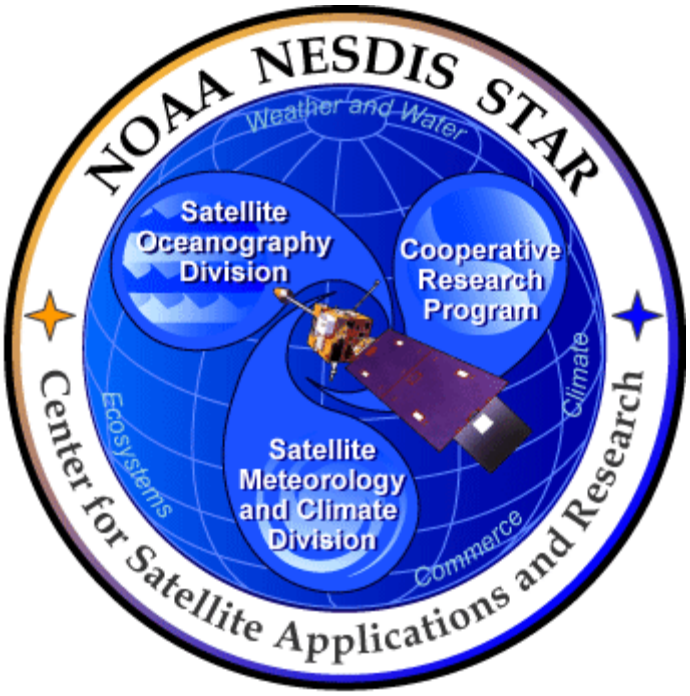


**NOAA NESDIS**
**CENTER for SATELLITE APPLICATIONS and RESEARCH**

# GOES-R Advanced Baseline Imager (ABI) Algorithm Theoretical Basis Document for Sea Surface Temperature

*Alexander Ignatov, NOAA/NESDIS/STAR*

August 30, 2010

# CONTENTS

# LIST OF FIGURES

# LIST OF TABLES

# LIST OF ACRONYMS

| | |
|---|---|
| ABI | Advanced Baseline Imager |
| ACM | ABI Cloud Mask |
| ACSPO | Advanced Clear-Sky Processor for Oceans |
| AIT | Algorithm Integration Team |
| AT | Algorithm Team |
| ATBD | Algorithm Theoretical Base Document |
| AWG | Algorithm Working Group |
| BT | Brightness Temperature |
| CLAVRx | CLouds from AVHRR extended |
| CONUS | Continental United States |
| CRTM | Community Radiative Transfer Model |
| ECMWF | European Centre for Medium-range Weather Forecasts |
| FD | Full Disk |
| GFS | Global Forecast System |
| GOCART | Global Ozone Chemistry Aerosol Radiation Transport |
| GOES | Geostationary Operational Environmental Satellite |
| GS-F&PS | Ground Segment Functional and Performance Specification |
| IMS | Ice Mapping System |
| IPT | Integrated Product Team |
| IR | Infrared |
| LST | Land Surface Temperature |
| LUT | Look-Up Table |
| MODIS | Moderate Resolution Imaging Spectroradiometer |
| MRD | Mission Requirement Document |
| MSG | Meteosat Second Generation |
| NAAPS | Navy Aerosol Analysis and Prediction System |
| NCEP | National Centers for Environmental Prediction |
| NESDIS | National Environmental Satellite, Data, and Information Service |
| NGST | Northrop Grumman Space Technology |
| NOAA | National Oceanic and Atmospheric Administration |
| NPOESS | National Polar-orbiting Operational Environmental Satellite System |
| NRT | Near-Real Time |
| OCD | Operations Concept Document |
| OISST | Optimal Interpolation SST |
| OSTIA | Operational Sea Surface Temperature and Sea Ice Analysis |
| QC | Quality Control |
| QF | Quality Flag |
| QA | Quality Assurance |
| QI | Quality Indicator |
| RMSD | Root-Mean Squared Deviation |

| | |
|---|---|
| RTG | Real-Time, Global SST |
| RTM | Radiative Transfer Model |
| SEVIRI | Spanning Enhanced Visible and Infrared Imager |
| SNR | Signal to Noise Ratio |
| SRF | Spectral Response Function |
| SST | Sea Surface Temperature |
| STAR | Center for Satellite Applications and Research |
| STD | Standard Deviation |
| SW | Split Window |
| SWA | Software Architecture Document |
| TIR | Thermal Infrared |
| TOA | Top Of Atmosphere |
| TPW | Total Precipitable Water [content in the atmosphere] |
| UTC | Universal Time Coordinated |
| VIIRS | Visible/Infrared Imager/Radiometer Suite |
| VVP | Verification and Validation Plan |
| WV | Water Vapor |

# ABSTRACT

This Algorithm Theoretical Basis Document (ATBD) provides a high-level description of the physical/mathematical basis and operational implementation of the sea surface temperature (SST) product derived from the Advanced Baseline Imager (ABI), which will be flown onboard the NOAA Geostationary Operational Environmental Satellite R series (GOES-R).

Currently, prior to launch of GOES-R, the SST algorithms have been prototyped with available satellite data, including AVHRR onboard NOAA 16-19 and METOP-A (similar spectral characteristics), and SEVIRI onboard MSG 1-2 (similar geostationary measurements). The retrieval system is the Advanced Clear-Sky Processor for Oceans (ACSPO), built upon heritage Clouds from the AVHRR Extended (CLAVR-x) system. ACSPO generates a suite of products including top-of-atmosphere (TOA) clear-sky brightness temperatures (BTs) and SSTs. The suite of products is accompanied by an external cloud mask (CM) and internally generated quality control (QC).

Three versions of SST algorithms have been implemented: (1) the regression algorithm, based on split-window nonlinear SST (NLSSST) and/or multi-channel SST (MCSST); (2) the radiative transfer model (RTM) inversion algorithm, based on the optimal estimation (OE) technique; and (3) the hybrid algorithm, based on a combination of the above two approaches. The ACSPO system requires as its input optical and thermal infrared channels, navigation and observational/illumination geometry. Two of its major ancillary data sources are the global daily 0.25º and weekly 1º reference Reynolds SST (OISST) fields, and 6-hour 1º National Centers for Environmental Prediction Global Forecast System (NCEP/GFS) atmospheric profiles. Ancillary GFS and OISST data are used as input to the fast Community Radiative Transfer Model (CRTM) to simulate clear-sky channel BTs. CRTM BTs are utilized for inversion and hybrid SST retrievals and QC of SST and BT. Web-based tools are being developed for near-real time (NRT) operational monitoring of the quality of SST and BT products and for calibration/validation (Cal/Val) of SST products. Currently, these tools are employed routinely with multiple AVHRR (NOAA 16-19) and METOP-A sensor data.

The SST Quality Monitor (SQUAM) tool allows monitoring of statistics of SST biases with respect to multiple reference SST fields, including OISST, Operational Sea Surface Temperature and Sea Ice Analysis (OSTIA), and Real-Time, Global SST (RTG). The Monitoring of IR Clear-sky Radiances over Oceans for SST (MICROS) tool allows monitoring of statistics of channel BT biases with respect to CRTM predictions. Finally, the Cal/Val tool provides calibration and validation of the SST product with respect to *in situ* (buoy) data. Drifting and tropical moored buoy data collected by the NCEP Global Telecommunication System (GTS) were selected for SST validation. Another NRT tool, in situ Quality Monitor (*iQuam*) is being set up to routinely conduct quality control of GTS in situ data. The results of prototyping and validation of the ABI SST product show that its accuracy and precision are close to those of other world-class SST products and well within existing GOES-R ABI specifications.

# 1 INTRODUCTION

The purpose, users, scope, related documents and revision history of this document are briefly described in this Section. Section 2 gives an overview of the sea surface temperature (SST) retrieval algorithm, including objectives and characteristics of the Advanced Baseline Imager (ABI) instrument. Section 3 describes the baseline algorithm and input and output data. Section 4 provides theoretical backgrounds of the SST retrieval problem and retrieval algorithms. Validation is described in Section 5, practical considerations in Section 6, assumptions and limitations associated with the algorithm in Section 7, and references are listed in Section 8.

## 1.1 Purpose of This Document

This Algorithm Theoretical Basis Document (ATBD) provides a high-level description of the physical basis and related mathematical formalism for an algorithm to derive the sea surface temperature (SST) product as a part of the requirements for the ABI. The ABI is the primary visible and infrared instrument to be flown onboard the platform of the Geostationary Operational Environmental Satellite (GOES) R series (GOES-R) of NOAA meteorological satellites. In addition, this document provides an overview of the required input data, product output, predicted performance, practical considerations, and assumptions and limitations.

## 1.2 Who Should Use This Document

The intended users of this document are those interested in understanding the physical basis of the SST algorithm and how to use the output of this algorithm for a particular application. This document also provides information useful to anyone maintaining or modifying the original algorithm.

## 1.3 Inside Each Section

This document covers the theoretical basis for the derivation of the SST product from ABI data. It is broken down into the following main sections:

- **System Overview:** Provides objectives of the SST algorithm, relevant details of the ABI instrument, and a brief description of the product requirements.
- **Algorithm Description:** Provides the general flow chart of the SST algorithm and detailed description of its inputs and its outputs.
- **Theoretical Description:** Provides a physical and mathematical background for the SST retrieval problem and algorithms.
- **Validation of SST Algorithms:** Provides a description of the methodology and the results of the validation of SST algorithms with the test data sets.
- **Practical Considerations:** Provides an overview of the issues involving numerical computation, programming and procedures, quality assessment and diagnostics, and exception handling.

- **Assumptions and Limitations:** Provides an overview of the current limitations of the approach and a plan for overcoming these limitations with further algorithm development.

## 1.4 Related Documents

This document may contain information listed in some other GOES-R documents available from the website maintained by the GOES-R Algorithm Working Group (AWG): www.star.nesdis.noaa.gov/star/goesr/index.php

The reader might want to refer to the following documents in conjunction with the current ATBD:

- GOES-R Series Ground Segment Functional and Performance Specification
- GOES-R Series Mission Requirements Document
- GOES-R SST Team Critical Design Review
- GOES-R SST Team Annual Reports to AWG in July 2008 and July 2009
- GOES-R Algorithm Theoretical Base Document for ABI Cloud Mask

Other related references are listed in the Reference Section.

## 1.5 Revision History

Version 0.0 of this document was created by Dr. Alexander Ignatov of NOAA/NESDIS in August 2008 and its intent was to accompany the delivery of the version 1.0 SST algorithm to the GOES-R Algorithm Integration Team (AIT).

Version 1.0 was created by A. Ignatov in July 2009 to update the ATBD document to 80% readiness and to accompany two subsequent deliveries (versions 2 and 3) of the SST code that occurred between August 2008 and July 2009.

Version 2.0 was created by A. Ignatov, B. Petrenko, N. Shabanov, and Y. Kihai in May 2010 to comply with 100% ATBD readiness and to support final GOES-R SST code delivery to AWG.

# 2 OBSERVING SYSTEM OVERVIEW

SST is needed for many applications including monitoring climate variability, seasonal forecasting, operational weather and ocean forecasting, military and defense operations, validating or forcing ocean and atmospheric models, ecosystem assessment, tourism, and fisheries (e.g., Donlon et al., 2007). Satellite retrievals of SST can be assimilated into climate, mesoscale atmospheric, and sea surface numerical models, which form the cornerstone of the operational ocean forecasting systems.

The SST requirements and qualifiers for GOES-R SST are listed in Table 2.1 as defined by the mission requirement document (MRD) and the Ground Segment Functional and Performance Specification (GS-F&PS) document. The mission requirements and qualifiers are identical for the four major ABI scanning modes (including full disk, hemisphere, CONUS, and mesoscale).

**Table 2.1** *GOES-R mission requirements and qualifiers for SST (GS-F&PS).*

| Name | User & Priority | Geographic Coverage | Vertical Resolution | Horizontal Resolution | Mapping Accuracy | Measurements Range | Measurement Accuracy | Refresh Rate/ Coverage Time | Vendor-Allocated Ground Latency | Product Measurement Precision | | Temporal Coverage Qualifier | Product Extent Qualifier | Cloud Cover Qualifier | Product Statistics Qualifier |
|---|---|---|---|---|---|---|---|---|---|---|---|---|---|---|---|
| Sea Surface Temperature (Skin) | GOES-R | CONUS and US Navigable waters thru EEZ & Full Disk & Mesoscale | N/A | 2 km | 1 km | 270 to 313 K | 0.4 K | 60 min | 806 sec | 0.8 K | | Day and Night | Quantitative out to at least 67° LZA; qualitative at larger LZA | Clear conditions associated with threshold accuracy | Over specified geographic area |

This section describes objectives of the SST algorithm, details of the ABI instrument related to the SST algorithm, and the product requirements.

## 2.1 Products Generated

SST will be produced for each clear-sky pixel observed by the ABI sensor using a state-of-the-art SST algorithm, which meets the GOES-R mission requirement. Algorithm accuracy, simplicity, computational efficiency and robustness, and consistency with polar SST algorithms are priorities of the GOES-R SST development. Physics of radiative transfer within the "sea surface – atmosphere" system is set forth in section 4.1. SST, derived from satellite radiances, is sensitive to the temperature of the skin layer, but, as discussed in more detail in Section 4.1.1, using "bulk" in situ measurements for calculation of regression coefficients can introduce a bias of satellite SST towards "bulk" SST.

Satellite retrievals have become the major source of highly accurate and globally consistent SST data since the 1970s (e.g., McMillin, 1975; McMillin and Crosby, 1984; Llewellyn-Jones et al, 1984; McClain et al, 1985; Barton et al., 1995; Brisson et al., 2002; Brown and Minnett, 1998; Merchant and Harris, 1999; Kilpatrick et al, 2001; Merchant et al, 2008, 2009). In the thermal infrared (IR), SST can be retrieved only under clear skies. Accuracy of the satellite SST measurement is limited by the accuracy of sensor radiances, quality of cloud screening, and correction for the effects of atmospheric absorption and scattering and surface reflection in the retrieval algorithms. Section 4.2 contains detailed description of SST retrieval algorithms.

## 2.2 Instrument Characteristics

The ABI will be a mission-critical payload on GOES-R, providing over 65% of all the mission data products currently defined. Similar to the current GOES imager, ABI will be used for a wide

range of qualitative and quantitative weather, oceanographic, climate, and environmental applications. ABI will offer higher spatial resolution and a faster imaging rate than the current GOES imager. Its spatial resolution will be nominally 2 km for the infrared bands and 0.5 km for the 0.64 μm visible band. While the instrument will allow a flexible scanning scenario, two basic modes are anticipated. The first is a flexible scanning scenario that will provide one scan of the Full Disk (FD), three scans (5 minutes apart) of the Continental United States (CONUS), and 60 scans (30 seconds apart) over a selectable 1000 km ×1000 km area every 15 minutes. The second mode is continuous FD scanning in which FD coverage is obtained every 5 minutes. In practice, some combination of both modes may be used. For example, three sequential FD images that are 5 minutes apart may be taken every hour for the generation of SST. The flexible scanning mode would then be used for the rest of the hour. For comparison, it takes approximately 25 minutes for the current GOES imager to scan the FD; GOES-R will thus provide a fivefold increase in the coverage frequency (Schmit et al., 2005).

ABI has 16 spectral bands. Figure 2.1 shows the spectral distribution of the ABI long-wave infrared channels, compared to the corresponding GOES-12 imager channels. Five ABI bands are similar to the 0.6-, 4-, 11-, and 12-μm windows and the 6.5-μm water vapor band on the current GOES-8/-9/-10/-11 imagers (Menzel and Purdom, 1994; Ellrod et al., 1998), and another is similar to the 13.3 μm on the GOES-12/-N/-O/-P imagers and the GOES-8/-P sounders (Schmit et al., 2005). Additional bands on ABI are 0.47 μm for aerosol detection and visibility estimation; 0.865 μm for aerosol detection and estimation of vegetation index and health; 1.378 μm to detect very thin cirrus clouds; 1.6 μm for snow/cloud discrimination; 2.25 μm for aerosol and cloud particle size estimation, vegetation, cloud properties/screening, hot-spot detection, moisture determination, and snow detection; 7.0 and 7.34 μm for mid-tropospheric water vapor detection and tracking and upper-level sulfur dioxide ($SO_2$) detection; 8.5 μm for detection of volcanic dust clouds containing sulfuric acid aerosols and estimation of cloud phase; 9.6 μm for monitoring atmospheric total column ozone and upper-level dynamics; and 10.35 μm for deriving low-level moisture and cloud particle size.

Each of these bands is often used in conjunction with other bands in a multiple spectral approach for product generation. For SST estimation, window bands centered at 3.7, 11, and 12 μm are used on the heritage sensors AVHRR and SEVIRI (Llewellyn-Jones et al., 2004; McClain et al., 1985; Schmetz et al., 2002). The 3.7-$\mu$m band is very transparent and may be used at night, while during daytime it is contaminated by solar reflectance. The ABI split-window configuration features three bands instead of the two found in heritage sensors. This offers additional potential but also may present a challenge if the two end bands centered at 10.35 and 12.3 $\mu$m are pushed too far in the absorption lines. The 8.5-$\mu$m is another window band that may be used in conjunction with the 10.35-$\mu$m and 11.2-$\mu$m bands for improved thin cirrus detection as well as for better atmospheric moisture correction in relatively dry atmospheres (Schmit et al., 2005). In summary, the SST retrieval will thus rely on channels 7 (3.9), 11 (8.5), 13 (10.35), 14 (11.2), and 15 (12.3 μm) of the ABI.

Channel specification of the ABI is given in Table 2.2. The advanced design of ABI will provide SST users with twice the spatial resolution, five times the scan rate, more spectral channels, and improved radiometric performance compared to the current GOES imager and SEVIRI. These improvements should allow significant improvements in the accuracy of SST.

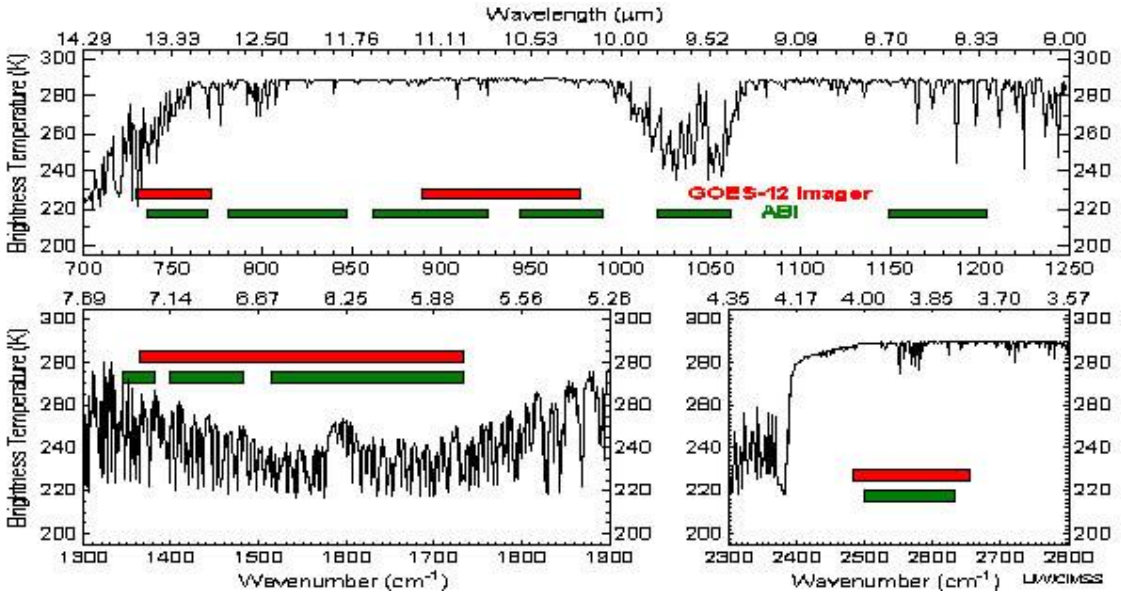


***Figure 2.1*** *Spectral distribution of the ABI channels, compared to GOES-12 Imager channels (after Schmit et al., 2005).*

***Table 2.2*** *Spectral and radiometric characteristics for the ABI channels. Green color highlights the channels, which are used in SST retrieval. Blue color highlights the channels, potentially useful for SST. For SEVIRI, only channels 14 and 15 are currently used because of problems with CRTM.*

| Channel Number | Usage | Wavelength (μm) | Bandwidth (μm) | NEDT/SNR | Upper Limit of Dynamic Range | Spatial Resolution |
|---|---|---|---|---|---|---|
| 1 | No | 0.47 | 0.45 – 0.49 | 300:1[1] | 652 $W/m^2/sr/\mu m$ | 1 km |
| 2 | No | 0.64 | 0.59 – 0.69 | 300:1[1] | 515 $W/m^2/sr/\mu m$ | 0.5 km |
| 3 | No | 0.86 | 0.8455 – 0.8845 | 300:1[1] | 305 $W/m^2/sr/\mu m$ | 1 km |
| 4 | No | 1.38 | 1.3705 – 1.3855 | 300:1[1] | 114 $W/m^2/sr/\mu m$ | 2 km |
| 5 | No | 1.61 | 1.58 – 1.64 | 300:1[1] | 77 $W/m^2/sr/\mu m$ | 1 km |
| 6 | No | 2.26 | 2.225 – 2.275 | 300:1[1] | 24 $W/m^2/sr/\mu m$ | 2 km |
| 7 | Yes | 3.9 | 3.8 – 4.0 | 0.1K[2] | 400K | 2 km |
| 8 | No | 6.15 | 5.77 – 6.60 | 0.1K[2] | 300K | 2 km |
| 9 | No | 7.0 | 6.75 – 7.15 | 0.1K[2] | 300K | 2 km |
| 10 | No | 7.4 | 7.24 – 7.44 | 0.1K[2] | 320K | 2 km |
| 11 | Potentially | 8.5 | 8.30 – 8.70 | 0.1K[2] | 330K | 2 km |
| 12 | No | 9.7 | 9.42 – 9.80 | 0.1K[2] | 300K | 2 km |
| 13 | Potentially | 10.35 | 10.10 – 10.60 | 0.1K[2] | 330K | 2 km |
| 14 | Yes | 11.2 | 10.80 – 11.60 | 0.1K[2] | 330K | 2 km |
| 15 | Yes | 12.3 | 11.80 – 12.80 | 0.1K[2] | 330K | 2 km |
| 16 | No | 13.3 | 13.0 – 13.6 | 0.3K[2] | 305K | 2 km |

*[1]100% albedo, [2]300K scene.*

# 3 ALGORITHM DESCRIPTION

A complete description of the algorithm at the current level of maturity is given in this Section. The algorithm and this ATBD are expected to mature as time goes on and algorithm development progresses.

## 3.1 Algorithm Overview

For detailed description of the algorithm see sections 4.2 - 4.3. The FD image processing within the SST module includes:

- calculation of regression, hybrid and inversion SSTs (note that currently inversion SST is not recorded in the output file but is used in the SST QC; this may be subject to change)
- SST quality control (SST QC)
- accumulation of BT and SST anomaly histograms over ocean pixels and updated bias file.

## 3.2 Processing Outline

The flow chart of the SST algorithm is shown in Fig. 3.1. SST retrieval will be performed with the special SST module within the Algorithm Integration Team (AIT) framework. The preparational procedures for SST, which should be executed within the AIT framework and the SST specific procedures, executed by the SST module, are shown in Fig. 3.1 in different colors.

The SST module processes the full disk (FD) images sequentially. The sequence of image processing is important because the SST module tracks variable global biases in SST and BT and recursively averages them over several sequential images. In the beginning of every FD image processing, the SST module reads previously estimated biases from the special bias file and updates this file at the end of FD image processing. If the bias file is not available when the first FD image is processed, the biases are initialized within the SST module.

The data needed for SST and prepared within the AIT framework include:

- satellite FD information
- configuration file
- ABI cloud mask and ice mask
- static and dynamic ancillary data
- Clear-sky BT and BT Jacobian, simulated with the Community Radiative Transfer Model (CRTM) on the GFS grid and bilinearly interpolated to the sensor's pixels
- Reynolds SST bilinearly interpolated to the sensor's pixels.

SST retrievals in each scanning mode will be performed during day and night, for cloud-free (i.e., "clear" and "probably clear" indicated by the ABI cloud mask) sea surface pixels only. The ABI cloud mask (ACM) will be used for preliminary cloud detection.

The SST algorithms, used in a split- or triple-window formulation (that is, using two or three channels), will be applied to correct for atmospheric absorption.

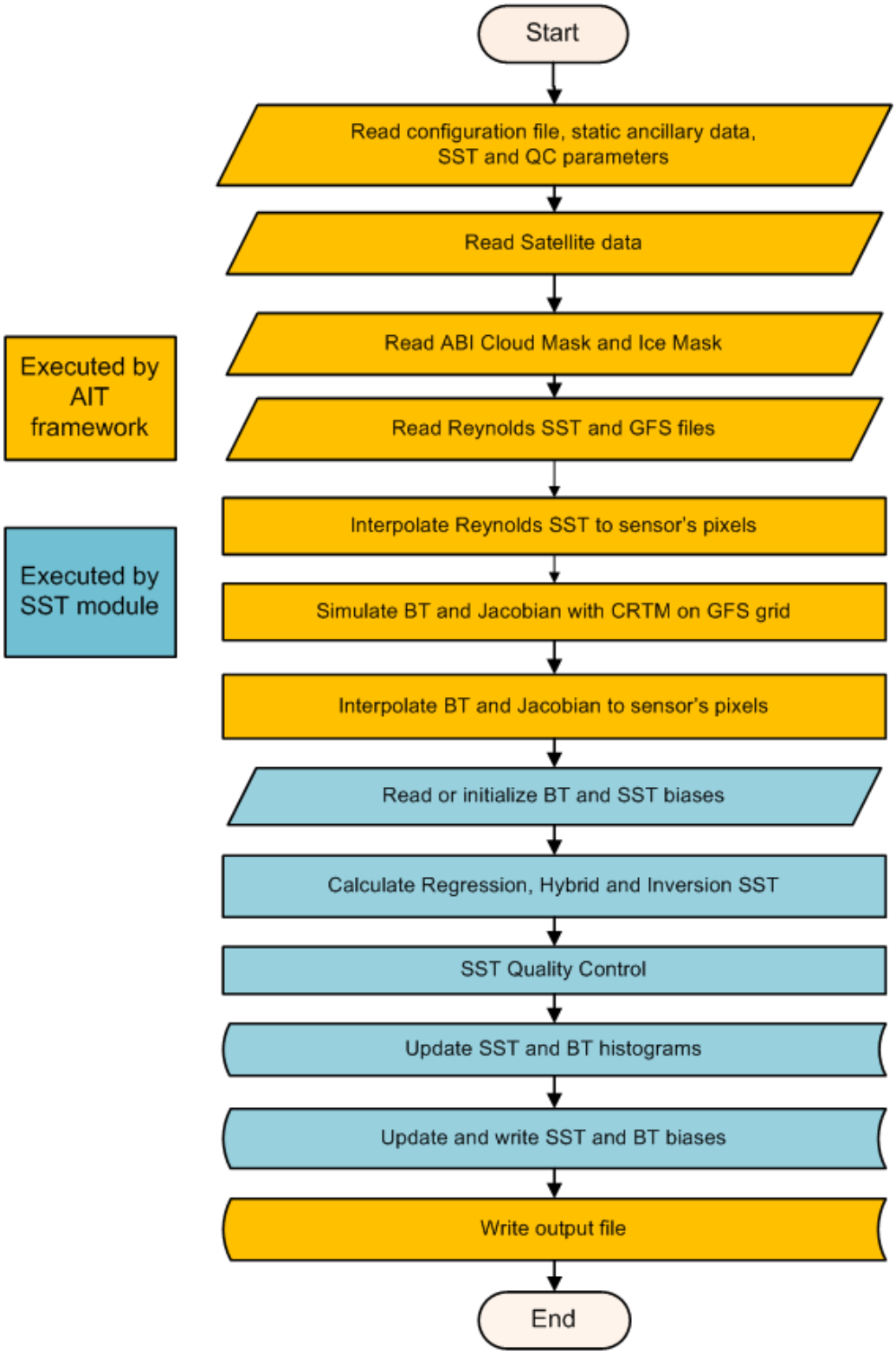


**Figure 3.1** *The flow chart of GOES-R ABI data processing for SST within the AIT framework.*

Based on the validation results of the three SST algorithms, the hybrid algorithm has been chosen as the baseline ABI SST algorithm. The regression algorithm is used as a back-up algorithm because it is more simple and robust and won't fail if the GFS or Reynolds SST data are not available. The inversion algorithm is also kept in the code and is used in the SST QC because of its ability to effectively minimize BT residuals under clear-sky conditions.

The SST QC estimates SST retrieval quality, which is captured using a set of flags and indicators. Cloud flags are passed from the input data, whereas SST quality flags are generated within the SST module. Currently, the quality flags and indicators are only assigned to the hybrid SST product, but they may be also used for estimation of the quality of the regression and inversion products.

SST development is closely coordinated with the cloud AT (Shabanov et al., 2010). The major objective of SST/cloud collaboration is ensure that the ABI cloud mask reliably identifies "confidently cloudy" and "probably cloudy" pixels, which are therefore not considered by the SST algorithm. SST QC marks these pixels as "cloudy" by the CM. Since the ABI cloud mask was designed to be conservative and minimize the discarding of potentially good data, the "clear" and "probably clear" pixels might still have significant cloud contamination which has a measurable effect on the SST product. This contamination is further quantified by SST QC and annotated by the SST Quality Flags (QF) and Quality Indicators (QI).

## 3.3 Algorithm Input

This section describes the input needed to compute the SST product. While the SST is derived for each pixel, the QC requires calculation of SST variability in the $n \times n$ sliding window around the central pixel, where $n$ is a TBD number (currently, $n$=11).

### 3.3.1 Primary Sensor Data

Table 3.1 lists the primary sensor data (i.e., information derived solely from the ABI observations and geolocation information), which is used by the SST algorithm.

The specific approach to convert satellite channel data stored as counts to radiances and radiances to BTs is specified by sensor calibration team. In the case of SEVIRI, BTs are derived according to the following parametric equations:

$$L_{eff}(\lambda) = gain(\lambda)\, count(\lambda) + offset(\lambda), \tag{3.1a}$$

$$\alpha(\lambda) \cdot T_{eff}(\lambda) + \beta(\lambda) = \frac{c_2(\lambda) \cdot \nu(\lambda)}{ln\left[1 + \nu^3 \frac{c_1}{L_{eff}(\lambda)}\right]}. \tag{3.1b}$$

Here, $L_{eff}$ and $T_{eff}$ are effective radiance and BT, quantities averaged over sensor bandwidth (EUMETSAT-1); $\lambda$ and $\nu$ are wavelength and frequency. EUMETSAT implemented operationally effective quantities for data starting May 05, 2008, at 08:00 UTM. Values of parameters (*gain, offset, count,* $\alpha$, $\beta$, $c_1$, $c_2$, $c_3$) are listed in Tables 3.2 and 3.3 for MSG-1 and

MSG-2 respectively and can also be found in the L1B data header. Alternatively, Look-Up Tables can be used to convert radiances to BTs with improved accuracy.

### 3.3.2 ABI-Based Ancillary Data

Table 3.4 describes the ancillary data, obtained from ABI data processing required for SST.

### 3.3.3 Non-ABI Ancillary Static Data

Table 3.5 lists and describes the static ancillary data (information not included in the ABI observations or geolocation data) required to run the SST algorithm.

### 3.3.4 Non-ABI Ancillary Dynamic Data

Table 3.6 describes the dynamic ancillary data required to run the SST algorithm. By ancillary data, we mean data that requires information not included in the ABI observations or geolocation data. The only data of this type needed by the SST module is Reynolds (weekly or daily) OISST analysis, bilinearly interpolated from the analysis grid to the sensor's pixels.

### 3.3.5 Algorithm Coefficients and Control Values (ABI-specific static)

Algorithm coefficients, look-up tables and some criterion values for algorithm selection and for quality control flags which will be ingested as input data are shown in Table 3.7. Tables 3.8 and 3.9 list the contents of configuration and parameters files.

***Table 3.1*** *Input list of sensor data.*

| Name | Type | Description | Dimension |
|---|---|---|---|
| Ch07 ABI BT | input | Calibrated ABI level 1b BT in channel 07 | grid (xsize, ysize)* |
| Ch11 ABI BT | input | Calibrated ABI level 1b BT in channel 11 | grid (xsize, ysize) |
| Ch13 ABI BT | input | Calibrated ABI level 1b BT in channel 13 | grid (xsize, ysize) |
| Ch14 ABI BT | input | Calibrated ABI level 1b BT in channel 14 | grid (xsize, ysize) |
| Ch15 ABI BT | input | Calibrated ABI level 1b BT in channel 15 | grid (xsize, ysize) |
| Latitude | input | Pixel latitude | grid (xsize, ysize) |
| Longitude | input | Pixel longitude | grid (xsize, ysize) |
| Solar zenith | input | ABI solar zenith angles | grid (xsize, ysize) |
| Solar azimuth | input | ABI solar azimuth angles | grid (xsize, ysize) |
| View zenith | input | ABI local zenith angle | grid (xsize, ysize) |
| View azimuth | input | ABI view azimuth angle | grid (xsize, ysize) |
| External ABI QC Flags | input | ABI quality control flags available from L1b data | grid (xsize, ysize) |

***Table 3.2*** *Calibration parameters for SEVIRI MSG-1.*

| | $\lambda_c$, [μm] | $\nu_c$, [$cm^{-1}$] | gain | offset | $C_1$ | $C_2$ | α | β |
|---|---|---|---|---|---|---|---|---|
| Ch 01 | 0.60 | | 2.3128100E-02 | -1.179533 | | | | |
| Ch 02 | 0.80 | | 2.9726600E-02 | -1.516057 | | | | |
| Ch 03 | 1.60 | | 2.3621900E-02 | -1.204717 | | | | |
| Ch 04 | 3.92 | 2567.33 | 3.6586667E-03 | -0.186592 | 201960.5 | 3696.35 | 0.9959 | 3.471 |
| Ch 09 | 10.80 | 930.68 | 0.2050344 | -10.45676 | 9600.593 | 1339.004 | 0.9983 | 0.627 |
| Ch 10 | 12.00 | 839.66 | 0.2223114 | -11.33788 | 7050.798 | 1208.079 | 0.9988 | 0.397 |

***Table 3.3*** *Calibration parameters for SEVIRI MSG-2.*

| | $\lambda_c$, [μm] | $\nu_c$, [$cm^{-1}$] | gain | offset | $C_1$ | $C_2$ | α | β |
|---|---|---|---|---|---|---|---|---|
| Ch 01 | 0.60 | | 2.0135500E-02 | -1.0269100 | | | | |
| Ch 02 | 0.80 | | 2.5922000E-02 | -1.3220220 | | | | |
| Ch 03 | 1.60 | | 2.2258500E-02 | -1.1351830 | | | | |
| Ch 04 | 3.92 | 2567.33 | 3.6586667E-03 | -0.1865920 | 201898.7 | 3695.958 | 0.9954 | 3.438 |
| Ch 09 | 10.80 | 930.68 | 0.2050344 | -10.45676 | 9632.847 | 1340.502 | 0.9983 | 0.640 |
| Ch 10 | 12.00 | 839.66 | 0.2223114 | -11.33788 | 6970.092 | 1203.452 | 0.9988 | 0.408 |

***Table 3.4*** *ABI-based input to SST algorithm.*

| Name | Type | Description | Dimension |
|---|---|---|---|
| ABI cloud mask | input | ABI Level 2 cloud mask data | grid (xsize, ysize) |
| Snow/ice mask | input | ABI Level 2 snow/ice mask data | grid (xsize, ysize) |

***Table 3.5*** *Non-ABI based static input ancillary data to SST algorithm.*

| Name | Type | Description | Dimension |
|---|---|---|---|
| Land/sea mask | input | A land/sea and coast mask | grid (xsize, ysize) |

***Table 3.6*** *Non-ABI based dynamic input ancillary data to SST algorithm.*

| Name | Type | Description | Dimension |
|---|---|---|---|
| SST Reference field | input | Reynolds SST** | grid (xsize, ysize) |
| Ch 07 ABI BT and Jacobian | input | CRTM*** Clear sky BT and Jacobian in ABI Ch07 | grid (xsize, ysize) |
| Ch 11 ABI BT and Jacobian | input | CRTM Clear sky BT and Jacobian in ABI Ch11 | grid (xsize, ysize) |
| Ch 13 ABI BT and Jacobian | input | CRTM Clear sky BT and Jacobian in ABI Ch13 | grid (xsize, ysize) |
| Ch 14 ABI BT and Jacobian | input | CRTM Clear sky BT and Jacobian in ABI Ch14 | grid (xsize, ysize) |
| Ch 15 ABI BT and Jacobian | input | CRTM Clear sky BT and Jacobian in ABI Ch15 | grid (xsize, ysize) |

* grid(xsize,ysize) is a 2-D data array at Satellite grid (i.e., SEVIRI grid), ysize is the number of scan lines and xsize is the number elements in each line.

** CRTM data ($1^o$ x 3-, 6-, 9- and 12- h, corresponding to input GFS data resolution) interpolated to Satellite grid.

*** Reynolds SST data (1° × weekly or 0.25° × daily) interpolated to Satellite grid.

### 3.3.6 CRTM Simulations and Dynamic Ancillary Fields Used for SST

Reynolds SST is used as direct input for the SST retrieval module, as shown in Table 3.6. In addition, the SST module requires clear-sky BTs and BT Jacobian (the matrix of BT derivatives with respect to SST and Optical Depth Scaling Factor (ODSF); see Section 4.2.2). The CRTM simulates these variables on the GFS grid using Reynolds SST, GFS vertical profiles of atmospheric temperature and humidity, and local zenith angle as inputs. The CRTM simulation also uses the interpolated Reynolds SST and local angle for the pixels nearest to the GFS grid nodes. The output CRTM parameters – clear-sky BTs and Jacobian – are also bilinearly interpolated from the GFS grid to the sensor's pixels.

The weekly (or daily) Reynolds SST fields are available once a week (or day), and the SST module and CRTM use the latest available data for the Reynolds field, without interpolation in time. The GFS atmospheric fields are more variable than the SST field and are linearly interpolated in time to the sequential FD image times.

When doing bilinear interpolation of the Reynolds SST and CRTM fields, it is possible that for some sensor's pixels there will be less than four neighboring grid nodes with valid field values. This may occur, for example, in the vicinity of the coast lines, if some of the nearest nodes fall on the land. This also can happen if some grid nodes contain invalid data, marked with NaNs. In this case, the pixel will be assigned and average value over those nodes with valid parameter values.

***Table 3.7*** *ABI-specific algorithm coefficients and input values to SST algorithm.*

| Name | Type | Description | Dimension |
|---|---|---|---|
| Config | input | • Input/Output parameters (layers names, pathes, compression types, formatting types),<br>• Ancillary data parameters (pathes, version switches, control flags),<br>• Retrievals modes (use/not external CM, SST algorithm type) | Single ASCII file |
| CRTM LUTs | input | Parameters/settings used for CRTM calculations (including transmittance, sensor-specific, aerosols emissivity and cloud coefficients) | Multiple ASCII and Binary files |
| SST and SST QC LUTs | input | Parameters/settings used in SST and SST QC calculations (including regression coefficients, test thershoulds and parameters) | Single ASCII file |

***Table 3.8*** *Selected entries of the 'Config' file (ancillary data parameters and retrievals modes).*

| Name | Meaning | Value |
|---|---|---|
| SST_FG_Swch | First Guess SST type switch | 0 – weekly Reynolds<br>1 – daily SST (AVHRR v1)<br>2 – daily SST (AVHRR+AMSR, v1)<br>3 – daily SST (AVHRR, v2)<br>4 – daily SST (AVHRR+AMSR, v2)<br>5 – daily SST (OSTIA) |
| Fcst_Interval_Swch | GFS Forecast interval switch | 3 – 3-hour forecast<br>6 – 6-hour forecast<br>9 – 9-hour forecast<br>12 – 12-hour forecast |
| Extrn_CM_Swch | External Cloud Mask (CM) switch | 0 – Not read, not used;<br>1 – Read and used to minimize QC calculation;<br>2 – Read, but not used (pass-through) |
| SST_algorithm_Swch | Selection of the SST algorithm | 0 – Hybrid (primary)<br>1 – Regression (back-up) |

***Table 3.9*** *Parameters of the SST and SST QC 'Parameters' file.*

| Name | Meaning | Value |
|---|---|---|
| a1_Regr<br>a2_Regr<br>a3_Regr<br>a4_Regr | Coefficients of the Regression SST | 0.963999<br>0.0711657<br>0.820187<br>11.8430 |
| a1_Hybr<br>a2_Hybr<br>a3_Hybr<br>a4_Hybr | Coefficients of the Hybrid SST | 0.743279<br>1.07488<br>0.0589083<br>0.734534 |
| Unif_Thresh,<br>Radius_Value | SST Uniformity filter parameters | 0.09<br>1 |
| TA_Lower_Thresh,<br>TA_Upper_Thresh,<br>TA_Scale,<br>Rad_Value | SST filter parameters | -6.<br>-2.<br>3.<br>15 |
| BT_Resi_Lower_Thresh<br>BT_Resi_Upper_Thresh | Radiance filter parameters | 1.<br>1. |
| Slope<br>Intercept_1<br>Intercept_2 | Optical Depth filter parameters | 0.05<br>1.1<br>1. |
| BT_Noise<br>FG_SST_Noise<br>FG_OD_Noise | Parameters of OE methods for SST and OD calculation | 0.2<br>1.5<br>0.2 |

## 3.4 Theoretical description

### 3.4.1 Physics of the Problem

#### 3.4.1.1 Skin and Bulk SST

Surface IR emission is formed in the top ~10 μm of water and is sensitive to the so-called "skin SST" (e.g., Saunders, 1967a; Robinson et al., 1984; Donlon and Robinson, 1997; Donlon et al., 2002; Minnett, 2003). *In situ* sensors, on the other hand, typically measure bulk SST, which differs from skin SST due to the skin effect (cold skin-layer, due to heat exchange at the surface), and diurnal thermocline (e.g., Gentemann et al., 2003; Horrocks et al., 2003; Gentemann, 2007; Gentemann and Minnett, 2008). The difference between skin and bulk SSTs may reach several degrees, especially during the daytime under clear-sky and low wind conditions, when the mixing in the upper layer is suppressed and therefore strong diurnal warming may develop (Fairall, 1996; Murray et al., 2000; Wick et al., 2002; Castro et al., 2002; Stuart-Menteth et al., 2003; Tanashi et al., 2003; Nardielli et al., 2005). Figure 3.2 shows typical vertical distributions of SST during day and night, and gives definitions of SSTs. Using *in situ* bulk SSTs for validation of the ABI skin SST product has limitations. Existing approaches to nighttime skin-to-bulk SST conversion may use a constant offset of ~0.17 K. If surface wind speed, *w*, is available, then the following relationship between skin and bulk SST was proposed by Donlon et al (2002):

$$SST_{bulk}=SST_{skin} - [0.14 + 0.30exp(-w/3.7)] \quad (3.2)$$

During daytime, the relationship between skin and bulk SSTs is more complex, due to the effect of the diurnal thermocline. Its modeling requires knowledge of fluxes at the surface, including their history. In this ATBD, correction of *in situ* data and retrieved SST for skin/bulk difference was not applied. The coefficients for regression and hybrid algorithm were calculated from matchups of BTs and *in situ* bulk SSTs. The BT bias correction for the inversion algorithm is based on Reynolds SST, which is anchored to *in situ* SST (Reynolds et al., 1994, 2007). Also, Reynolds SST is used as the first-guess SST input for CRTM to model first-guess BTs. On the other hand, the observed BTs, from which the SST products are derived, are sensitive to skin SST. As a result, SST, retrieved with all three algorithms in this ATBD, reflects variations in skin SST, but on average represents bulk SST. Recently, Castro et al. (2010) have found that the accuracy of regression, produced from matchups of bulk SST and AVHRR BTs, is not worse (and often is better) than the accuracy of regression, produced from matchups of skin SST and AVHRR BTs. Nevertheless, we plan to explore the performance of skin-bulk conversion algorithms outside this ATBD, at the Cal/Val stage of the project. If these conversions are found to be efficient, they will be incorporated into the SST retrieval algorithms.

#### 3.4.1.2 Surface Emissivity

Ocean surface is not a black body. Overall, emissivity of sea water is well constrained (compared to, e.g., land emissivity). It is less than unity and depends upon spectral interval and local zenith angle (e.g., Smith et al., 1996; Watts et al., 1996). Spectral and angular structure of emissivity is defined by Fresnel's laws and sea surface roughness. Typical emissivities of a flat surface in the thermal IR windows representative of AVHRR, SEVIRI, and ABI bands are shown in Fig. 3.3.

They were calculated with spectral refractive indexes (Friedman, 1969; Hale and Querry, 1973; Downing and Williams, 1975; Pinkley et al., 1977; Segelstein, 1981).

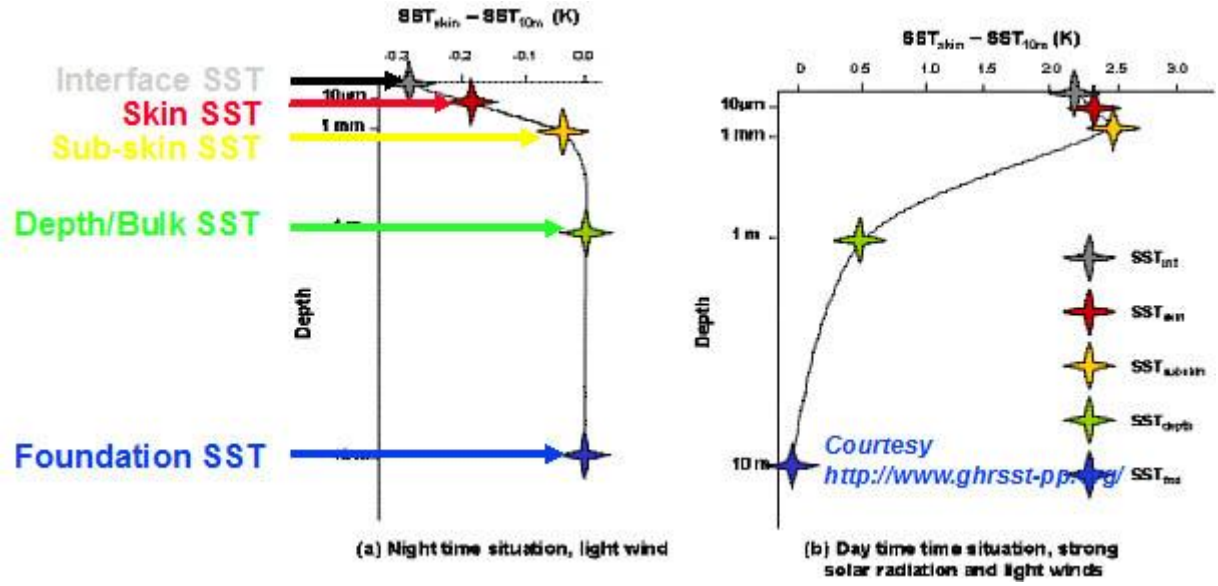


**Figure 3.2** *Definitions of different SSTs (after Donlon et al., 2007):*

- *Interface SST is a temperature at exact air-sea interface*
- *Skin SST is a temperature measured by IR radiometer at ~10-20µm depth*
- *Subskin SST is a temperature at the base of a conductive laminar sub-layer*
- *Depth/bulk SST is a temperature measured by drifting buoys at ~1 m depth*
- *Foundation SST is a temperature of the water column free from diurnal variability*

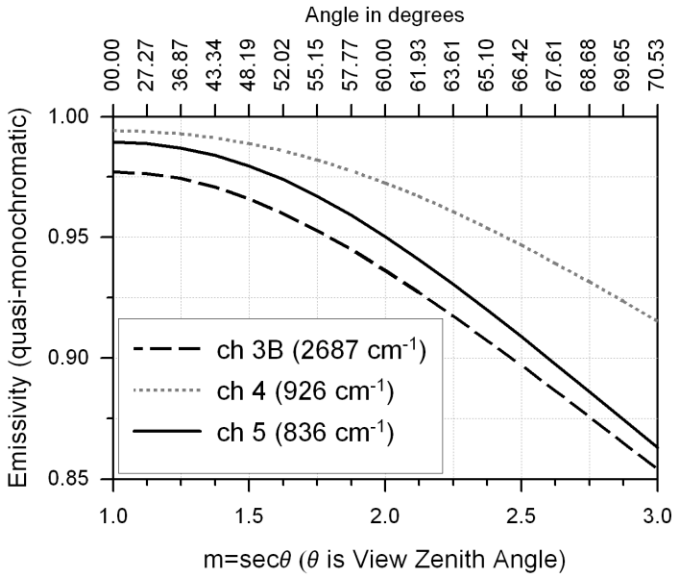


**Figure 3.3** *Typical spectral and angular dependence of sea water emissivity in the AVHRR bands (Dash and Ignatov, 2008).*

Emissivity is also a function of wind speed (e.g., Wu and Smith, 1997; Minnett et al., 2001; Masuda et al., 2006; Nalli et al., 2008ab), water temperature, and salinity (e.g., Newman et al., 2005). These corrections are relatively small but can introduce errors in SST retrievals up to several tenths of a degree Kelvin (e.g., Hanafin and Minnett, 2005; Niclos et al., 2005; Donlon et al., 1998, 2002).

### 3.4.1.3 Atmospheric Transmittance

Assuming clear sky conditions and neglecting atmospheric scattering, the top of atmosphere (TOA) radiance (I(ν)) is customarily described by (e.g., Deschamps and Phulpin, 1980; Chedin et al., 1985; Berk et al, 1998, 2002; Han et al., 2006; Dash and Ignatov, 2008)

$$I(\nu) = I_S(\nu) + I_{atm}(\nu)^{\uparrow} + I_{atm}(\nu)^{\downarrow} \tag{3.3}$$

Here, $I_s(\nu)$, $I_{atm}(\nu)^{\uparrow}$ and $I_{atm}(\nu)^{\downarrow}$ represent the surface emission, atmospheric upwelling, and reflected downwelling radiance, respectively, and ν is frequency. The radiance components are illustrated in Fig. 3.4.

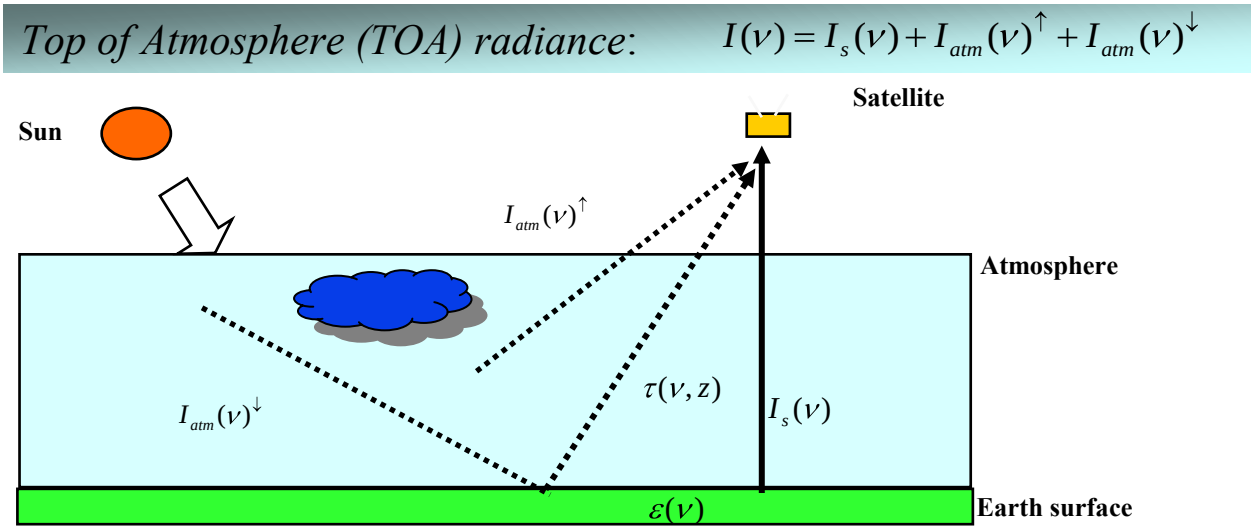


**Figure 3.4** *Schematic of TOA radiation at satellite sensor level.*

Satellite SST retrievals are performed in infrared (IR) bands where the surface emission reaches its maximum, yet atmospheric absorption is small (c.f. Fig.3.5). Atmospheric transmittance varies depending upon atmospheric conditions and in the atmospheric windows is mostly defined by water vapor and temperature profiles (e.g., Saunders, 1967; Prabhakara et al., 1974; McMillin, 1975; Phulpin and Deschamps, 1980; Llewellyn-Jones et al., 1984). Typically, atmospheric correction algorithms are aimed at minimizing the water-vapor-induced error in retrieved SST (e.g., Minnett, 1990; Sobrino et al., 1993; Emery et al., 1994; Francois and Ottle, 1996; Steyn-Ross et al., 1997, 1999; Kumar et al., 2003; Merchant et al., 2006, 2008, 2009). Minor gases also affect transmission in the window bands, but their effect is typically small and much less variable in space and time (e.g., Dash and Ignatov, 2008).

Under typical maritime conditions, aerosol effects on atmospheric transmission in the window regions are smaller than the water vapor effects (e.g., Dash and Ignatov, 2008). These effects are much more complex and less explored (e.g., Walton, 1985; Walton et al, 1998; Merchant and Harris, 1999; Highwood et al., 2003; Vazquez et al., 2004; Hollweg et al., 2006; Nalli and Reynolds, 2006; Castro et al., 2008). Empirical correction for the effects of aerosols have been explored in the past (e.g., Nalli and Stowe, 2002; Merchant et al., 2006b) but they remain limited in scope. A more appropriate way to perform aerosol correction is based on an approach consistent with physical SST retrievals, i.e., using RTM with a global first-guess aerosol field (e.g., the Goddard Chemistry Aerosol radiation and Transport, or GOCART, Chin et al., 2000; the Navy Aerosol Analysis and Prediction System, or NAAPS, found at www.nrlmry.navy.mil/aerosol/). This approach appears relatively straightforward, at least in principle. However, it requires substantial investment in CRTM improvement and GOCART data exploration and may be explored later beyond the 100% ATBD.

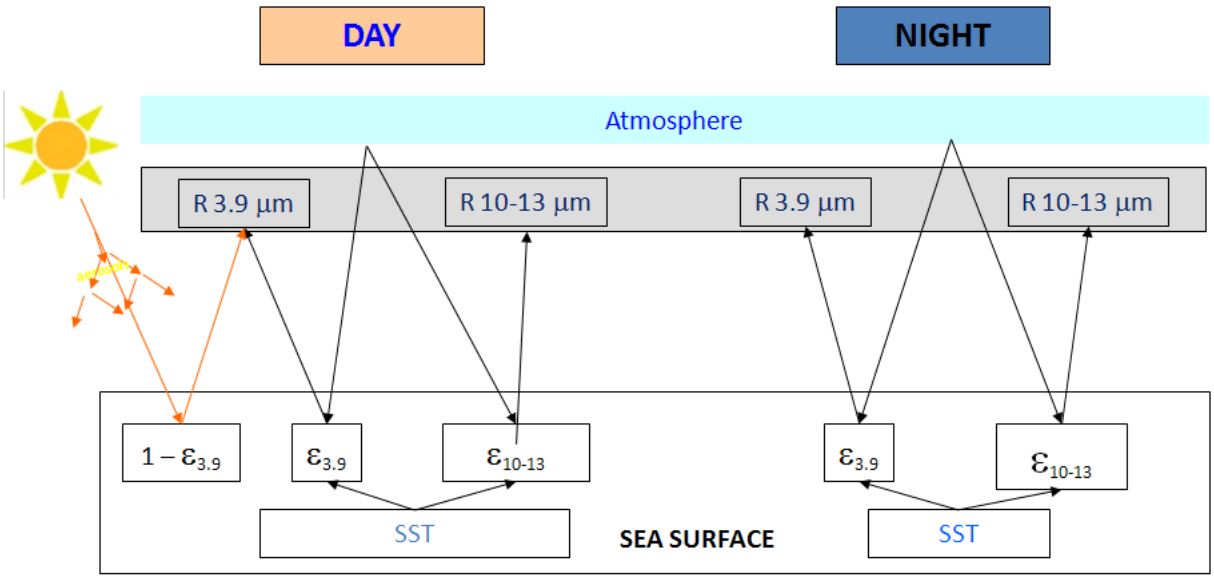


**Figure 3.5** *During daytime, shortwave IR band 3.9 µm is subject to solar scattering in the atmosphere and reflection form the surface. Unless these effects are corrected for, the shortwave window cannot be used during daytime for SST retrievals. However, it can be used at night when there is no solar contamination.*

Another factor that affects the top-of-atmosphere radiances is residual and ambient cloud. Effect of this factor on SST may be significant but it is even less explored than aerosols (e.g., Vazquez et al., 2004; Dash and Ignatov, 2008; Liang et al., 2009). The empirical approach considered in Xu and Ignatov (2008) may be explored, but these analyses are beyond the scope of this 100% ATBD.

During daytime, the shortwave IR window is subject to solar reflection and scattering as shown in Fig. 3.5. Unless these signals are corrected for, the shortwave band cannot be used during the day. Solar reflectance and scattering is also present in the longwave bands too, but the corresponding signals are much smaller there. However, the effect may reach from several tenths to several degrees of Kelvin in the glint areas (e.g., Khattak et al., 1991; Nath et al, 1993).

Correcting for this effect or screening data in the glint area is thus needed for accurate SST retrievals during daytime.

In IR bands, each of the components in Eq. (3.3) can be expressed mathematically as follows:

$$I_s(\nu) = \varepsilon(\nu)\tau_0(\nu)B(\nu,T_s) \tag{3.4a}$$

$$I_{atm}(\nu)^{\uparrow} = \int_z^0 B(\nu,T_p(z))\frac{\partial\tau(\nu,z)}{\partial z}dz \tag{3.4b}$$

$$I_{atm}(\nu)^{\downarrow} = (1-\varepsilon(\nu))\tau_0(\nu)\int_0^z B(\nu,T_p(z))\frac{\partial\tau(\nu,z)}{\partial z}dz \tag{3.4c}$$

(Note that each term in Eq. (3.4) is local zenith angle dependent but this dependence was omitted here for simplicity.) Here, ε is the surface emissivity, τ is the atmospheric transmittance, $\tau_o$ is the atmospheric transmittance from the surface to the top of the atmosphere, z is the height, $T_s$ is the surface temperature;, $B(\nu,T_s)$ is the Planck function, and $T_P(z)$ is a temperature profile in the atmosphere. Equation (3.3) describes radiative transfer in the atmosphere in the absence of scattering. Atmospheric scattering should be taken into account in the 3.9-$\mu$m band during daytime, and the scattering term should be added to Eq. (3.4b). However, the CRTM v1.1 currently employed does not take into account scattering. Hence, at this writing, shortwave bands are not used for SST in the daytime, and the scattering term in Eq. (3.4b) is neglected.

The major problem of SST retrieval is atmospheric correction, i.e., decoupling the contribution of SST variations in the measured radiances from the effects of atmospheric absorption and scattering, taking into account the effect of surface emissivity. (e.g., Zavody et al., 1995; Smith et al., 1996; Berk et al., 1998, 2000; Garand, 2003; Merchant and LeBorgne, 2004; Merchant et al, 2008, 2009; Liang et al., 2009; Liang and Ignatov, 2010). The regression, inversion and hybrid SST algorithms considered in this ATBD approach this problem differently. The regression SST algorithms (split-window NLSST or triple-window MCSST) effectively account for the above effects by producing an average dependency of SST on BTs over all atmospheric and sea surface states within the matchup data set. The inversion algorithm fully relies on the RTM, adopts the first guess BTs from RTM simulations, and solves the set of RTM equations simultaneously for SST and certain atmospheric variables. The hybrid algorithm uses the first guess similarly to the inversion algorithm and establishes an average relationship between SST and BTs over all atmospheric and sea surface states within the matchup data set regression to relate deviations of SST and BT from the corresponding first guesses. These three approaches are discussed in more detail below.

### 3.4.2 Mathematical Description of the SST Algorithms

As a first approximation, TOA radiance in the TIR windows is a function of SST, atmospheric absorption, and a geometric factor. It was shown that when two measurements in two spectral bands are used, the two equations can be solved and SST can be estimated as a linear combination of several BTs (e.g., Prabhakara et al., 1974; McMillin, 1975). This technique is known as the multi-channel SST (MCSST). Nonlinear modifications to MCSST were also explored (Walton et al., 1998). The respective family of algorithms is termed the nonlinear SST (NLSST). The regression techniques introduced in the early 1970s, still continue to be used in NOAA operations with AVHRR (McClain et al., 1985; May et al., 1998) and NASA MODIS

(Brown and Minnett, 1999) processing, and they will continue to be employed in the NPOESS era with VIIRS data (Sikorski et al., 2002).

However, the regression techniques may not always be accurate enough to achieve the desirable accuracy or optimize SST retrievals. Due to suboptimal approximation of the inverse relationship between SST and observed BTs, regression SST estimates may include local biases of several tenths Kelvin, depending on observational conditions (e.g., Merchant et al., 2008; 2009). For example, the accuracy of regression SST is likely to degrade at extreme local zenith angles and total precipitable water vapor contents in the atmosphere.

The further improvement in accuracy of SST retrieval, in our opinion, can explore two recent developments. First, the global analysis fields of SST, such as Reynolds Weekly SST (WSST) Daily High-Resolution Blended SST (DSST) (Reynolds et al., 2007), and Operational SST and Sea Ice Analysis (OSTIA - Stark et al., 2007, 2008), as well as atmospheric variables from the numerical weather prediction (NWP) models, e.g., National Center for Environmental Prediction Global Forecast System, or NCEP GFS (http://nomad3.ncep.noaa.gov/pub/gfs/rotating/) are currently synthesized from satellite observations and *in situ* data on a regular basis. Interpolation of analyses of SST fields to the sensor's pixels provides first-guess SST estimates ($T_{FG}$), whose accuracy and precision (~0.5K) are comparable with that of satellite retrievals. Second, fast RTMs, such as the CRTM (e.g., Han et al., 2006) now enable NRT simulations of clear-sky BTs ($T_{CS}$) using the analysis SST and upper air fields as input. Given $T_{FG}$ and $T_{CS}$, the SST retrieval problem can be posed in the incremental formulation, i.e., as restoring increments $\Delta T_S = T_S - T_{FG}$ from increments $\Delta T_B = T_B - T_{CS}$ (rather than $T_S$ from $T_B$, as in the classical regression formulation). Throughout this document, the term "SST increment" refers to deviations of retrieved (or *in situ*) SST from $T_{FG}$, and the term "BT increment" refers to deviations of $T_B$ from $T_{CS}$. With $T_{CS}$ simulated from real-time analysis fields, the incremental approach has the potential to more comprehensively account for atmospheric transmission than is possible with the conventional regression. In addition, the incremental formulation is more favorable to linear retrieval algorithms.

The difficulty of the incremental approach compared to conventional regression is that the signal-to-noise ratio (SNR) in $\Delta T_B$ is much lower than in $T_B$. The range of $T_B$ variations is ~30K, whereas the range of variations in $\Delta T_B$, is on the order of RMS error of modeling BTs with CRTM ( ~ 0.5 K - Liang et al., 2009; Petrenko et al., 2010). This is only a factor of ~4 larger than the upper estimate of RMS thermal noise in the AVHRR channels (RMSD<0.12 K – Robel et al., 2009) and ~5 times greater than the expected RMS thermal noise for ABI (Table 2.2). In addition to thermal noise, $\Delta T_B$ is contaminated with that part of $T_{CS}$ modeling error, which is due to inaccuracy of simulated atmospheric transmission (the part of $\Delta T_B$, caused by $\Delta T_S$ itself, is a useful signal). While the systematic part of the $\Delta T_B$ error (bias) can be corrected prior to $\Delta T_S$ retrieval, the retrieval algorithm still has to handle its random part.

For example, the OE technique (e.g., Rodgers, 1976) has been recently applied to SST retrieval from AVHRR (Gemmill et al., 2007; Merchant et al, 2008) and MSG SEVIRI (Merchant et al, 2009) data. In all implementations, correction of $\Delta T_B$ biases preceded application of the OE technique. Random variations in the atmospheric transmission were accounted for by solving a set of RTM equations simultaneously for $T_S$ and atmospheric variables such as average temperature and average water vapor mixing ratio (Gemmill et al., 2007) or TPW (Merchant et al, 2008, 2009). Merchant et al. (2009) have found that, at least in the case of $T_S$ retrieval from

observations in two bands, 11 and 12μm, the OE underestimates spatial and temporal $T_S$ variations. This is because the OE constructs the solution of the ill-conditioned set of RTM equations as a combination of observational and *a priori* information, which biases the solution towards the first guess. As shown in this ATBD, underestimation of SST variations can be in general mitigated by adjustment of the weights, with which observational and *a priori* information are combined in the OE solution. This adjustment does not follow from the OE theory, but rather should be made empirically, based on additional information. This information, for example, can be obtained from matchups of satellite BTs and *in situ* SST. This reduces the value of the pure physical (OE) approach, based solely on RTM inversion.

As an alternative to the inversion approach, we have developed another incremental RTM-based algorithm – the hybrid -- which avoids inversion of ill-conditioned sets of RTM equations using regression, which relates deviations of SST from the first guess with deviations of observed BTs from simulated BTs.

### 3.4.2.1 Regression Algorithms

The selected regression algorithms used for day and night are shown in Eqs (3.5) and (3.6). These equations were initially derived for AVHRR, are also currently used for MODIS, and are planned to be used for VIIRS. The nonlinear SST algorithm (NLSST) does not use the 3.9 μm band, which makes it applicable during both day and night:

$$T_R = a_0 + a_1 T_{11} + a_2 (T_{FG} - 273.15) (T_{11} - T_{12}) + a_3 (T_{11} - T_{12})(\sec\theta - 1). \quad (3.5)$$

The multi-channel SST algorithm (MCSST) uses the 3.9-μm band and is applicable only in the nighttime, when this band is not contaminated by sunlight scattering and reflection:

$$T_R = a_0 + a_1 T_4 + a_2 T_{11} + a_3 T_{12} + a_4 (T_4 - T_{12})(\sec\theta - 1) + a_5 (\sec\theta - 1). \quad (3.6)$$

In (3.5, 3.6), $T_R$ is regression SST estimate, $T_4$, $T_{11}$ and $T_{12}$ are brightness temperatures (BT) in 3.9, 10.8 and 12 μm bands, $T_{FG}$ is first guess (*a priori*) SST (climate or analyses/forecast SST, *e.g.*, Reynolds), $\theta$ is local zenith angle at the surface, and $a$'s are regression coefficients computed from matchups of *in situ* SST $T_{IS}$ with observed BTs. All temperature values are K degrees. Customarily, coefficients ($a$'s) are calculated early in each satellite's mission empirically against *in situ* SST, using 1–3 months of match-ups. Alternatively, they can also be calculated using RTM simulations. In this case, bias correction against *in-situ* is still needed.

As was mentioned earlier, inaccuracy of approximating the inverse SST/BT relationship with (3.5) and (3.6) causes local biases in regression SST estimate $T_R$. Using RTM simulations, the bias component can be extracted from $T_R$. The regression equation can be written as follows:

$$T_R = a_0 + \mathbf{a}^{\mathbf{T}}\mathbf{Y}. \quad (3.7)$$

Here, **a** is a vector of regression coefficients and **Y** is a vector of regressors. In NLSST formulation, for example, **a** is three-dimensional vector, $\mathbf{a}=[a_1,a_2,a_3]^T$ and **Y** is a three-dimensional vector function of observed BTs, $T_{11}$ and $T_{12}$, $T_{FG,}$ and $\theta$:

$$\mathbf{Y}(T_{11,}\, T_{12,}\, T_{FG,}\, \theta) = \mathbf{\Phi}(T_{11,}\, T_{12,}\, T_{FG,}\, \theta), \quad (3.8)$$

$$\mathbf{\Phi}(T_{11,}\, T_{12,}\, T_{FG,}\, \theta)^{\mathbf{T}} = [T_{11}, (T_{11} - T_{12})(T_{FG} - 273.15), (T_{11} - T_{12})(\sec\theta - 1)]. \quad (3.9)$$

Customarily, regression coefficients are calculated from a set of matchups between the *in situ* SSTs ($T_{IS}$) and observed BTs $T_B$ using a least squares method:

$$\mathbf{a} = S_{YY}^{-1}\mathbf{S_{YT}}, \tag{3.10}$$

$$a_0 = \langle T_{IS}\rangle - \mathbf{a}^{\mathbf{T}}\langle \mathbf{Y}\rangle. \tag{3.11}$$

$S_{YY}$ is a covariance matrix of $\mathbf{Y}$ over the matchup data set and $\mathbf{S_{YT}}$ is a covariance of $\mathbf{Y}$ and $T_{IS}$. The angle brackets <> denote averaging over the matchup data set. The expression (3.11) ensures that $T_R$ is unbiased with respect to $T_{IS}$ within the matchup data set. Typically, the global bias of regression SST increment $\Delta T_R = T_R - T_{FG}$ is small as the first-guess field $T_{FG}$ is anchored to $T_{IS}$. The formalism of conventional regression, however, does not prevent local bias in $\Delta T_R$ from being a function of observational conditions. The local bias term can be extracted from $\Delta T_R$, using the following expansion of $\mathbf{Y}$:

$$\mathbf{Y} = \mathbf{Y_{CS}} + \mathbf{\Delta Y}, \tag{3.12}$$

$\mathbf{Y_{CS}}$ is approximation of $\mathbf{Y}$ with simulated clear-sky BTs $T_{CS11}$ and $T_{CS12}$:

$$\mathbf{Y_{CS}} = \mathbf{\Phi}[T_{CS11}(T_{FG}, \mathbf{x}, \theta), T_{CS12}(T_{FG}, \mathbf{x}, \theta), T_{FG}, \theta], \tag{3.13}$$

$\mathbf{x}$ is a vector of GFS atmospheric variables and $\mathbf{\Delta Y} = \mathbf{Y} - \mathbf{Y_{CS}}$:

$$\mathbf{\Delta Y} = \mathbf{\Phi}[\Delta T_{B11}(T_{FG}, \mathbf{x}, \theta), \Delta T_{B12}(T_{FG}, \mathbf{x}, \theta), T_{FG}, \theta], \tag{3.14}$$

$\Delta T_{B11}$ and $\Delta T_{B12}$ are BT increments: $\Delta T_{B11} = T_{B11} - T_{CS11}$ and $\Delta T_{B12} = T_{B12} - T_{CS12}$. Substituting (3.12) into (3.7), we decompose $\Delta T_R$ into a "local bias" component $\Delta T_L$ and an "information" component $\Delta T_I$:

$$\Delta T_R = \Delta T_I + \Delta T_L, \tag{3.15}$$

$$\Delta T_I = \mathbf{a}^{\mathbf{T}}\,\mathbf{\Delta Y}, \tag{3.16}$$

$$\Delta T_L = a_0 + \mathbf{a}^{\mathbf{T}}\mathbf{Y_{CS}} - T_{FG}. \tag{3.17}$$

According to (3.14, 3.16), $\Delta T_I = 0$ when $T_{11} = T_{CS11}$ and $T_{12} = T_{CS12}$, and, in this sense, $\Delta T_I$ is the unbiased response of $\Delta T_R$ to variations in $\Delta T_{B11}$ and $\Delta T_{B12}$. In contrast, according to (3.13, 3.17), $\Delta T_L$ represents local bias of $\Delta T_R$, which does not depend on observations but is a function of $\theta$ and RTM input variables.

### 3.4.2.2 Inversion Algorithm

The inversion algorithm is intended to improve the atmospheric correction for SST in two ways. First, if the approximation of $T_B$ with $T_{CS}$ simulated from first-guess analysis SST and GFS atmospheric variables is accurate enough, it can reduce local SST biases compared to the case of the regression algorithm. Second, the inversion algorithm accounts for random deviations of the atmospheric transmission from the first guess by simultaneous retrieval of SST and one or two atmospheric variables, depending on the number of used sensor bands. In the implementation of the RTM inversion algorithm for SEVIRI, we used two unknowns, SST and the Optical Depth Scaling Factor (ODSF) $\beta$, defined as the ratio of the optical depth of water vapor absorption $\tau$ to its value, computed from GFS data $\tau_{FG}$:

$$\beta = \tau / \tau_{FG}\,, \tag{3.18}$$

The corresponding set of RTM equations can be written as follows:

$$F(T_S, \beta)=T_B+\eta \quad (3.19)$$

Here, $\mathbf{F}(T_S, \beta)$ is a vector RTM function, $\mathbf{T_B}$ is a vector of observed brightness temperatures, $\boldsymbol{\eta}$ is instrumental noise.

To solve (3.19), the unknown variables are represented in the incremental form:

$$T_{INV} = T_{FG} + \Delta T_{INV}, \quad (3.20a)$$

$$\beta = 1+\Delta\beta, \quad (3.20b)$$

$$\mathbf{T_B} = \mathbf{T_{CS}} + \mathbf{\Delta T_B}. \quad (3.20c)$$

Here, $\Delta T_{INV}$, $\Delta\beta$ and $\mathbf{\Delta T_B}$ are the increments, i.e., deviations of the corresponding variables from the first guess. Using (3.20), (3.19) can be linearized and brought to the incremental form:

$$K\mathbf{Z} = \mathbf{\Delta T_B} + \boldsymbol{\eta}, \quad (3.21)$$

where $\mathbf{Z}^T = [\mathbf{\Delta}T_S, \mathbf{\Delta}\beta]^T$, K is the Jacobian of $\mathbf{F}(T_S, \beta)$ at $T_S = T_{FG}$ and $\beta = 1$. In general, set of Eqs (3.21) is ill-conditioned, i.e., its solution is not stable with respect to noise and other disturbing factors and requires stabilization with *a priori* information on $\mathbf{\Delta Z}$. The OE technique assumes that $\mathbf{Z}$ is a random vector with known Gaussian statistical distribution and produces the Bayesian estimate of the vector $\mathbf{Z}$ as

$$\mathbf{Z} = (K^T\Delta^{-1}K + S^{-1})^{-1}K^T\Delta^{-1}\,\mathbf{\Delta T_B}, \quad (3.22)$$

Here $\Delta$ is a covariance matrix of measurement errors and S is *a priori* covariance matrix of $\mathbf{\Delta Z}$. The drawback of OE is that as discussed above, the solution (3.22) is biased towards the first guess (Merchant et al, 2008), suppressing spatial and temporal variations in the retrieved SST (Merchant et al., 2009). In general, this artificial bias in $T_{INV}$ can be reduced (but not removed completely) by empirical adjustment of diagonal elements of S in (3.22). This adjustment, however, cannot be derived from RTM or *a priori* information and requires additional knowledge of the magnitude of expected SST variations.

### 3.4.2.3 Hybrid Algorithm

The objective of GOES-R SST algorithm development is to combine the strong points of the regression and inversion approaches into a hybrid algorithm, as shown in Fig. 3.6. Similarly to the expression (3.20a) for the inversion algorithm, the hybrid SST estimate $T_H$ is a sum of the first guess and the increment:

$$T_H = T_{FG} + \Delta T_H \quad (3.23)$$

The difference with the inversion algorithm is that the hybrid algorithm increment $\Delta T_H$ is calculated from regression between *in situ* SST increments $\Delta T_{IS} = T_{IS} - T_{FG}$ and the vector of incremental regressors $\mathbf{\Delta Y}$:

$$\Delta T_H = b_0 + \mathbf{b}^T\mathbf{\Delta Y}(T_{FG}, \mathbf{x}, \theta) \quad (3.24)$$

Here $b_0$ is the offset and $\mathbf{b}$ is the vector of hybrid regression coefficients. Considering the hybrid algorithm in NLSST formulation, $\mathbf{b}$ has three components, $\mathbf{b}^T = [b_1,b_2,b_3]$ and $\mathbf{\Delta Y}$ is defined by (3.14). Compared to the conventional regression, calculation of regression coefficients from

matches of $\Delta T_{IS}$ with $\Delta T_B$ rather than from matches of $T_{IS}$ with $T_B$ has two advantages. First, since the equation (3.24) does not include the "bias" term, unlike (3.15), the local bias of $T_H$ with respect to $T_{FG}$ is expected to be small. Second, the vector of hybrid coefficients **b** can be selected in such a way as to maximize correlation between $\Delta T_H$ and $\Delta T_{IS,}$ which additionally improves the accuracy of fitting $\Delta T_{IS}$ with $\Delta T_B$.

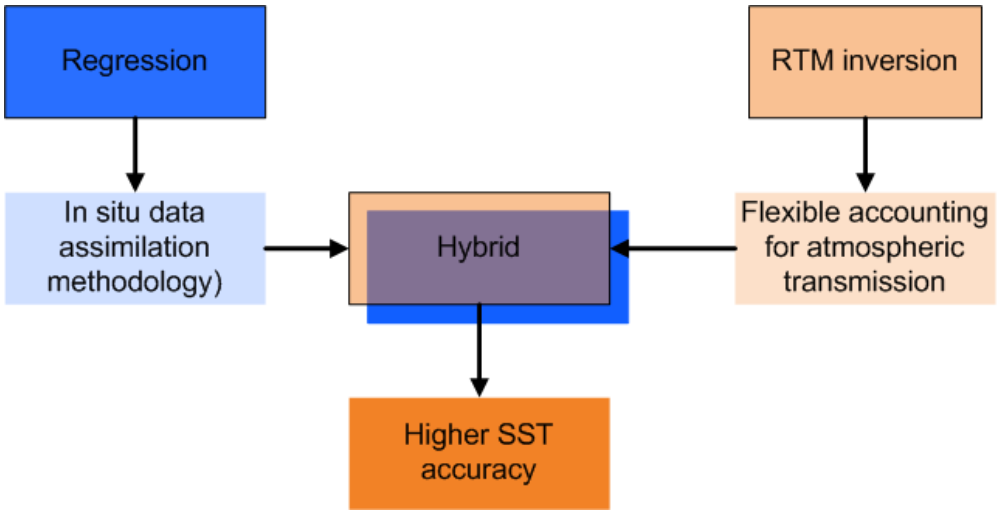


**Figure 3.6** *Merging regression and inversion methodologies: the hybrid SST algorithm.*

Compared to the inversion algorithm, the hybrid approach also has two advantages. First, with properly chosen coefficients (see below), $T_H$ is not biased towards $T_{FG}$. Second, if the estimate of the RTM Jacobian K in (3.21) is not accurate enough, the equation (3.24) with coefficients, derived from matches of BT and *in situ* SST increments can provide more accurate SST estimates than the equation (3.22).

On the other hand, computing hybrid coefficients is a more complicated task than computing conventional regression coefficients. The straightforward way to estimate the hybrid coefficients would be to use least-squares estimates $\mathbf{b_{LS}}$ and $b_{0LS}$:

$$\mathbf{b_{LS}} = S_{\Delta Y \Delta Y}^{-1} \mathbf{S_{\Delta Y \Delta T}}, \quad (3.25)$$

$$b_{0LS} = \langle \Delta T_{IS} \rangle - \mathbf{b_{LS}}^{\mathbf{T}} \langle \mathbf{\Delta Y} \rangle, \quad (3.26)$$

Here $S_{\Delta Y \Delta Y}$ is a covariance matrix of $\mathbf{\Delta Y}$ over the matchup data set and $\mathbf{S_{\Delta Y \Delta T}}$ is a covariance of $\mathbf{\Delta Y}$ and $\Delta T_{IS}$. The coefficients $\mathbf{b_{LS}}$ and $b_{0LS}$ minimize RMS error between the left-hand and right-hand parts of (3.24) and maximize correlation between $\Delta T_H$ and $\Delta T_{IS}$. However, the estimates (3.25, 3.26) may not be accurate. As it is known from regression analysis (e.g., Seber, 1977), the least square method guarantees that regression coefficients are unbiased only if values of the regressors are accurate. In the case of regression between $\mathbf{\Delta Y}$ and $\Delta T_{IS,}$ the ranges of regressors' variations are much smaller compared to errors in regressors and compared to the conventional regression. As a result, the SST estimate (3.24) with coefficients $\mathbf{b_{LS}}$ and $b_{0LS}$ underestimates temporal and spatial SST variations. To avoid this undesirable effect, we modify $\mathbf{b_{LS}}$ by "inflating" it in such a way as to equalize variance of $\Delta T_H$ with variance of the "information" component of regression SST $\Delta T_I$. The corresponding algorithm is described below.

1. The conventional regression coefficients **a** is calculated from (4.8, 4.9)

2. The least square estimate of hybrid coefficients is calculated from (4.23) and (4.24)

3. The variances of $\Delta T_I$ and $\Delta T_{HLS}$, $D_1$ and $D_{HLS}$ are estimated as

$$D_1 = <( \mathbf{a}^{\mathbf{T}}(\mathbf{\Delta Y}-<\mathbf{\Delta Y}>))^2> \quad (3.27)$$

$$D_{HLS} = <( \mathbf{b_{LS}}^{\mathbf{T}}(\mathbf{\Delta Y}-<\mathbf{\Delta Y}>))^2> \quad (3.28)$$

4. The final estimates of hybrid coefficients are found as

$$\mathbf{b} = (D_1/D_{HLS})^{0.5}\, \mathbf{b_{LS}}, \quad (3.29)$$

$$b_0 = \langle T_{IS} \rangle - \mathbf{b}^{\mathbf{T}} \langle \mathbf{\Delta Y} \rangle, \quad (3.30)$$

By construction, the variance of the hybrid SST increment $\Delta T_H$, calculated with the coefficients (3.10) and (3.11), is equal to $D_I$ and the correlation of $\Delta T_H$ and $\Delta T_{IS}$ is the same as in the case of using the least-squares coefficients $\mathbf{b_{LS}}$ and $b_{0LS}$.

As it follows from descriptions of inversion and hybrid algorithms, the problem of underestimation of SST variations does exist with both incremental algorithms. In the case of the hybrid algorithm, this problem is solved by estimating the variance of regression SST from the data set of matchups by equalizing the variances of regression and hybrid SST. The pure inversion methodology does not use *in situ* matchups and, hence, it does not allow adjustment of retrieved SST variance.

## 3.4.3 SST Quality Control

### 3.4.3.1 The Concept and the Structure of SST Quality Control

Typically, only about 15% of ocean pixels are cloud-free to the extent that they are usable for SST retrieval from thermal IR measurements. The task of SST quality control (QC) is to separate the usable and unusable pixels for SST. Within the GOES-R ABI processing system, preliminary cloud masking will be done with a special module, ABI cloud mask (ABI CM). ABI CM will be run upstream of other product modules and provide them with preliminary information on presence/absence of clouds. Since the product modules may define "pixel usability" differently, ABI CM is anticipated to perform cloud screening judiciously in order to preserve any pixels which might be useful for any surface-oriented ABI application. This strategy suggests that individual product modules may include their own product-specific QC.

The SST QC module classifies ocean pixels into three categories: "Optimal," "Sub-Optimal", and "Poor" in terms of using them for SST. The basic concept of the SST QC is testing observed BTs for consistency with CRTM (Petrenko et al., 2010). The model is adequate to observations if, first, it fits the observations with the predefined accuracy and, second, the values of model variables, at which this accuracy is achieved, are within the predefined range (e.g., Y. Bard, 1973). In the context of cloud masking, this means that in clear-sky areas over ocean CRTM is expected to fit the observed BTs at realistic values of the model's input variables. *A priori* information, needed for the adequacy check, includes NWP expectations of those atmospheric and surface variables, which are the input for CRTM, and the limits on realistic variations in those variables which participate in fitting observations.

The methods by which this concept is implemented for AVHRR and SEVIRI are somewhat different. Initially, the SST QC was developed for regression SST, operationally produced from AVHRR measurements. Since the regression algorithm involves retrieval of only one variable, SST, and the regression fits the inverse SST/BT relationship only approximately, the accuracy of approximation of observed BTs with regression SST was limited. For SEVIRI, the inversion SST algorithm has been implemented. As described in Section 4.2.2, the inversion algorithm simultaneously retrieves two variables, SST and ODSF ($\beta$), which allows more accurate fitting of observed BTs with CRTM in clear-sky pixels. Here we describe the implementation of SST QC for SEVIRI.

The pixel is classified "Poor" by QC if it fails at least one of the following tests:

- RTM test, in which the accuracy of fitting observed BTs with CRTM and regression SST is evaluated.
- Static SST test, which rejects the pixel if retrieved SST is lower than the liberal physically realistic limit.
- Adaptive SST test, which refines the classification by the static SST test based on analysis of statistics of "optimal" and "poor" pixels in the neighborhood of a given pixel.
- Optical depth test, which verifies if the retrieved $\beta$ value is realistic for clear-sky conditions.
- SST uniformity test, which tests the pixels passing the consistency check and detects residual subpixel clouds by elevated spatial variability of SST in the immediate neighborhood of a given pixel.

### 3.4.3.2 SST QC Tests

*a. RTM test*

The RTM test verifies accuracy of fitting the vector of observed BTs, $\mathbf{T}_B$, with the clear-sky vector of simulated BTs $\mathbf{T}_{CS}(\mathbf{y}, \mathbf{x}, \theta)$. Here $\mathbf{y}$ is a vector of retrieved variables and $\mathbf{x}$ is a vector of GFS atmospheric variables, which are not retrieved but used as input for CRTM. The tested condition for the pixel being "Optimal" is:

$$[\mathbf{T}_B - \mathbf{B}_{BT} - \mathbf{T}_{CS}(\mathbf{y},\mathbf{x},\theta)]^T \Delta^{-1} [\mathbf{T}_B - \mathbf{B}_{BT} - \mathbf{T}_{CS}(\mathbf{y},\mathbf{x},\theta)]/N < D_{BT} \quad (3.31)$$

If the above condition is met, the pixel is set to "Optimal;" otherwise it is set to "Poor." Here, $\mathbf{B}_{BT}$ is the vector of BT biases estimated as discussed in Section 4.4, $N$ is the number of channels used in SST retrieval; for SEVIRI, N=2 (Ch10 and Ch11). The vector $\mathbf{y}$ includes two variables, inversion SST $T_{INV}$ and ODSF. $\Delta$ is a covariance matrix of errors, which accounts for measurement noise and errors of fitting $\mathbf{T}_B$ with $\mathbf{T}_{CS}$. $\Delta$ is diagonal, with all diagonal elements equal to 25 $K^{-2}$, assuming that the RMS noise level in SEVIRI channels is 0.2 K. The threshold $D_{BT}$ is set to1.

*b. Static SST test*

The predictor for the static SST test is hybrid SST increment $\Delta T_H$, corrected for the bias $B_{SST}$. $B_{SST}$ is estimated as described in Section 4.4. The hybrid SST is used as input in the static and adaptive SST tests because the hybrid algorithm is considered as the baseline SST algorithm. However, the results of these tests are applicable with a good accuracy to regression SST $T_R$ and inversion SST $T_{INV}$. The test cuts off obviously unrealistic negative $\Delta T_H$ with the following condition:

$$\Delta T_H - B_{SST} > D_{SST}? \tag{3.32}$$

If yes, then the pixel is set to "Optimal;" otherwise, it is set to "Poor." The threshold $D_{SST}$ is location and time specific and depends on the estimate of RMS accuracy of the reference SST for this pixel, $\sigma_{SST}$. The SST reference field can be either Weekly Reynolds OISST (WSST - Reynolds et al., 2002) or Daily High-Resolution Reynolds Blended SST (DSST - Reynolds et al., 2007). The DSST data set includes the $\sigma_{SST}$ estimate on the same $0.25^o$ grid as for SST itself. For WSST, the estimate of $\sigma_{SST}$ deemed proportional to the maximum spatial SST difference within the window of 3×3 nodes ($2^o \times 2^o$). $D_{SST}$ is defined as follows:

$$D_{SST} = \min(-3\sigma_{SST}, -2\text{K}) \tag{3.33}$$

The values of $\sigma_{SST}$ typically vary from 0.1 K to 0.7 K, depending on location; hence, $D_{SST}$ is close to -2 K for most of the world's ocean. The liberal setting of the threshold reduces the chance of false cloud detections. On the other hand, it may cause misclassifications of cloudy pixels as "Optimal," especially at the boundaries of cloudy systems, often surrounded with relatively warm ambient cloudiness.

*c. Adaptive SST test*

The adaptive SST test further refines the initial classification by the static SST test. It detects ambient cloudiness at the boundaries of cloudy systems, initially determined with condition (3.32). The test analyzes local statistics of $\Delta T_H$ in "Optimal" and "Poor" clusters within a sliding window, surrounding the tested pixel. The size of the sliding window for SEVIRI was empirically chosen to be 11×11 pixels. All "Optimal" pixels within the window are tested with the following condition:

$$\rho_{\text{CLD}} \geq \rho_{\text{CLR}} \tag{3.34}$$

If yes, then the pixel is set to "Optimal;" otherwise it is set to "Poor." $\rho_{\text{CLD}}$ in (3.34) is the difference between $\Delta T_H$ in a given pixel and mean $\Delta T_{CLD}$ averaged over "Poor" pixels within the sliding window, normalized to STD $\sigma_{CLD}$ of $\Delta T_S$ over "Poor" pixels within the same window:

$$\rho_{\text{CLD}} = |\Delta T_H - \Delta T_{CLD}| / \sigma_{CLD}, \tag{3.35a}$$

and $\rho_{\text{CLR}}$ is $\Delta T_H$ normalized to $\sigma_{CLR} = D_{SST}/3$:

$$\rho_{\text{CLR}} = |\Delta T_H| / \sigma_{CLR}. \tag{3.35b}$$

Parameters $\Delta T_{CLD}$ and $\sigma_{CLD}$ are subject to change on each iteration if new pixels are classified as "Poor" according to condition (3.33). The procedure repeats itself until either the classification of the pixels within the window stabilizes or the tested (central) pixel in the window becomes "Poor."

*d. Optical depth test*

The optical depth test compares the retrieved value of ODSF $\beta$ against the predetermined threshold $D_\beta$:

$\beta > D_\beta$? (3.36)

If yes, than the pixel is marked as "Poor". Considering that the probability of clouds increases with negative SST deviations from the reference SST, the threshold $D_\beta$ is dependent on the retrieved hybrid SST increment:

$\Delta T_H > 0$: $D_\beta = 1.0$ (3.37a)

$-2\text{K} \le \Delta T_H \le 0$: $D_\beta = 1.1 + 0.05\,\Delta T_H$, (3.37b)

$\Delta T_H < -2\text{K}$: $D_\beta = 1.1$ (3.37c)

*e. The SST spatial uniformity test*

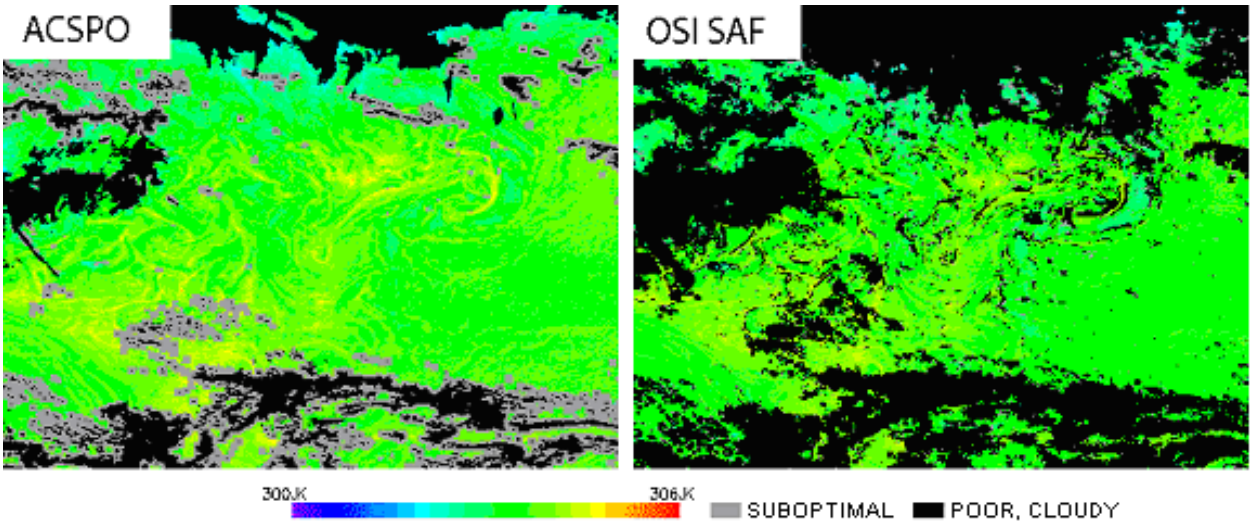


**Figure 3.7** *SST images of a part of the Gulf of Mexico, produced from Metop-A nighttime AVHRR Full Resolution Area Coverage Mode (FRAC) measurements on 7 July 2009 with ACSPO (left) and by the EUMETSAT Ocean & Sea Ice Satellite Application Facility (OSI SAF – right).*

Residual subpixel clouds, missed by other cloud tests, can be detected by higher spatial variability in BT and retrieved SST. This concept forms the foundation of the texture, or spatial uniformity, tests used in many cloud masking algorithms. Usually, the predictor for the texture test is spatial RMS variation in BT in the immediate neighborhood of a given pixel. The potential risk of using this predictor is possible false detection of clouds in clear-sky ocean areas with high thermal gradients.

In SST QC, the implementation of the uniformity test has the following features. First, it analyzes the field of retrieved SST ($T_H$ for SEVIRI) rather than observed BTs, i.e., residual cloud contaminations are screened out directly from the SST product. Second, the predictor for the SST

uniformity test is STD of the difference $T_S$ – median($T_S$) rather than STD of $T_S$. Median($T_S$) is the $T_S$ field, passed through the 2D median filter. The window size in the median filter is set to 3×3 pixels to avoid an excessive loss of "Optimal" pixels. The threshold for the uniformity test is selected to be somewhat above the RMS level of random noise in SST. The median filter is known to preserve regular contrasts but suppress random noise (e.g., Gonzalez and Woods, 2003). As a result, the difference $T_S$ – median($T_S$) is more sensitive to random variations in $T_S$, typical for sub-pixel cloud effects, than to more regular surface contrasts caused by ocean thermal fronts. This reduces the risk of misclassification of ocean fronts as cloudy pixels.

As an example, Fig. 3.7 shows the SST images of a part of the Gulf of Mexico, produced from Metop-A nighttime Full Resolution Area Coverage measurements on 7 July 2009 at NOAA with the ACSPO, using the median uniformity test, and at the EUMETSAT Ocean and Sea Ice Satellite Application Facility (OSI SAF – LEO SST User Manual, 2009). The pixels classified as "Sub-Optimal" with the SST QC uniformity test are marked gray on the left image. The pixels classified as "Poor" by ACSPO (left image) and those classified "Poor" by O&SI SAF (right image) are marked black. The comparison of the two images shows that ACSPO, using the median-based SST uniformity test, better preserves thin spatial structure of SST.

### 3.4.4 Estimation of Global Biases

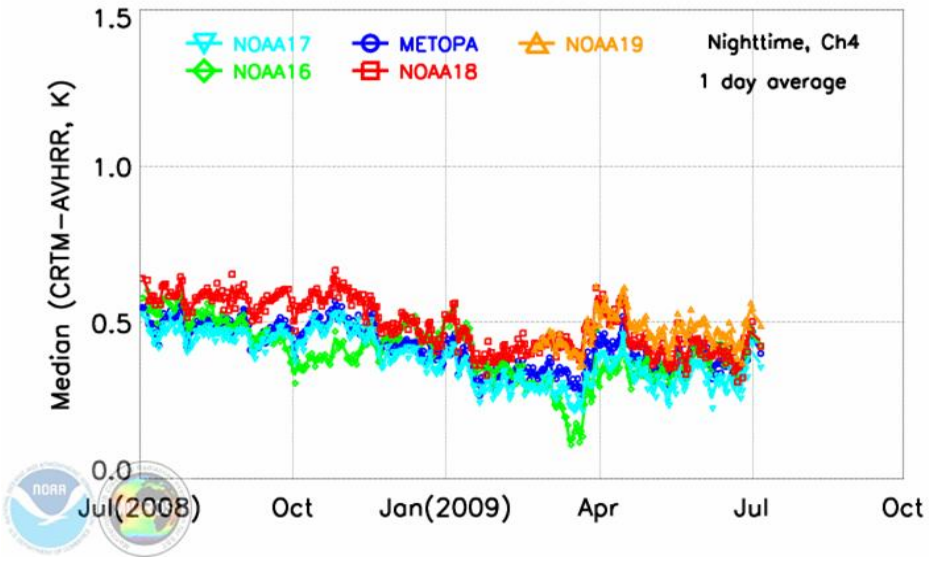


**Figure 3.8** *Model minus Observation biases in AVHRR Ch4 (10.8 μm). Model does not include aerosol, uses bulk Reynolds SST (instead of skin), and does not account for effect of SST diurnal cycle. Warm bias of several tenths of a degree Kelvin is consistent for 5 AVHRRs. Causes: CRTM (no aerosol; bulk SST instead of skin; no diurnal correction) and AVHRR (residual cloud). Data are from the MICROS web-based tool, www.star.nesdis.noaa.gov/sod/sst/micros/*

Both inversion and hybrid algorithms require correction of biases between observed and simulated BTs, at least in a global average sense, otherwise these biases will be translated to biases in retrieved SST. Figures 3.8-3.9 show model minus observation (M-O) global mean

biases for AVHRR channel 4 (10.8 μm), and for SEVIRI channels 4 (3.9 μm), 9 (10.8 μm) and 10 (12.0 μm). In the longwave AVHRR Channel 4 and SEVIRI Channels 9 and 10, M-O biases are positive and within several tenths K. The warm bias is due to the facts that the current CRTM v1.1 does not account for the effects of aerosols, and that the bulk Reynolds SST used as input to CRTM was not converted to skin, and was not corrected for the effect of the diurnal cycle. Additionally, AVHRR and SEVIRI BTs may be biased cold due to residual or ambient clouds (e.g., Dash and Ignatov, 2008; Liang et al., 2009). All these factors lead to positive M-O biases. Figure 3.9 additionally shows that bias in shortwave SEVIRI Channel 4 is unrealistic and inconsistent with AVHRR bias. As of this writing, this anomaly was not resolved. As a result, all algorithms considered in this ATBD for SEVIRI are two-channel split-window formulation and do not employ the 3.9-μm band. The two-band formulation provides consistency between daytime and nighttime retrievals but gives a "worst case" estimate of SST performance at night. Based on AVHRR analyses, adding the shortwave band is expected to improve SST accuracy. The global BT bias evaluation algorithms were developed and preceded inversion SST retrieval. Correction of biases in simulated BTs and retrieved SST is also performed within QC, as discussed in Section 4.3.

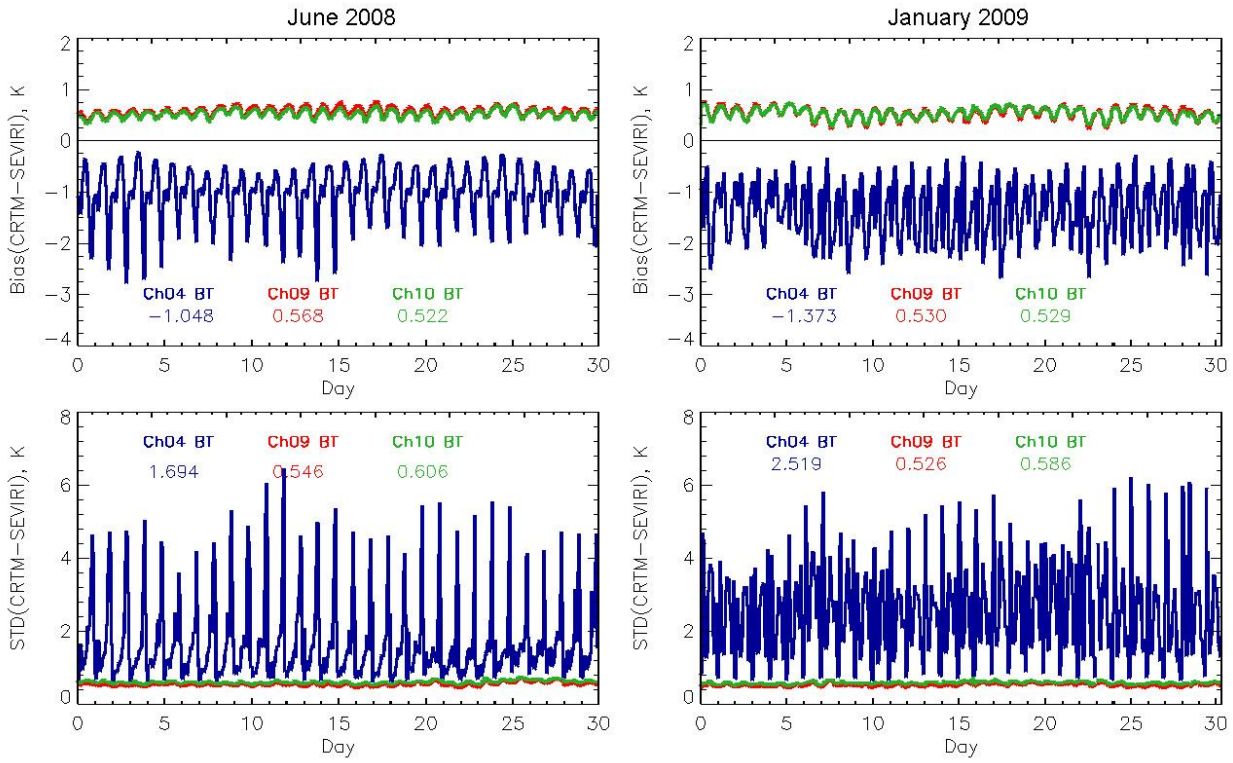


**Figure 3.9** *Model minus Observation biases in SEVIRI BTs in June 2008 (left) and January 2009 (right). In longwave bands, SEVIRI M-O biases are +0.5K and consistent with AVHRR. In shortwave bands, the M-O biases are negative and inconsistent with AVHRR. During daytime, M-O biases are large and highly variable, due to inaccurate modeling of solar reflectance.*

The SST and BT biases may vary in time because of sensor calibration trends and orbital drift. Therefore, the biases are estimated on-line and accounted for in the corresponding QC tests and

in the inversion SST algorithm. The most common method of clear-sky bias estimation is to average the deviations (increments) of $T_S$ from $T_{FG}$ and $T_B$ from $T_{CS}$ over "clear" pixels, determined with a clear-sky mask (e.g., Merchant et al., 2006; Liang et al., 2009). However, this method may create undesirable cross-talk between the classification of pixels by QC and the bias estimates. To avoid this crosstalk, the biases are estimated within ACSPO independently from and prior to QC as positions of peaks of incremental histograms, accumulated over all ocean pixels, before separation the pixels into "optimal," "sub-optimal," and "poor". Though the percentage of "optimal" ocean pixels is typically only about 15%, the increments, corresponding to "optimal" pixels, are concentrated in a relatively narrow range and form the peaks of all-sea-pixels histograms.

The SEVIRI-ACSPO code includes estimation of global biases in simulated clear-sky BTs and hybrid SST. The estimates of $B_{BT}$ and $B_{SST}$ are used in the QC tests and the estimates of $B_{BT}$ are also accounted for in the inversion SST algorithm. It is important to note that the estimates of biases for QC and for the inversion algorithm are produced by averaging over different time periods. In general, variations of instant global biases in observed BTs and retrieved SST for SEVIRI include three components with different time scales:

- The high-frequency component includes short-term variations of biases between sequential images.
- The diurnal component is due to the diurnal warming cycle and has a time period of 24 hours and the peak-to-peak magnitude of about 0.3 K.
- The low-frequency component of BT and SST bias is caused by calibration trends on the time scale of several months.

One of the goals of SST retrieval from geostationary satellites is monitoring diurnal SST variability. To preserve the diurnal component in retrieved SST, the bias correction for the inversion SST algorithm should account for bias, averaged over the period of several days. In the ACSPO-SEVIRI code, the global biases for SST retrieval are averaged over 3 to 6 days, depending on the time interval between sequentially processed images (15 or 30 min). The RTM and SST tests of the SST QC are based on comparison of observed BT and retrieved SST with reference values, which do not track diurnal variations. Consequently, the diurnal component should also be removed from observed BTs and retrieved SST before using them in the SST QC tests. As a result, the integration time for averaging biases for QC purposes is 2 to 4 hours. For every sequentially processed image, the instant values of $B_{BT}$ and $B_{SST}$ are estimated from all-ocean-pixel histograms of BT and hybrid SST increments and the averaged bias values are updated:

$$B_1 = V_1 \tag{3.38a}$$

$$B_i = kV_{i-1} + V_i,\ i>0 \tag{3.38b}$$

Here, $V_i$ is the global BT or SST bias for the $i^{th}$ processed image, i=1,2,….; $B_i$ is a recursively updated bias for the $i^{th}$ image $k = 0.992$ if the biases are averaged for inversion SST and $k = 0.75$ if the biases are averaged for SST QC tests.

## 3.5 Algorithm Output

***Table 3.10*** *SST algorithm output product and QC data.*

| Field Name | Type | Category | Description | Dimension |
|---|---|---|---|---|
| Retrieved SST | output | Product | Hybrid (primary) or Regression (back up) SST | grid (xsize, ysize) |
| Observation Conditions | output | QC | Observation Conditions mask (cf. Table 3.12) | grid (xsize, ysize) |
| SST QC Individual Tests | output | QC | Individual SST QC tests mask (cf. Table 3.12) | grid (xsize, ysize) |
| SST QC | output | QC | Overall Quality Control mask (cf. Table 3.12) | |

***Table 3.11*** *SEVIRI SST product output metadata.*

| Field | Description |
|---|---|
| 1 | -Date time of swath begin and end<br>-Bounding box information (resolution, num rows/columns, bytes per pixel)<br>-Instrument info (satellite, instrument, altitude, nadir, latitude/longitude, projection)<br>-Citation to documents |
| 2 | Product name and units |
| 3 | Algorithm type (Hybrid or Regression) |
| 4 | Number of Day, Night and Twilight 'Optimal' Retrievals |
| 5 | Number (and % from total) of ocean pixel with Optimal/Sub-Optimal/Poor/Unprocessed retrievals |
| 6 | Mean, Min, Max and STD of (SEVIRI – CRTM) BT for Ch 7, 11, 13, 14, 15 over 'Optimal retrievals' |
| 7 | Mean, Min, Max and STD of (SEVIRI – Reynolds) for the utilized algorithm type (Hybrid (or Regression SST) |

***Table 3.12*** *QC of the SST product specification (three 8-bits fields).*

| Bit(s) | Description |
|---|---|
| **Field 1: Observation conditions (packed 8-bit word)** | |
| 1 | Channel value Valid(0) / Invalid(1) |
| 2 | External CM Used (0) /Not used(1) |
| 3 | Night (0) /Day (1) |
| 4 | Ocean (0) /Land or Outer space (1) |
| 5 | No-glint (0) /Glint (1) |
| 6 | No ice (0) /Ice (1) |
| 7-8 | N/A |
| **Field 2: SST QC Individual tests (packed 8-bit word)** | |
| 1 | Radiance Test |
| 2 | Adaptive SST Anomaly test |
| 3 | Static SST Test |
| 4 | N/A |
| 5 | Optical Depth Test |
| 6 | N/A |
| 7 | Spatial Uniformity Test |
| 8 | N/A |
| **Field 3: SST QC (single variable 8-bit word)** | |

| | |
|---|---|
| 1-8 | SST QC Optimal (0) /Sub-Optimal (1) /Poor (2) /Not processed (3) |

# 4 TEST DATA SETS AND OUTPUT

## 4.1 Input Data Sets and Status of SST Retrieval Algorithms

The algorithms are verified and validated using ABI proxy data listed in Table 4.1.

***Table 4.1*** *ABI, AVHRR, and SEVIRI (and possibly MODIS) sensors used as its proxy.*

| Sensor | Band # | FOV, km | Band Center, µm | Bandwidth, µm | NEdT @300K |
|---|---|---|---|---|---|
| ABI | 7 | 2 | 3.9 | 0.2 | 0.10 |
| | 11 | 2 | 8.5 | 0.4 | 0.10 |
| | 13 | 2 | 10.4 | 0.5 | 0.10 |
| | 14 | 2 | 11.2 | 0.8 | 0.10 |
| | 15 | 2 | 12.3 | 1.0 | 0.10 |
| SEVIRI | 4 | 5 | 3.9 | 0.9 | 0.35(0.17) |
| | 9 | 5 | 10.8 | 2.0 | 0.25(0.11) |
| | 10 | 5 | 12.0 | 2.0 | 0.37(0.15) |
| AVHRR | 3B | 4 (1)* | 3.75 | 0.4 | <0.12 |
| | 4 | 4 (1)* | 10.8 | 1.0 | <0.12 |
| | 5 | 4 (1)* | 12.0 | 1.0 | <0.12 |
| MODIS | 20 | 1 | 3.75 | 0.18 | 0.05 |
| | 22 | 1 | 3.96 | 0.06 | 0.07 |
| | 31 | 1 | 11.0 | 0.50 | 0.05 |
| | 32 | 1 | 12.0 | 0.50 | 0.05 |

** AVHRR Global Area Coverage (GAC) data have 4km global resolution and the Local Area Coverage (LAC) have1km resolution. NB: AVHRR onboard MetOp-A provides global 1km data in the Full Resolution Area Coverage (FRAC) format.*

The primary proxy sensor used in the GOES-R development is the Spinning Enhanced Visible and Infra-red Imager (SEVIRI) onboard the European Meteosat Second Generation (MSG-1 and MSG-2) satellites. This sensor was selected because it is flown in a geostationary orbit and has spectral bands similar to the ABI. In this ATBD, two months of MSG-2 SEVIRI data (June 2008 and January 2009) are used to cross-evaluate SST retrievals.

However, SEVIRI radiometric and spectral characteristics and spatial resolution are not fully representative of ABI. To that end, AVHRR flown in a polar orbit is a better proxy for the ABI. Global Area Coverage (GAC) 4-km resolution global data of five AVHRR instruments (flown onboard NOAA-16, -17, -18, -19 and Metop-A) from 2001 to the present are used in this ATBD.

Combining analyses from MSG SEVIRI and AVHRR data provides sufficient insight into performance of the SST algorithms with ABI data. MODIS may be used later (beyond the 100% ATBD timeframe).

The development strategy is based on setting up and evaluating outputs of the two end-to-end systems, including near-real time acquisition of AVHRR Level 1b, and 15(30)-minute FD SEVIRI Level 1 data and processing them into Level 2 SST and associated TOA clear-sky brightness temperatures (BT) products. The continuous inflow for the AVHRR L1b data is available from the STAR Collaborative Environment Data Repository (CEDR), and for SEVIRI FD images has been established in close collaboration with the AWG Land Team. McIDAS area files are being downloaded from NOAA operational servers in near-real time, reformatted into HDF4.2 files (similar in structure to the EUMETSAT L1.5 product), and saved on STAR SAN storage provided by the AWG for shared use between different teams within the AWG. Near-real time processing is done on SST Team Linux computers.

As of this writing, only the regression SST algorithm is being used for operational AVHRR data processing with the Advanced Clear-Sky Processor for Oceans (ACSPO). The inversion and hybrid algorithms have been implemented within AVHRR-ACSPO for validation purposes. Since validation of SST algorithms for MSG SEVIRI has shown that the performance of the hybrid algorithm is better than the performance of the inversion algorithm, the emphasis with AVHRR has been put on comparison of conventional regression and hybrid algorithms. The results of this comparison are presented in Section 5.4.

## 4.2 Quality Control and Monitoring of *in situ* SST for Satellite Applications

*In situ* sea surface temperatures (SST) are used for calibration and validation (Cal/Val) of satellite retrievals. Quality of *in situ* SSTs is suboptimal and very non-uniform in space and time. The algorithm for QC of *in situ* SST has been developed and implemented. In addition to basic screenings (duplicate removal, plausibility, platform track and SST spike checks), the algorithm also includes two advanced checks for consistency with the external reference field, and cross-platform consistency, based on Bayesian theory. The efficacy of the QC algorithm was tested by adding simulated errors and climate signals on the top of "error-free" (QCed) *in situ* data, and estimating whether the QC algorithm can capture errors and preserve the climate signals. An online *in situ* quality monitor (*iQuam*; www.star.nesdis.noaa.gov/sod/sst/iquam/ ) was set up to serve the QCed *in situ* SSTs to external users for the use in satellite Cal/Val. The *iQuam* also displays in near real time maps and basic "*in situ* minus reference" SST statistics stratified by four *in situ* platform types (drifters, ships, tropical and coastal moorings). The user also has a choice to monitor individual *in situ* platforms.

## 4.3 Implementation and Validation of SST Algorithms for MSG SEVIRI

In this ATBD, analyses of precision and accuracy of SST products is performed against two reference SSTs, including *in situ* (e.g., Ignatov et al., 2010) and global reference SSTs (Dash et al., 2008). The satellite SST is a skin product and both reference SSTs are bulk products. Some of the observed differences are due to this disparity.

Coefficients of the regression and hybrid algorithms, derived using one month (January 2009) of SEVIRI - *in situ* match-ups, are listed in Table 4.2. Note that indexation of the coefficients corresponds to the NLSST regression and hybrid equations:

$$T_R = a_0 + a_1 T_{11} + a_2 (T_{FG} - 273.15) (T_{11} - T_{12}) + a_3 (T_{11} - T_{12})(\sec\theta - 1), \quad (4.1)$$

$$T_H = b_0 + b_1( T_{11} - T_{CS11}) + b_2 (T_{FG} - 273.15)((T_{11} - T_{CS11}) - ( T_{12} - T_{CS12})) + + b_3 ((T_{11} - T_{CS11}) - ( T_{12} - T_{CS12})) (\sec\theta - 1). \quad (4.2)$$

***Table 4.2*** *NLSST regression and hybrid coefficients for MSG SEVIRI*

| **Algorithm** | **$a_0$, $b_0$** | **$a_1$, $b_1$** | **$a_2$, $b_2$** | **$a_3$, $b_3$** |
|---|---|---|---|---|
| Regression (a) | 11.8430 | 0.963999 | 0.0711657 | 0.820187 |
| Hybrid (b) | 0.743279 | 1.07488 | 0.0589083 | 0.734534 |

According to the theory of OE (e.g., Rodgers, 1976), optimal weights of observations and *a priori* information in (4.20) are determined by the noise covariance matrix $\Delta$ and by the covariance matrix of a priori estimates of unknown variables S. In the initial implementation of the Inversion algorithm for SEVIRI, the covariance matrix $\Delta$ of measurement errors and in the SEVIRI channels 9 and 10 was assumed to be diagonal, with both diagonal elements being equal to 0.04 $K^2$, which corresponds to uncorrelated noise with RMS level of 0.2K. The covariance matrix S of *a priori* parameter variations was also assumed diagonal, and *a priori* SST RMS error was set to 0.5K which corresponds to the mean RMS accuracy of the Reynolds Weekly OISST (e.g., Reynolds et al., 2002); RMS error in the optical depth scaling factor was set to 0.2. However, as described in the 80% GOES-R ATBD, the inversion SST estimate, produced with these parameters, has turned out to be biased to the first guess (Reynolds) and therefore underestimates real spatial and temporal SST variations, including global diurnal cycle. This result is consistent with Merchant et al., 2009. In order to make inversion SST variations consistent with ones for regression and hybrid SST, the assumed RMS error for *a priori* SST has been increased to 1.5K.

An example of three SST products derived from one sample FD image on June 2, 2008 is shown in Fig. 4.1 (left panels). The three products look very similar, largely due to the large SST variations from the polar areas to equator of ~30°C. To further emphasize the similarities and differences between the three products, the same images are shown in right panels of Fig. 4.1 after subtracting the global Weekly Reynolds OISST (Reynolds et al., 1994) available for that day. Out of the three algorithms, the regression SST shows maximum variability; in particular, it is more sensitive to ambient cloud and less stable at slant geometries (e.g., note a warm bias in the Western Atlantic, and a cold bias in the Indian Ocean). hybrid SST anomaly shows more uniform and smooth distributions. The empirically adjusted inversion SST has become closer to the hybrid SST.

| | SST | SST Anomaly |
|---|---|---|
| **Regression** | 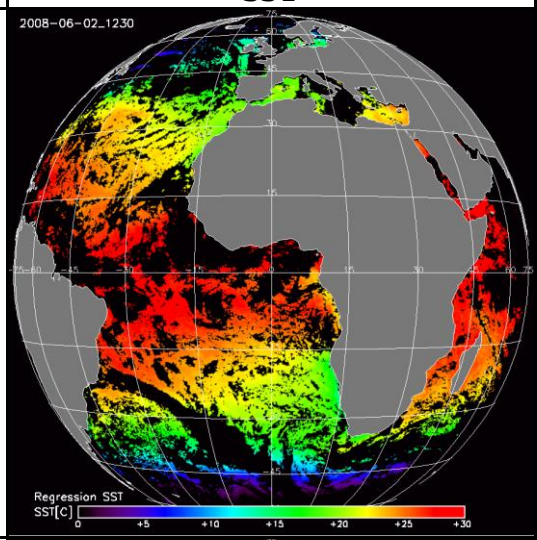 | 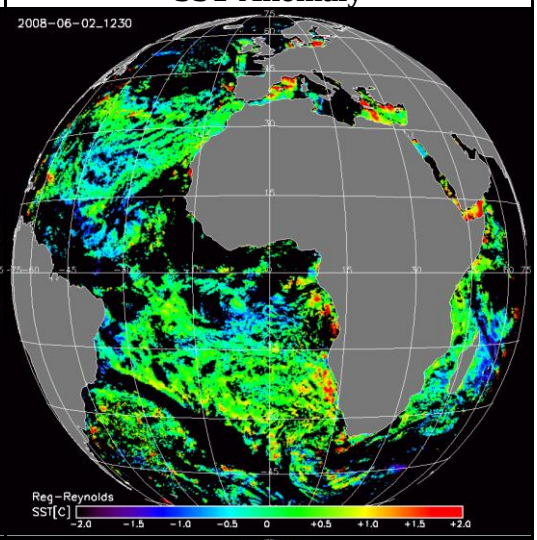 |
| **Hybrid** | 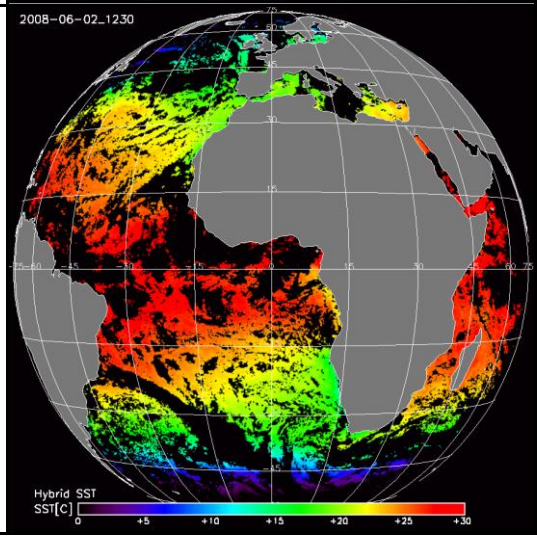 | 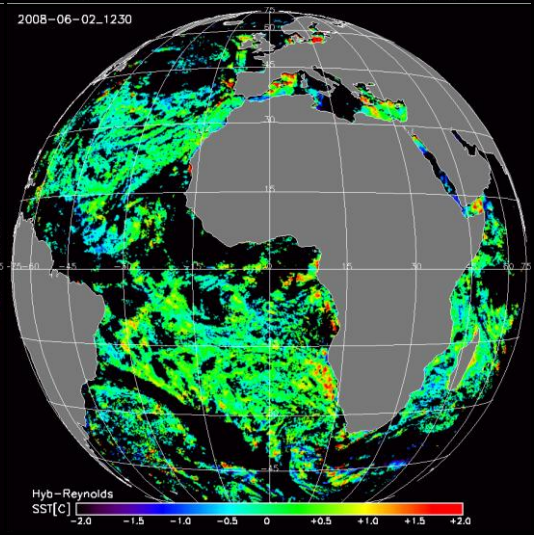 |

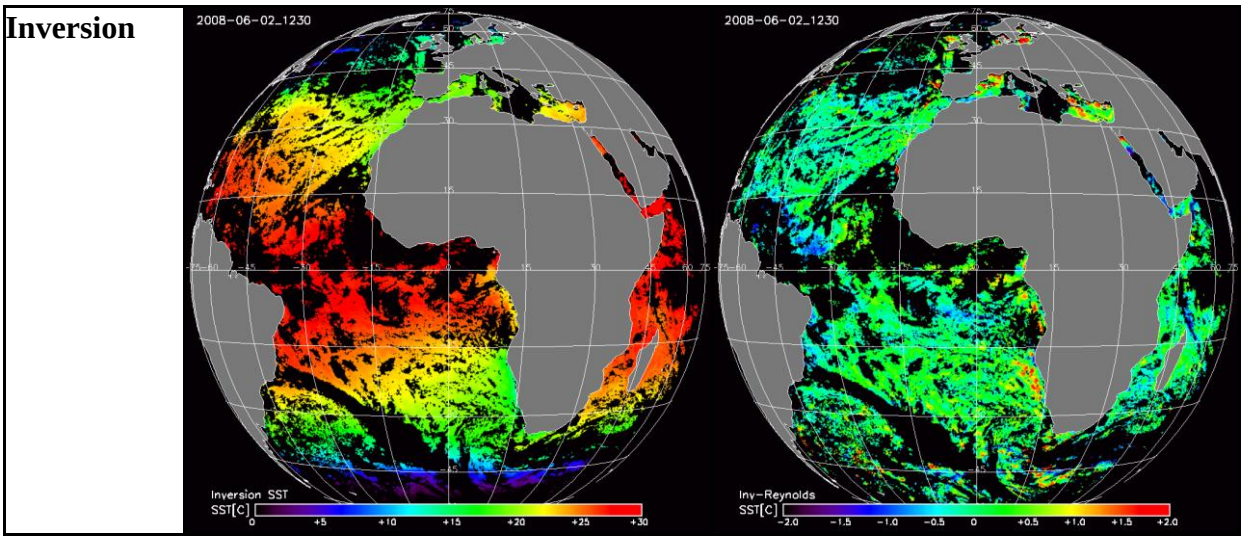


***Figure 4.1*** *SST (left) and SST anomalies, retrieved SST minus Reynolds SST (right) on 2 June 2008 @ 12:30 UTM. Note a cold bias in regression SST at slant views, e.g., in the Indian Ocean.*

For quantitative comparisons, histograms of "retrieved minus Reynolds" SSTs are shown in Fig.4.2 for two days of data, one in June 2008 and one in January 2009. Although using Reynolds SST as "ground truth" may not be appropriate for ultimate evaluation of product precision, this approach can be used to evaluate the relative performance of the three products. The regression SST shows the greatest STD due to the contribution of variable local SST bias, as shown in Section 4.2.1. The inversion SST shows the smallest STD. This, however, cannot be considered as the advantage of the inversion algorithm because the weights of *a priori* information in (4.20) were set without full justification, and therefore there is no guarantee that this algorithm does adequately reproduce SST variations in space and time. The value of STD for the hybrid SST is in between ones for regression and inversion. As described in Section 4.2.3, the hybrid SST estimate has been set up to be free from local SST biases, and its variance is adjusted to match the variance of the information component of regression SST.

Figure 4.3 shows sample diurnal cycles of the bias and STD of regression, hybrid, and inversion SST (as functions of Universal Time Coordinated (UTC), for 10 June 2008 and 4 January 2009. The value of 0.3-0.4 K for a globally average diurnal range is consistent with published data (e.g., Stuart-Menteth et al., 2005; Kennedy et al., 2002; Gentemann and Minnett, 2008). All three products show diurnal cycle in retrieved SST (recall that Reynolds SST, used to normalize all three products, does not resolve the diurnal cycle). The inversion algorithm shows a smaller SST diurnal range than ones measured by the regression and hybrid algorithms. To put SEVIRI observation in context, Fig.4.4 shows an expected shape of the diurnal cycle (as a function of local time). The proximity of their shapes suggests that SEVIRI and ABI can potentially derive information about SST diurnal cycle. The relative precision of the SST products measured by their respective STDs is stable during the course of the day.

Figure 4.5 shows time series of global bias and STD with respect to Reynolds SST in the three SEVIRI SST products for June 2008 and January 2009. All three SST products are approximately centered at Reynolds SST and show diurnal cycle (recall that Reynolds SST does not resolve a diurnal cycle). STD of the hybrid algorithm lies in between regression and inversion. Except diurnal variations, the STD of SST in all three products show long-term

variations likely caused by variable accuracy of the Reynolds OISST field. As an example, Fig. 4.6 shows the FD SST, determined with regression and hybrid algorithms from the SEVIRI image on June 21 2008, 14:00 UTC. All images show strong warm SST anomalies in the North Atlantic and in the Mediterranean Sea, which are not captured by the Reynolds OISST. These anomalies cause the increase in global SST STD, clearly seen in the end of June 2008 on the left bottom panel in Fig. 4.5. Figure 4.7 shows time series of bias and STD of retrieved SST - *in situ* SSTs for the same months (June 2008 and January 2009). The STDs of retrieved SST with respect to *in situ* SST are smaller than with respect to Reynolds OISST for all three algorithms.

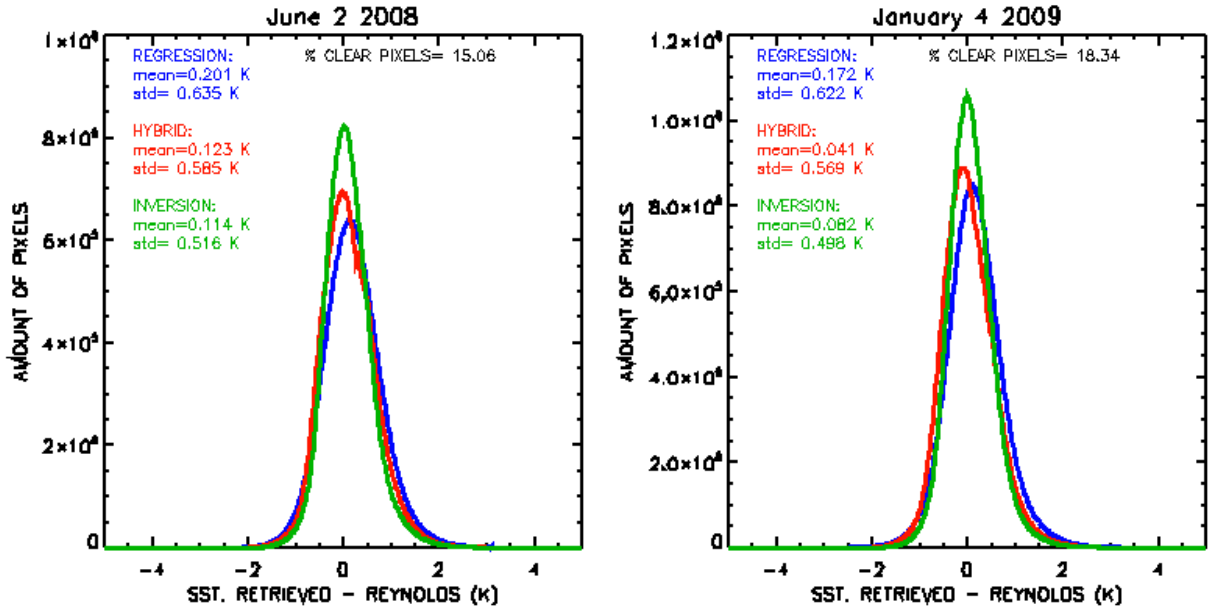


***Figure 4.****2 Histograms of SST anomalies from two sample days of SEVIRI data.*

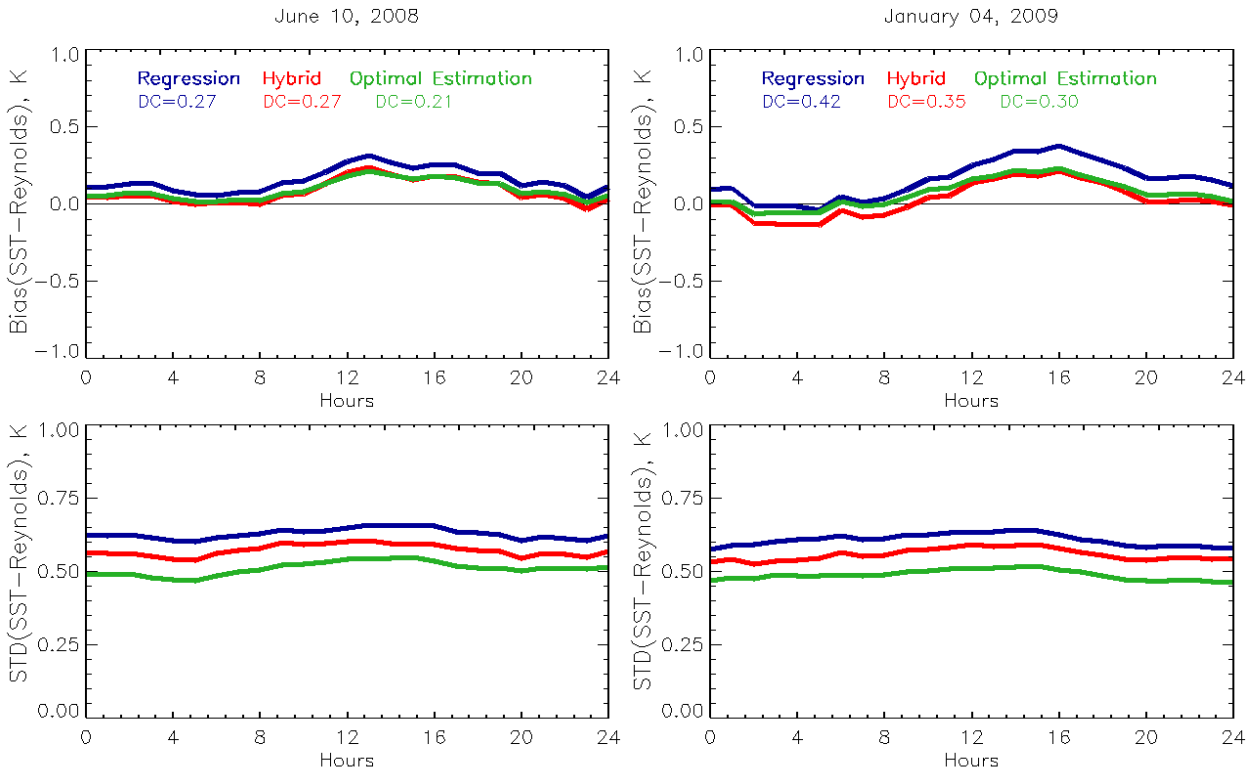


***Figure 4.3*** *Time series of SST biases and STDs for June 10, 2008 (left) and January 04, 2009 (right). Each data point represents corresponding statistics derived from all clear-sky pixels within one FD image.*

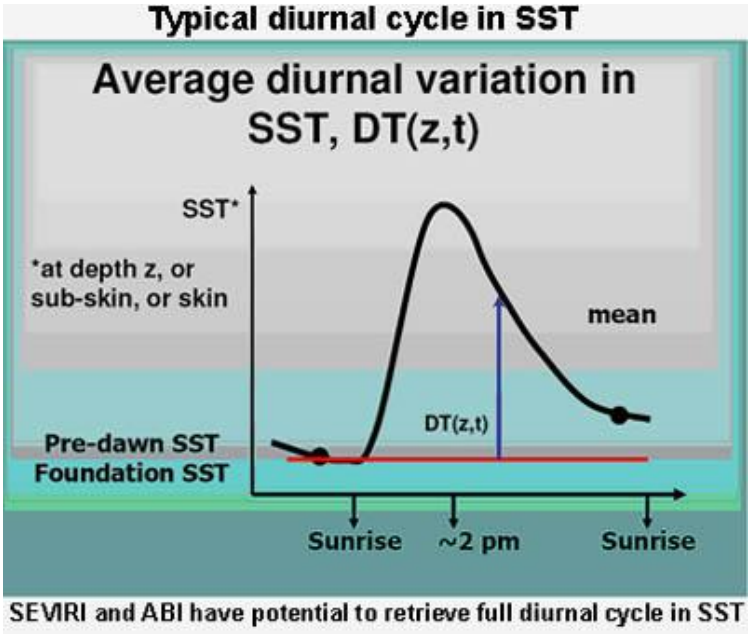


***Figure 4.4*** *Expected diurnal cycle in SST (courtesy of* www.ghrsst-pp.org/*).*

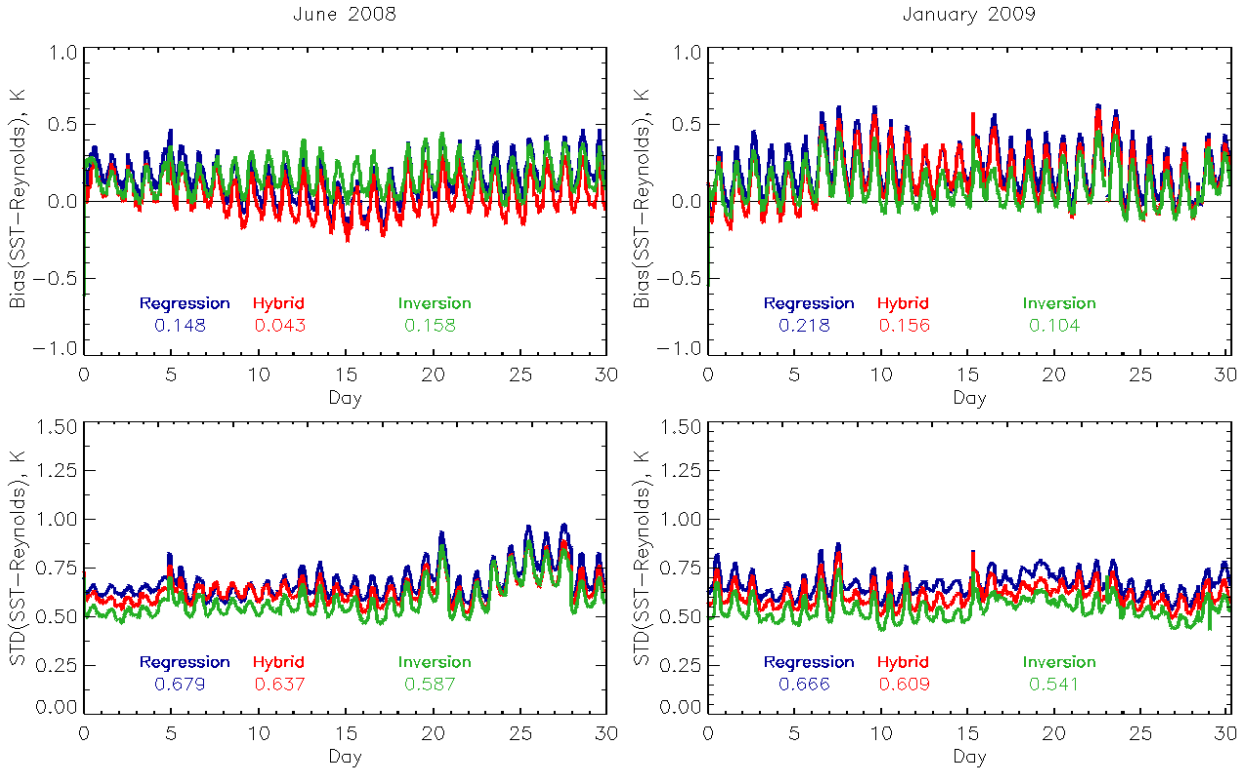


***Figure 4.5*** *Time series of global bias and STD of retrieved SST minus Reynolds SST in three SEVIRI SST products in June 2008 (left) and January 2009 (right). The numbers on each panel characterize average values of bias or STD over the month.*

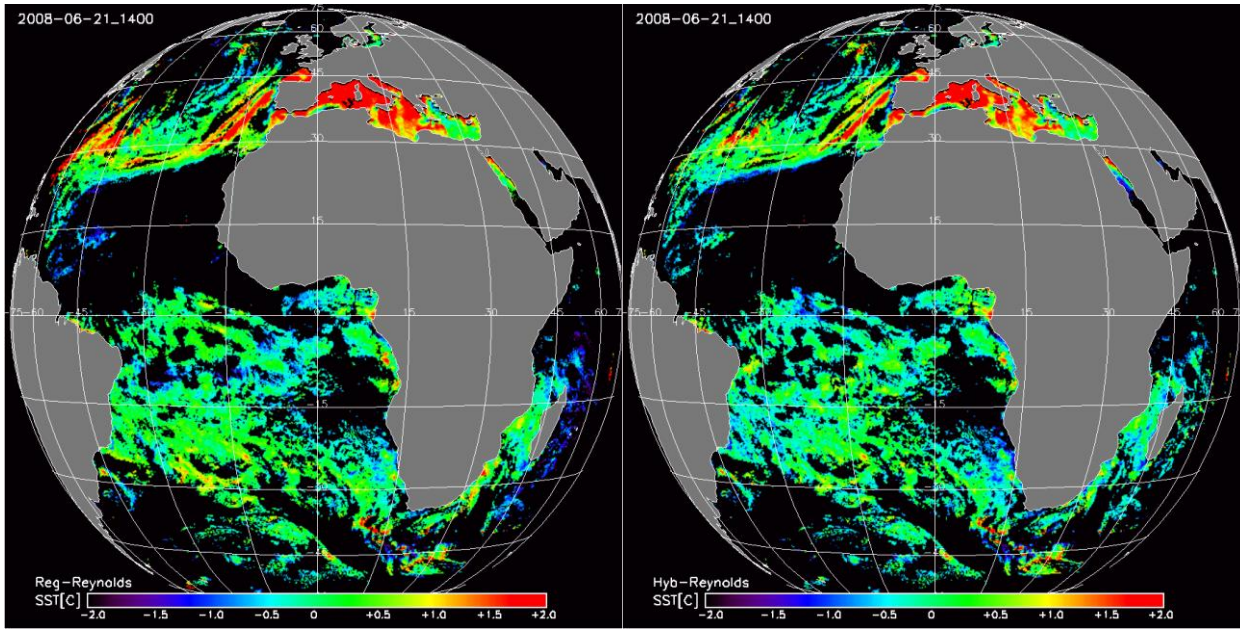


***Figure 4.6*** *FD distributions of regression and hybrid SST anomalies on June 21 2008, 14:00 UTC.*

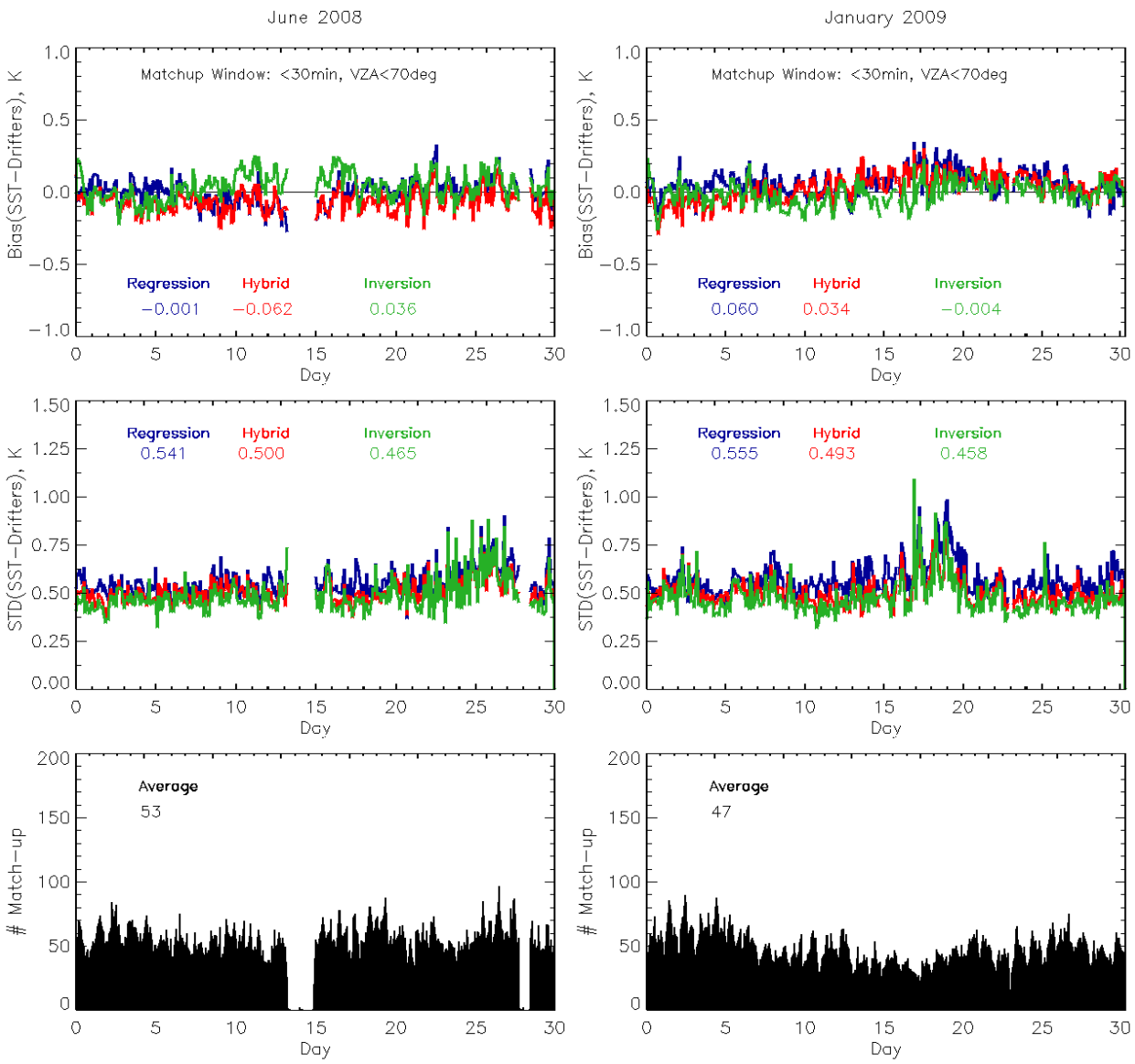


***Figure 4.7*** *Time series of global bias and STD with respect to in situ SST in the three SEVIRI SST products in June 2008 and January 2009. Match-up window was set to 5km in space and 30 min in time. 50 match-ups per FD in June 2008 and 40 in Jan 2009 per FD; global mean bias is 0± 0.5K. Diurnal cycle is caused by skin (SEVIRI) – bulk (in situ) differences; for all 3 algorithms, global STD 0.6±0.2K. Hybrid STD is in between STDs for regression and inversion SST.*

## 4.4 Validation of Regression SST Algorithm for AVHRR

Additional evaluation of the regression algorithm was performed using the heritage AVHRR SST product. Figure 4.8 illustrates the principles of how the match-up data set with *in situ* data is created. In the AVHRR processing, the match-up window was set up to 1 hr in time and 20 km in space. Analyses are currently underway to optimize the match-up windows (Minnett, 1990; Ignatov et al., 2009) and quality control procedures (Emery et al, 1991; Xu and Ignatov, 2009).

Next, validation statistics (satellite minus *in-situ* SST) are generated on a monthly basis, separately by day and night. Figure 4.9 gives examples of monthly validation statistics for one NOAA platform. Time series of the mean and STD are shown in Fig. 4.10. Typically, there are ~7,000 match-ups per month for day and ~15,000 match-ups for night in the case of AVHRR.

Parameters of the Gaussian distribution are subsequently monitored in time (Fig. 4.10). Typically, bias is within ~±0.1K and STD is within 0.5K. Note that these validation statistics are only achieved if outliers are removed from *in-situ* data. Figure 4.10 compares side-by-side bias and STD for the case if outliers were removed (left column) and retained (right column) in the *in situ* data. Satellite data also have outliers, but their magnitude and their fraction are much smaller. Recall that *in-situ* SST data come from many different sources (countries, agencies) and their quality is non-uniform in space and time and often suboptimal. Careful quality control of *in situ* SST is needed before they can be used in satellite Cal/Val (Emery et al, 2001; Xu and Ignatov, 2009).

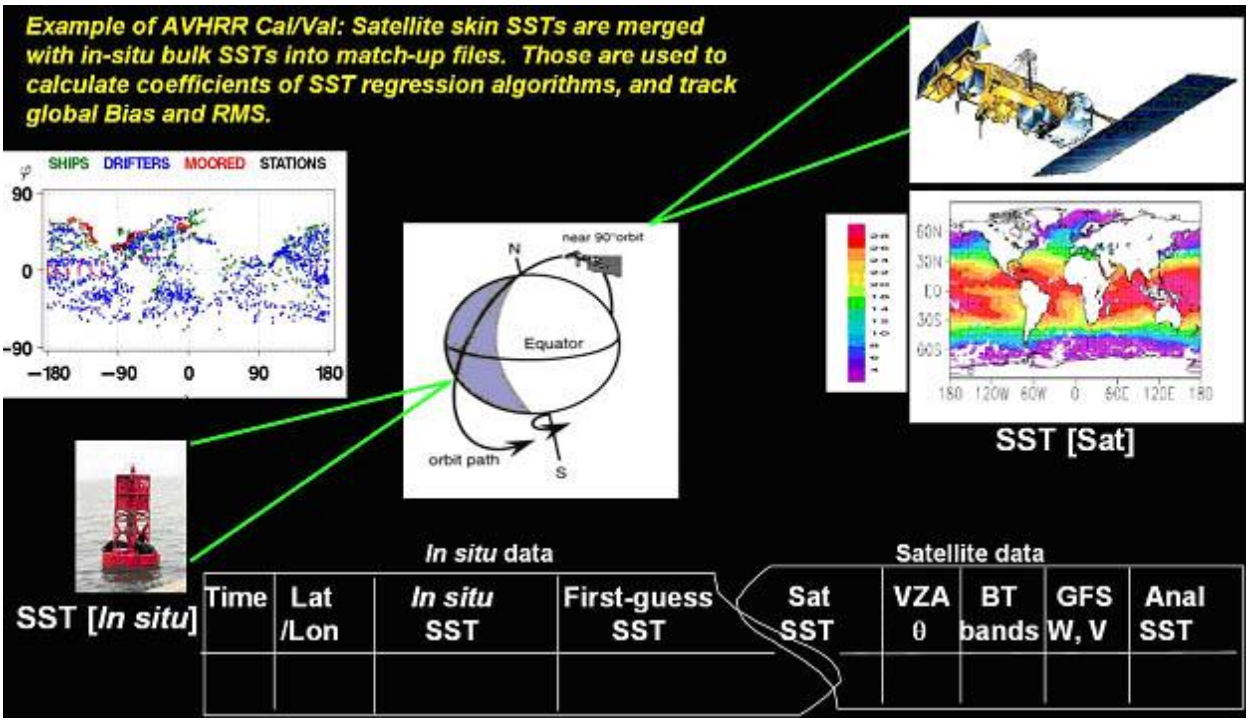


***Figure 4.8*** *Match-up methodology with global in-situ data.*

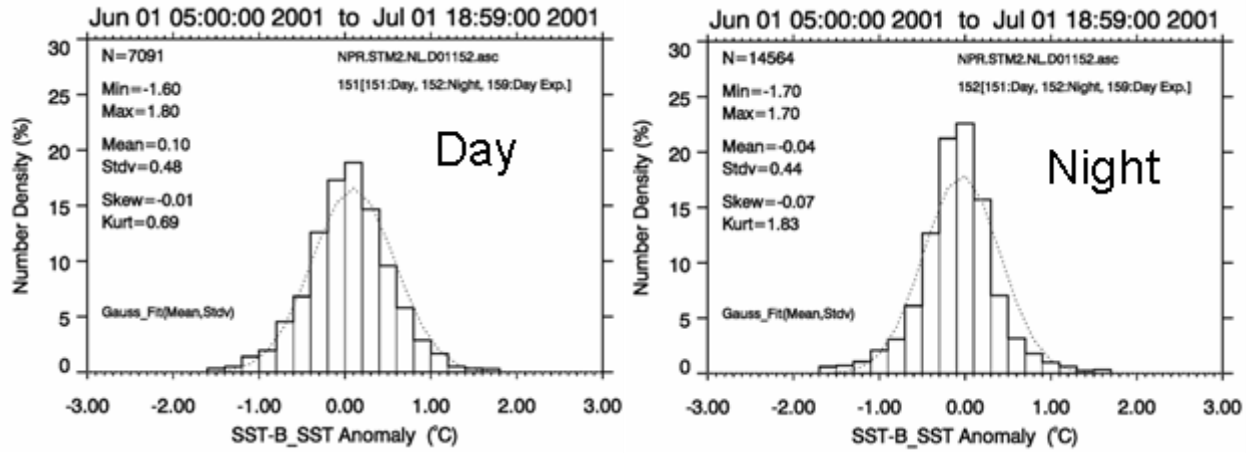


***Figure 4.9*** *Sample monthly validation statistics for NOAA-16 in June 2001. Statistics are generated on a monthly basis and stratified by Day and Night. Typically for AVHRR, number of match-ups is 10,000 per month. Global Bias (accuracy) is ~0.1K and Global RMSD (Precision) ~0.5K.*

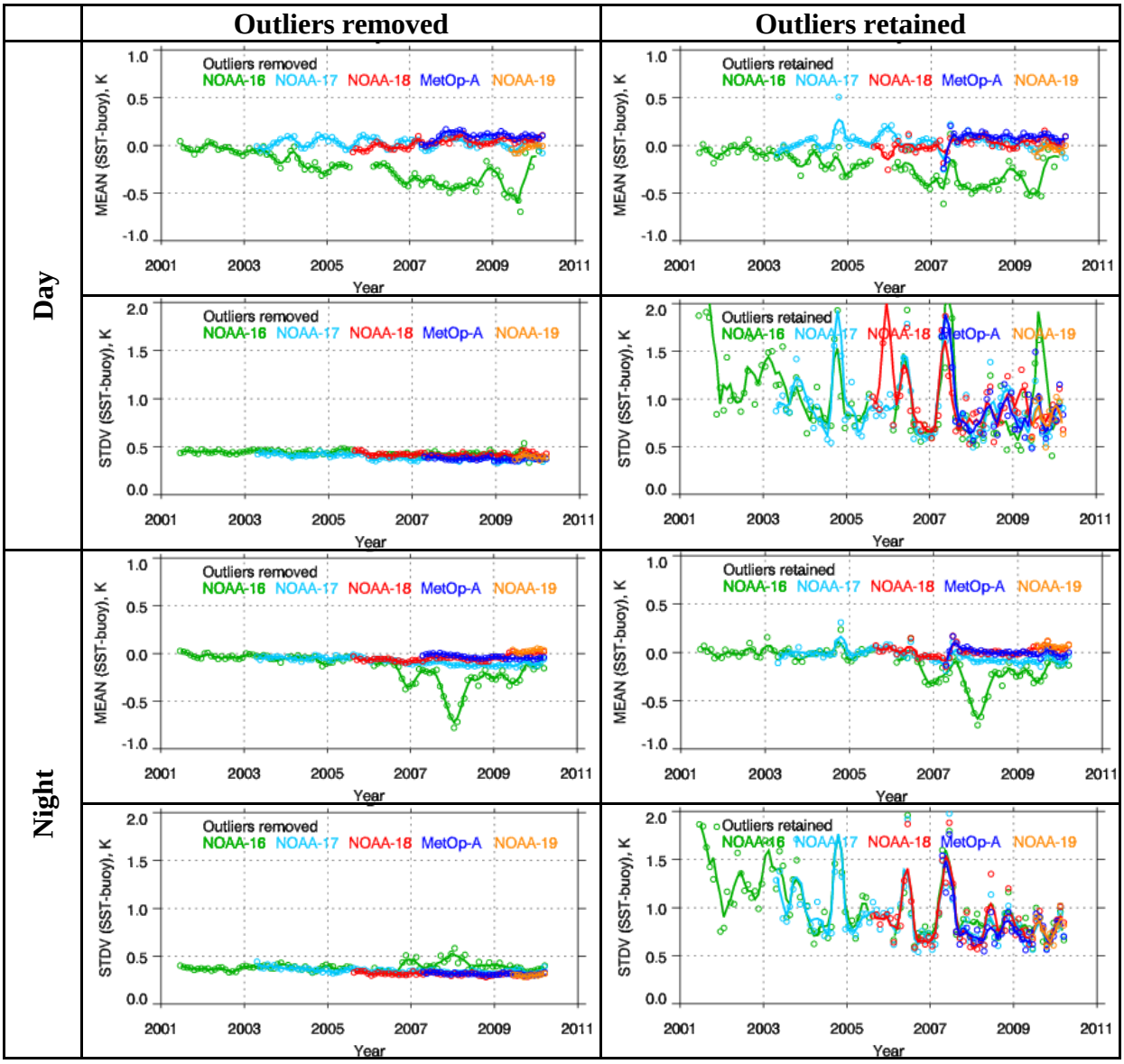


***Figure 4.10*** *Time series of validation accuracy (global bias) and precision (global STD) for 5 NOAA platforms: NOAA-16, -17, -18, -19, and MetOp-A. Outliers excluded from in situ data (left) and outliers retained (right). Comparison with QC'ed Buoy SST: Bias +/-0.1K; STD 0.4-0.5K. Data are from SQUAM web-based tool, http://www.star.nesdis.noaa.gov/sod/sst/calval/ .*

## 4.5 Comparison of Regression and Hybrid NLSST Algorithms for AVHRR

Two AVHRR and matchup data sets were used in the comparison of regression and hybrid SST algorithms. The first data set contained nighttime observations from five AVHRR-carrying platforms, NOAA 16, 17, 18, 19 and Metop-A and matchups of drifting buoy *in situ* measurements within the time period August 18 - September 17 2009 (2009 data set). Daytime observations were not used to avoid distortions of angular dependencies by sun glint and non-uniform heating of the ocean surface along the AVHRR scan. Another reason to ignore daytime observations is that the difference between skin SST, which the AVHRR observations are sensitive to, and *in situ* measured bulk SST is largest in the daytime. The majority of the analysis, including estimation of local BT biases, calculation of regression and hybrid coefficients, and evaluation of accuracy and precision of SST retrievals was performed with this data set. The second, 2010 data set, contained nighttime data from the same platforms and drifting buoy matchups for January 1-7 2010 and was used to ensure stability of the results obtained with the 2009 data set. Here we present the comparative performance of regression and hybrid SST algorithms in the NLSST formulation only. The analysis of nighttime AVHRR MCSST retrievals has shown that adding the more transparent channel 3.7μm (Ch3b) to the split-window channels 11 μm (Ch4) and 12 μm (Ch5) improves the regression, hybrid, and inversion SST estimates and minimizes the differences between them. These results are consistent with Merchant et al. (2008).

For AVHRR, correction of Ch4 and Ch5 local biases as two-dimensional functions of $|\theta|$ and total precipitable water content in the atmosphere was implemented. Because of essential nonlinearities of the dependencies of $\Delta T_B$ biases from $\theta$ and $W$, these functions were represented with two-dimensional lookup tables (LUT). The biases were estimated by averaging over "clear" pixels during nighttime AVHRR observations from August 18 to September 17, 2009 within $4^o \times 0.5$ g/cm$^2$ cells in the ($\theta$, $W$) space. The exact value of bias for any combination of $\theta$ and $W$ was found by bilinear interpolation between the nearest LUT nodes.

The regression and hybrid coefficients, calculated from the 2009 data set for five AVHRR-carrying platforms are presented in Table 4.3. Table 4.4 compares the precisions of fitting *in situ* SST $T_{IS}$ with regression SST $T_R$ and hybrid SST $T_H$ within the 2009 data set (the biases of $T_R$ - $T_{IS}$ and $T_H$ - $T_{IS}$ are not shown in the Table 4.4 because they are zero by construction). For all platforms, STDs of $T_H$ - $T_{IS}$ are smaller than STDs of $T_R$ - $T_{IS}$ and correlations between $T_H$ and $T_{IS}$ are higher than between $T_R$ and $T_{IS}$. Table 4.4 also shows correlation between retrieved SST increments, $\Delta T_H = T_H - T_{FG}$ and $\Delta T_R = T_R - T_{FG}$, and *in situ* SST increments $\Delta T_{IS} = T_{IS} - T_{FG}$. The incremental correlations are also higher for $\Delta T_H$ than for $\Delta T_R$.

***Table 4.3*** *Regression and hybrid regression coefficients for five AVHRR carrying platforms.*

| Coefficient | Metop-A | NOAA-16 | NOAA-17 | NOAA-18 | NOAA-19 |
|---|---|---|---|---|---|
| **Regression** | | | | | |
| $a_0$ | 11.8215 | 19.2345 | 16.9407 | 16.1066 | 18.0330 |
| $a_1$ | 0.963037 | 0.935558 | 0.944471 | 0.947016 | 0.940330 |
| $a_2$ | 0.0731346 | 0.0720969 | 0.0735208 | 0.0708459 | 0.0628712 |
| $a_3$ | 1.14645 | 0.837695 | 1.06111 | 0.878284 | 0.783647 |
| **Hybrid** | | | | | |
| $b_0$ | -0.0286684 | -0.0398945 | -0.0561765 | -0.0157083 | -0.0372663 |
| $b_1$ | 0.985580 | 0.949439 | 0.949757 | 0.924738 | 0.917020 |
| $b_2$ | 0.1032640 | 0.0848259 | 0.0984409 | 0.0925503 | 0.0884904 |
| $b_3$ | -0.717516 | -0.0398945 | -0.103969 | -0.166228 | -0.401969 |

***Table 4.4*** *Statistics of deviations of regression SST $T_R$ and hybrid SST $T_H$ from in situ SST $T_{IS}$. 2009 data set.*

| Parameter | MetOp-A | NOAA-16 | NOAA-17 | NOAA-18 | NOAA-19 |
|---|---|---|---|---|---|
| *STD*, $T_R - T_{IS}$ | 0.531 | 0.486 | 0.527 | 0.528 | 0.559 |
| STD, $T_H - T_{IS}$ | 0.475 | 0.451 | 0.475 | 0.461 | 0.493 |
| Correlation, $\Delta T_R$ and $\Delta T_{IS}$ | 0.312 | 0.313 | 0.309 | 0.284 | 0.239 |
| Correlation, $\Delta T_H$ and $\Delta T_{IS}$ | 0.344 | 0.345 | 0.328 | 0.335 | 0.303 |

***Table 4.5*** *Statistics of regression and hybrid SST increments over the 2010 matchup data set.*

| Statistics | Metop-A | NOAA 16 | NOAA 17 | NOAA 18 | NOAA 19 |
|---|---|---|---|---|---|
| Bias, $T_R - T_{IS}$ | -0.051 | 0.065 | -0.103 | 0.049 | 0.095 |
| Bias, $T_H - T_{IS}$ | 0.035 | -0.018 | -0.022 | 0.095 | 0.104 |
| *STD*, $T_R - T_{IS}$ | 0.565 | 0.528 | 0.515 | 0.536 | 0.540 |
| STD, $T_H - T_{IS}$ | 0.465 | 0.449 | 0.418 | 0.414 | 0.404 |
| Correlation, $\Delta T_R$ and $\Delta T_{IS}$ | 0.236 | 0.270 | 0.284 | 0.238 | 0.220 |
| Correlation, $\Delta T_H$ and $\Delta T_{IS}$ | 0.324 | 0.377 | 0.404 | 0.399 | 0.397 |
| Correlation, $T_R$ and $\Delta T_{IS}$ | 0.994 | 0.996 | 0.995 | 0.995 | 0.999 |
| Correlation, $\Delta T_H$ and $\Delta T_{IS}$ | 0.997 | 0.998 | 0.996 | 0.998 | 1.000 |

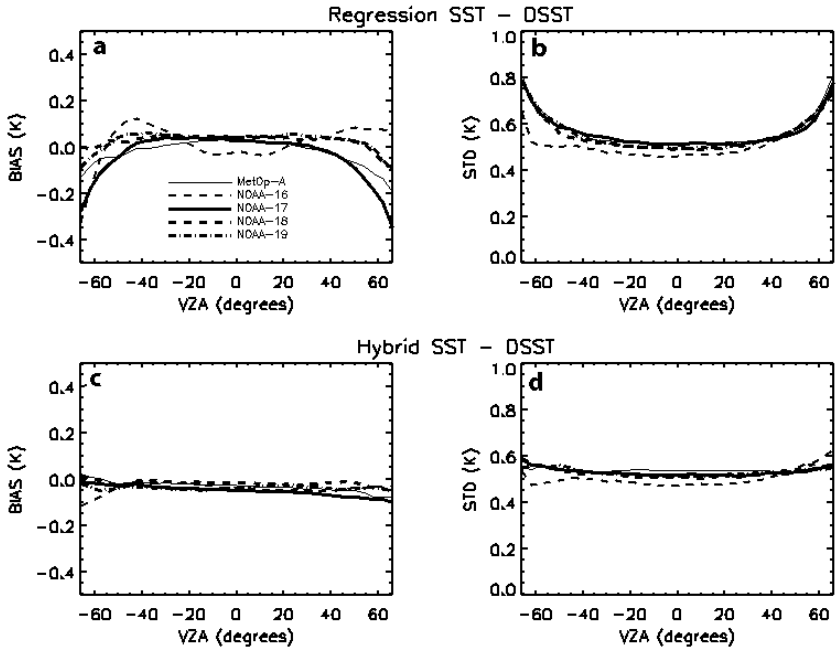


***Figure 4.11*** *Statistics of retrieved SST increments as functions of local zenith angle (LZA): Bias (a) and STD (b) of regression SST increment $\Delta T_R = T_R - T_0$; bias (c) and STD (d) of hybrid SST increment $\Delta T_H = T_H - T_0$. The statistics accumulated over 2009 data set.*

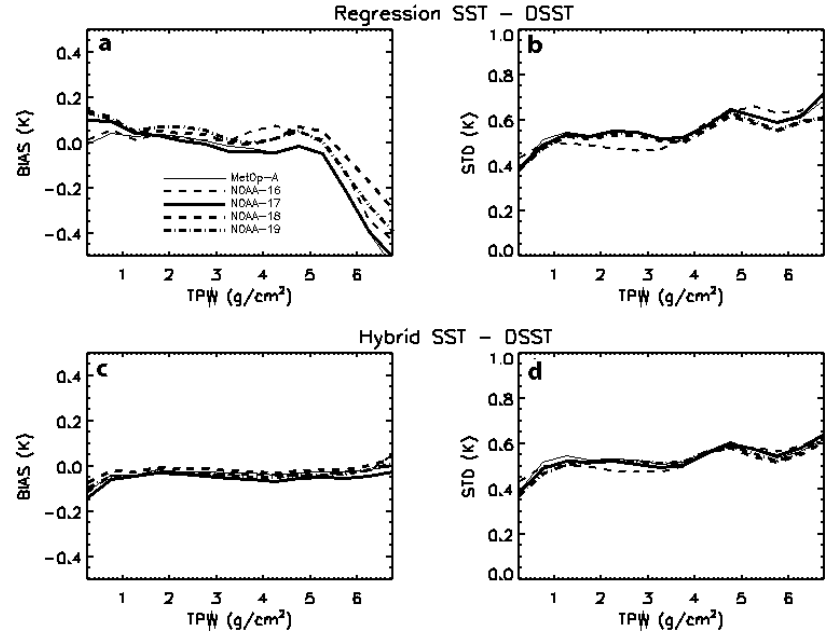


***Figure 4.12*** *Statistics of retrieved SST increments as functions of GFS total precipitable water vapor content (TPW): Bias (a) and STD (b) of regression SST increment $\Delta T_R = T_R - T_0$; bias (c) and STD (d) of hybrid SST increment $\Delta T_H = T_H - T_0$. The statistics accumulated over 2009 data set.*

Figure 4.11 compares the dependencies of local biases and STD of $\Delta T_R$ and $\Delta T_H$ on local zenith angle. Inaccuracy of approximation of the inverse relationship between SST and BTs with NLSST conventional regression equation at big local zenith angles causes increase of both bias and STD of $\Delta T_R$. The same dependencies for bias and STD of $\Delta T_H$ are flattened. Figure 4.12 compares these statistics as functions of GFS total precipitable water content in the atmosphere (TPW). The dependency of $\Delta T_R$ bias on TPW in Fig. 4.12a is more pronounced than the same dependency for $\Delta T_H$ bias in Fig. 4.12c.

Table 4.5 compares the accuracies and the precisions of fitting *in situ* SST $T_{IS}$ with regression SST $T_R$ and hybrid SST $T_H$ within the 2010 data set. For all platforms, both for Regression and Hybrid algorithms, the absolute values of biases of $T_H$ - $T_{IS}$ are within or close to 0.1K, which indicates that there were no significant calibration trends between August –September 2009 and January 2010. STDs of $T_H$ - $T_{IS}$ are smaller than STDs of $T_R$ - $T_{IS}$ and correlations between $\Delta T_H$ and $\Delta T_{IS}$ are higher than between $\Delta T_R$ - $\Delta T_{IS}$. Table 4.5 also shows correlations between absolute temperatures $T_R$ vs. $T_{IS}$ and $T_H$ vs. $T_{IS}$. These correlations are also higher for $T_H$ than for $T_R$. Overall, the Hybrid algorithm improves SST retrieval accuracy over the conventional Regression algorithm. The improvement shows itself in more accurate fitting with *in situ* SST measurements, significant reduction in local SST biases with respect to the reference SST field, more uniform dependencies of SST retrieval error on local zenith angle and in better temporal stability of global SST biases.

## 4.6 Stability of the Hybrid SST Estimates wrt the First Guess SST

At present, several SST analysis fields are available, such as Reynolds Daily High-Resolution Blended SST (DSST - Reynolds et al., 2007), Weekly Optimal interpolation SST (WSST - Reynolds et al., 2002), Operational Sea Surface Temperature and Sea Ice Analysis (OSTIA - Stark et al., 2007, 2008) and Pathfinder SST (www.nodc.noaa.gov/sog/pathfinder4km/userguide.html). A possible scenario in operational ose of the hybrid SST algorithm is one in which the analysis field initially used for calculation of hybrid coefficients becomes unavailable. Since different SST analysis fields are not identical, it is important that switching from one SST analysis to another would not degrade the SST retrieval accuracy nor require recalculation of hybrid regression coefficients.

The following equation represents incremental formulations of NLSST algorithm:

$$T_H = T_{FG} + b_0 + b_1 [T_{11} - T_{CS11}(T_{FG}, \mathbf{x}, \theta)] + \\ + b_2 Q\{[T_{11} - - T_{CS11}(T_{FG}, \mathbf{x}, \theta)] - [T_{12} - T_{CS12}(T_{FG}, \mathbf{x}, \theta)]\} + \\ + b_3 \{[T_{11} - - T_{CS11}(T_{FG}, \mathbf{x}, \theta)] - [T_{12} - T_{CS12}(T_{FG}, \mathbf{x}, \theta)]\} (\sec\theta - 1) \quad (4.3)$$

Here, $T_{FG}$ is the first guess SST, and simulated clear-sky BTs $T_{CS11}$, $T_{CS12}$ at 11 and 12 μm are the functions of $T_{FG}$, $\theta$ and the vector of GFS atmospheric variables **x**. $Q$ in (4.3) is the "atmospheric term," which accounts for global variations in the atmospheric absorption. The conventional NLSST formulation, which is considered in this ATBD, assumes that water vapor absorption in the atmosphere is roughly proportional to SST in Celsius, and

$$Q = T_{FG} - 273.15, \quad (4.4)$$

Since the estimate of atmospheric water vapor content $W$ is currently available from GFS data, we are planning to replace $Q$ with the term depending directly on $W$ rather than on $T_{FG}$. After this replacement, the dependency of $T_H$ from $T_{FG}$ will manifestate itself only through variations in $T_{FG}$, $T_{CS11}$ and $T_{CS12}$. In this Section, we analyze sensitivity of $T_H$ to variations in $T_{FG}$, $T_{CS11}$ and $T_{CS12}$ assuming that $Q$ does not depend on $T_{FG}$.

We generated the NLSST Hybrid SST estimates from Metop-A observations for the 2010 data set using several analysis fields as the first guess: Daily Reynolds SST (DSST, $T_{DSST}$), Weekly Reynolds SST (WSST, $T_{WSST}$), OSTIA ($T_{OSTIA}$) and Pathfinder ($T_{PATHF}$):

$$T_H(T_{FG})=T_{FG} + b_0 + \mathbf{b}\Delta\mathbf{Y}[T_{CS11}(T_{FG}, \mathbf{x}, \theta), T_{CS12}(T_{FG}, \mathbf{x}, \theta), T_{FG}, \theta, Q], \quad (4.5)$$

The vector of regressors' increments $\Delta\mathbf{Y}$ is defined in (4.12), and $T_{FG}$ can be equal to $T_{DSST}$, $T_{WSST}$, $T_{OSTIA}$ or $T_{PATHF}$. In all cases, $Q$ was calculated as $Q = T_{DSST} - 273.15$. As DSST is the SST field that is used as a reference field in ACSPO for AVHRR, the clear-sky BTs, $T_{CS11}(T_{DSST}, \mathbf{x}, \theta)$, and $T_{CS12}(T_{DSST}, \mathbf{x}, \theta)$ were simulated directly with CRTM. Along with $T_{CS11}$ and $T_{CS12}$, their derivatives with respect to $T_{FG}$ $D_{11}(T_{DSST})$ and $D_{12}(T_{DSST})$, were calculated numerically. For other reference fields $T_{FG}$, $T_{CS11}$ and $T_{CS12}$ were calculated using the Taylor expansion as follows:

$$T_{CS11}(T_{FG}, \mathbf{x}, \theta) = T_{CS11}(T_{DSST}, \mathbf{x}, \theta) + D_{11}(T_{DSST})\,(T_{FG} - T_{DSST}), \quad (4.6a)$$

$$T_{CS12}(T_{FG}, \mathbf{x}, \theta) = T_{CS12}(T_{DSST}, \mathbf{x}, \theta) + D_{12}(T_{DSST})\,(T_{FG} - T_{DSST}), \quad (4.6b)$$

In (3.14), $T_{FG}$ is equal to $T_{WSST}$, $T_{OSTIA}$ or $T_{PATHF}$. Table 4.6 compares global statistics of hybrid SST, produced with different first guess SST fields. Global bias and STD of $T_{FG}$ - $T_{DSST}$ characterize the initial differences between a given field and DSST. The values of biases and STDs of $T_{FG}$ - $T_{DSST}$ vary respectively from -0.09 and 0.051 for WSST to -0.475 and 0.954 for Pathfinder. Biases and STDs of $T_H(T_{FG})$ - $T_{DSST}$ characterize the statistics of deviations of $T_H(T_{FG})$ from $T_{DSST}$. If these statistics are averaged over the whole scan ($-68^o < \theta < +68^o$), the biases of $T_H(T_{FG})$ - $T_{DSST}$ with different $T_{FG}$ vary from 0.047K to 0.056K, i.e., within 0.01K, and STDs vary from 0.462 K to 0.505K. The STDs are noticeably reduced in the central part of the scan ($-40^o < \theta < +40^o$). The Table also shows the statistics of global differences between $T_H$, produced with the first guess $T_{FG}$, and $T_H$, produced with the first guess DSST. The biases of $T_H(T_{FG})$ - $T_H(T_{DSST})$ are well within 0.01K for all $T_{FG}$, which means that $T_H(T_{FG})$, produced with different $T_{FG}$, are practically unbiased with respect to each other. The STDs of $T_H(T_{FG})$ - $T_H(T_{DSST})$ are within 0.16K over the whole scan and within 0.09 K in the central part of the scan. Therefore, we conclude that the fields of $T_H$, produced with different $T_{FG}$, converge to the same retrieved SST field with a good accuracy. However, the accuracy of convergence degrades toward scan edges.

***Table 4.6*** *Statistics of hybrid SST estimates, produced with different first guess SST fields, averaged over nighttime Metop-A clear-sky pixels within 2010 data set (January 1-7 2010).*

| Statistics | DSST | WSST | OSTIA | Pathfinder |
|---|---|---|---|---|
| $T_{FG}$ - $T_{DSST}$ | | | | |
| Bias, K | 0 | -0.009 | -0.045 | -.475 |
| STD, K | 0 | 0.051 | 0.394 | 0.954 |
| $T_H(T_{FG})$ - $T_{DSST}$, $-68^o < \theta < +68^o$ | | | | |
| Bias, K | 0.035 | 0.056 | 0.056 | 0.047 |
| STD, K | 0.475 | 0.499 | 0.505 | 0.505 |
| $T_H(T_{FG})$ - $T_{DSST}$, $-40^o < \theta < +40^o$ | | | | |
| Bias, K | 0.054 | 0.060 | 0.060 | 0.055 |
| STD, K | 0.459 | 0.475 | 0.480 | 0.478 |
| $T_H(T_{FG})$ - $T_H(T_{DSST})$, $-68^o < \theta < +68^o$ | | | | |
| Bias, K | 0 | 0.003 | 0.003 | -0.006 |
| STD, K | 0 | 0.139 | 0.146 | 0.159 |
| $T_H(T_{FG})$ - $T_H(T_{DSST})$, $-40^o < \theta < +40^o$ | | | | |
| Bias, K | 0 | 0.006 | 0.006 | 0.001 |
| STD, K | 0 | 0.065 | 0.072 | 0.088 |

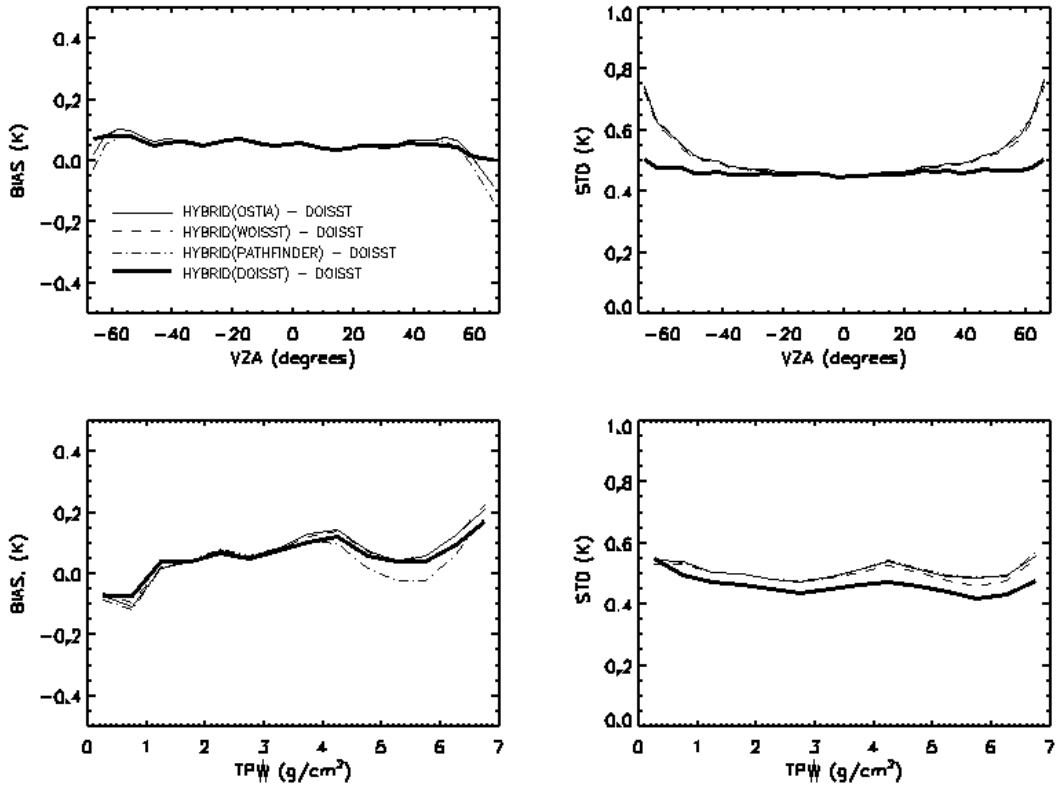


***Figure 4.13*** *The bias and STDs of $T_H(T_{FG})$ - $T_{DSST}$ for different analysis fields as functions of local zenith angle $\theta$ and total precipitable water content (TPW). Metop-A, 2010 data set.*

Figure 4.13 shows the bias and STDs of $T_H(T_{FG})$ - $T_{DSST}$ as functions of local zenith angle $\theta$ and TPW. While for $T_H(T_{DSST})$ - $T_{DSST}$ these functions are only slightly dependent on $\theta$, the dependencies for other analysis fields are more pronounced and similar to each other. The reason for this difference between DSST and other fields is that in the case of DSST, clear-sky BTs are calculated with CRTM, whereas for other analysis fields the Taylor expansions of the CRTM function (5.5) are used. The increase in STD of $T_H(T_{FG})$ - $T_{DSST}$ toward the scan edges for WSST, OSTIA and Pathfinder points to degradation in accuracy of numerically calculated derivatives of $T_{CS11}$ and $T_{CS12}$ with respect to $T_{FG}$. The fact that the accuracy of BT derivatives degrades towards scan edges can serve as an additional argument for using the hybrid SST retrieval rather than the inversion algorithm.

## 4.7 ABI Cloud Mask and SST Quality Control

In GOES-R suite of geophysical products, generic ABI cloud mask (ABI CM) will be evaluated for all sensor pixels and made available to all downstream products. Prior experience with AVHRR and MODIS suggests that a generic CM may not be optimal for all downstream products, and product-specific quality control may still be needed (Martins et al., 2002; Minnett and Evans, 2008; OS&I SAF SST, 2009). The approach adopted in the ABI CM is to provide a somewhat 'liberal' (attempting to minimize false cloudy) cloud screening, leaving product-specific QC up to individual retrieval algorithms (Heidinger, 2009). Following this approach, SST Team has implemented SST quality control (SST QC). The algorithm for SST QC has been described in Section 4.3. In this section we inter-compare performance of ABI CM and SST QC.

### 4.7.1 Description of the ABI CM and SST QC

The objective of ABI cloud mask is clear-sky identification for accurate retrievals of clear-sky product. The ABI CM builds upon heritage approaches employed for AVHRR, MODIS and SEVIRI (Heidinger, 2009). It includes up to 30 different tests, with 10 tests being relevant to ocean applications (cf. Table 4.7). Thresholds in the individual ABI CM tests have been tuned against CALIPSO Lidar measurements. Online RTM (PFAAST) simulations are employed in several ABI CM tests (12, 13, 21, and 22, cf. Table 4.7). Target misclassification rate ('False Clear' + 'False Cloudy') is 13%. The latest tests over ocean demonstrated a misclassification rate of 8.8% wrt CALIPSO data. The ABI CM output contains results of the individual cloud tests, which are further aggregated into the overall ABI CM with four states: "Confidently Clear," "Probably Clear," "Probably Cloudy," and "Confidently Cloudy."

For the ABI SST application we applied the following modifications to the original ABI CM mask: (1) to avoid day-night discontinuity, we eliminated all reflectance-bases and MIR tests, and constructed mask from TIR-based tests; (2) to facilitate comparison of ABI CM and SST QC we aggregated two "Probably" categories, resulting in ABI CM mask with three states: "Clear," "Probably," and "Cloudy" (cf. Table 4.9).

The objective of the SST quality control is assessment of the SST retrieval's accuracy, degraded by various environmental factors (possible contamination due to residual cloud, aerosols, sun glint, radiometric noise, extreme observation geometry, proximity to coast, etc). While ABI CM is relatively liberal to avoid misclassification of clear pixels as cloudy (false alarms), the QC is more conservative to avoid cloud leakage in the SST product. Thus, the implementation of the SST QC is different from ABI CM. It currently utilizes 5 tests (cf. Table 4.8). All tests (except

'Spatial Uniformity') rely on the CRTM simulations driven by *a priori* information (Reynolds SST and GFS atmospheric fields) (Liang et al., 2009). Significant reliance on *a priori* information is essential to meet high accuracy SST requirements, without significant reduction in the amount of clear-sky pixels. The SST QC output contains results of the individual QC tests, which are further aggregated into an overall SST QC with three states: "Optimal," "Sub-Optimal," and "Poor" (cf. Table. 4.9).

The schematic plot illustrating the relationship between ABI CM and SST QC as implemented in the AIT framework is shown in Fig. 4.14. Upstream other L2 products, ABI CM will be executed for all ABI pixels, while SST QC will pass-through 'Cloudy' and further inspect 'Clear' and 'Probably' categories. The advantages of this scheme for the ABI SST product are: (1) save time by executing SST QC only over small portion of potentially non-contaminated pixels identified by ABI CM; (2) periodically check the performance of the reference-based SST QC with independent physically-based ABI CM.

### 4.7.2 Intercomparison of ABI CM and SST QC Performance

The performance of the ABI CM and SST QC was intercompared and their impact on the SST product was assessed using: (1) side-by-side comparison of ABI CM and SST QC; (2) ABI CM vs. SST QC Confusion Matrix analysis. Further details, including analysis of performance of individual ABI CM and SST QC tests are given in Shabanov et al. (2010).

Time series of the components of ABI CM ('Clear', 'Probably' and 'Cloudy') and SST QC ('Optimal', 'Suboptimal', and 'Poor') are shown in Figure 4.15 (left column). Although the fractions of top category pixels identified by the ABI CM and SST QC are different, they both exhibit diurnal cycle with a minimum found at 04:00 UTC and maximum at 14:00 UTC. Overall, the fraction of 'Clear' CM pixels (17-23%) is larger than the fraction of 'Optimal' QC pixels (16-19%). Furthermore, the fraction of 'Probably' ABI CM pixels (~18%) is much larger than that of "Sub-Optimal" SST QC pixels (~6%). Additional analysis (not shown) suggests that the pattern of ABI CM exhibits temporal discontinuities between day - night, and glint - no glint areas and artifacts in the areas contaminated by aerosols, while SST QC is more regular and continuous in time. For this reason we modified ABI CM mask to retain only thermal-channels based tests.

Time series of data screening rate by individual ABI CM and SST QC tests are shown in Fig. 4.15 (right column). The unique feature of the SST QC tests is that their triggering rates are clustered together around 70-80%, suggesting that all QC tests are consistently tuned and work for SST screening. However, some tests may be performing a redundant job. This redundancy mainly comes from the fact that majority of tests (except 'Spatial Uniformity') are derived from the common concept of comparing retrievals and references (SSTs or BTs).

In contrast, ABI CM individual tests have a wide distribution of triggering rates. Triggering rates of thermal channel based tests are flat through the diurnal cycle with rates ranging from 75% ("Thermal Uniformity") to below 1% ("Uniform Low Stratus"). Reflectance based tests ("Reflectance Uniformity", "Reflectance Gross Contrast", "Relative Visible Contrast", "4-micron emissivity", and "Uniform Low Stratus") have a wide variation (0-60%) of triggering rates. Thus, ABI CM tests are uniquely tailored to filter particular cloud types. One major disadvantage of ABI CM (from SST applications point of view) is that reflectance-based tests

contribute to day-night, glint-no-glint discontinuities and sometimes confusion of clouds and aerosols. As mentioned earlier those tests were excluded from the mask.

Figures 4.16 and 4.17 quantify the impact of ABI CM and SST QC screening on SST anomalies, $\Delta T_S$ = Hybrid SST – Reynolds SST. According to Fig. 4.16, spatial patterns of ABI CM and SST QC $\Delta T_S$ are generally similar. Namely, both capture "hot spots" along the African coast and in the Mediterranean Sea, which are not captured by coarse resolution 1° weekly Reynolds SST. However, residual clouds are more pronounced in the ABI CM (e.g., cold anomalies in the NW part of the Atlantic Ocean and in the Mediterranean Sea).

Figure 4.17 shows statistics for $\Delta T_S$ screened with ABI CM and SST QC. In the case of ABI CM, the cold tail of the $\Delta T_S$ histogram is more pronounced, while in the case of SST QC, the histogram is skewed on the right, suggesting a slight "over-screening." However, right shoulders of both histograms match very closely. Instantaneous values of mean and STD of $\Delta T_S$ statistics are indicated in the histograms and their respective diurnal cycles are shown separately. Mean $\Delta T_S$ is biased negative and shows a more pronounced diurnal cycle compared to SST QC, suggesting more residual cloud contamination in the ABI CM. This observation is further confirmed by the time series of standard deviations, which show that STDs for the ABI CM are a factor of ~3 larger than for SST QC. Figure 4.17 clearly indicates that the ABI CM alone is not sufficient to provide highly accurate SST retrievals, and additional SST QC is required.

A confusion matrix analysis complements the side-by-side comparison of ABI CM and SST QC. We will use SST QC as a "Reference" as a matter of convention (as opposed to a true reference, in view that SST QC has its own uncertainties). The main *rationale* behind this convention is: (1) convenience of commonly accepted nomenclature; (2) by construction SST QC should be intrinsically more accurate than ABI CM as former relies on SST references. We trace the following key components of the confusion matrix:

***Both Clear*** ≡ *[QC='Optimal'] ∩ [CM='Clear']*,

***False Cloudy*** ≡ *[QC='Optimal'] ∩ [CM='Cloudy']*,

***False Clear*** ≡ *[QC='Poor'] ∩ [CM='Clear']*.

Figure 4.18 shows time series of the above three components. The majority of ABI CM "Clear" and SST QC "Optimal" pixels are consistent. As a result, the "Both Clear" component comprises 9-15% of all ocean pixels. The 'False Clear' rate of ~5-7% highlights liberal setting of ABI CM. Overestimation of 'Clear' pixels is acceptable, as SST QC will be applied on the top of the ABI CM, and will catch the residual clouds missed by the ABI CM. From other side, very low rate of 'Cloudy' overestimation ('False Cloudy' rate of ~0.5%) allows SST QC to pass-through 'Cloudy' pixels and focus on refining 'Clear' and 'Probably' categories. The diurnal cycle of the corresponding $\Delta T_S$ statistics are shown in Fig. 4.19. Note that the statistics of the 'Both Clear' and 'False Cloudy' categories are close. On the other hand, the 'False Clear' ABI CM pixels form a distinct cluster with negative $\Delta T_S$ and large STD.

Overall, ABI CM performance evaluated wrt SST QC taken as reference meets the ABI cloud mask ATBD specs (Heidinger, 2009). Total misclassification error wrt SST QC ('False Cloudy' + 'False Clear') is ~5-7% of all ocean pixels. Further, confusion matrix analysis confirms feasibility of sequential execution of ABI CM and SST QC in the AIT framework, such that SST QC improves on initial data screening of ABI CM.

***Table 4.7*** *ABI Cloud Mask tests relevant to Ocean applications. Reflectance and MIR-channel based tests were further excluded from ABI CM to ensure temporal continuity (shaded boxes), and only TIR-channels based tests were retained (solid boxes).*

| Test ID | Test Name | Description |
|---|---|---|
| 09 | RUT- Reflectance Uniformity Test | STD of the observed 0.6 μm reflectance within a 3x3 box surrounding each pixel checked against a globally fixed threshold (Reflectance analog of TUT). |
| 10 | TUT- Thermal Uniformity Test | STD of the observed 11 μm BT within a 3x3 box surrounding each pixel checked against a globally fixed threshold (Thermal analog of RUT). |
| 11 | RTCT- Relative Thermal Contrast Test | BT difference @ the 11 μm (Pixel minus Nearest Warm Center in 5x5 box) checked against a globally fixed threshold. |
| 12 | ENTROP- Emissivity at Tropopause. | Effective emissivity of a pixel is compared against a fixed threshold. For cloud at the tropopause, emissivity is elevated, while for clear sky it approaches 0. |
| 13 | PFMFT- Positive 4-5 Test | Split window test for semi-transparent cloud ΔBT=BT(11 μm)-BT(12 μm) is checked against the pre-calculated ΔBT as a function of BT(11 μm). |
| 16 | RFMFT - Relative 4-5 Test | Split-window test. Significant deviations of pixel's ΔBT in 5x5 box from that at the NWC (positive or negative) are indicative of cloud. |
| 17 | RGCT - Reflectance Cross Contrast Test | Clouds exhibit large values of the visible reflectance compared to clear sky. |
| 18 | RVCT - Relative VIS Contrast Test | Relative VIS Contrast Test - over small region (5x5 box, cloud edge), cloudy pixels have largest contrast in VIS reflectance. Unlike RGCT, the RVCT test dynamically calculates its thresholds. |
| 21 | EMS4 - 3.9 μm Emissivity Test | 3.9 μm emissivity for clouds is augmented, and near zero for clear sky. |
| 22 | ULST - Uniform Low Stratus Test | Low uniform stratus clouds are more reflective (less emissive) than the surface in the 3.9 μm. Test compares pixel emissivity with clear sky prediction @ Night. |

***Table 4.8*** *SST Quality Control tests.*

| Test ID | Test Name | Description |
|---|---|---|
| 01 | Radiance Test | Checks for consistency between the observed BT @ 11μm and 12μm BT and those generated by CRTM for clear sky conditions. |
| 03 | Static SST Test | Detects unrealistically cold SST anomalies. |
| 02 | Adaptive SST Anomaly Test | Refines results of Static SST test, by analyzing statistics of clear/cloudy pixels within the neighborhood of the tested pixel. |
| 05 | Optical Depth Test | Checks optical depth generated by SST physical retrieval algorithm (high for clouds). |
| 07 | Spatial Uniformity Test | Detects fractional sub-pixel cloudiness by the presence of increased spatial variability in the retrieved SST. |

***Table 4.9*** *Correspondence between ABI CM and SST QC categories.*

| ABI CM | | SST QC | |
|---|---|---|---|
| Clear | 3 | 0 | Optimal |
| Probably Clear | 2 | 1 | Sub-Optimal |
| Probably Cloudy | 1 | 2 | Poor |
| Cloudy | 0 | 2 | Poor |
| ----- / -------- | | 3 | Unprocessed |

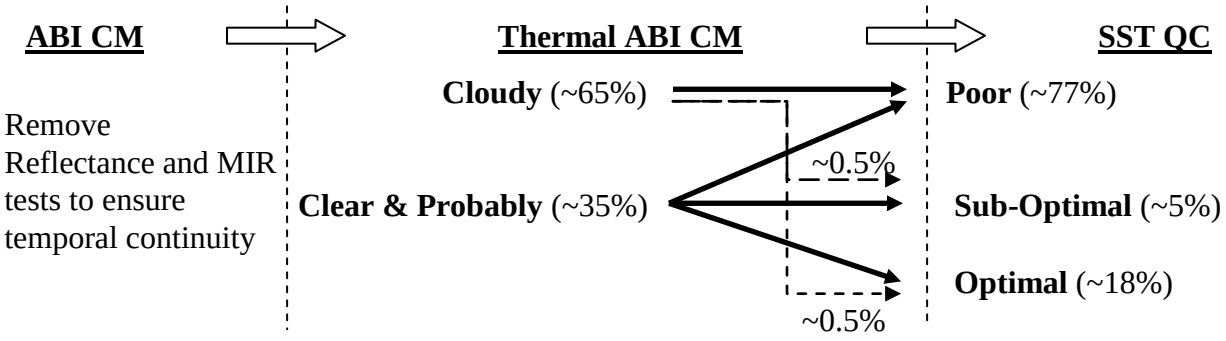


***Figure 4.14*** *Schematic plot of sequential implementation of ABI CM and SST QC masks in the AIT framework.*

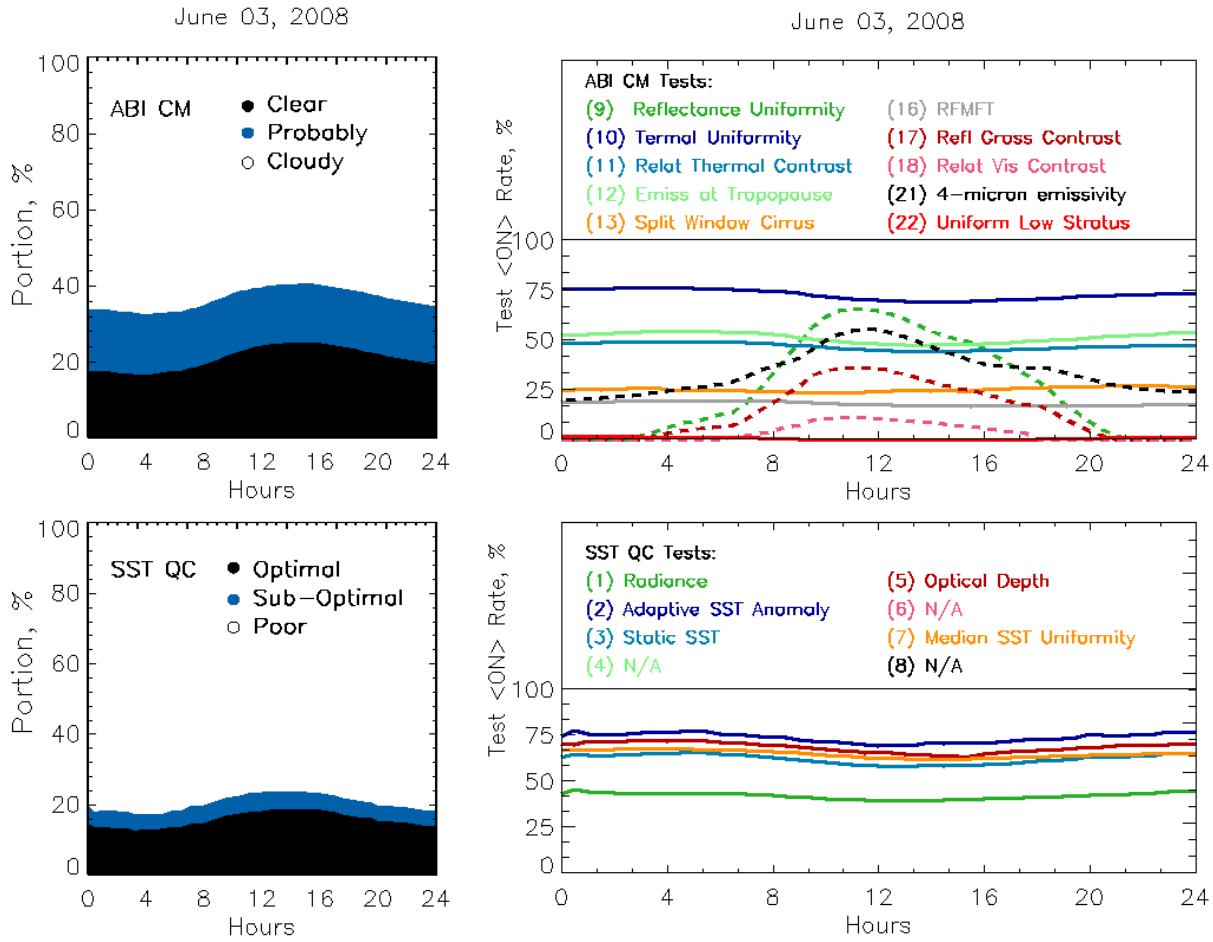


***Figure 4.15*** *Time series of the ABI CM (top row) and SST QC (bottom row) portion of retrieval states (on the left) and triggering rates of individual tests (on the right) over whole diurnal cycle. Each portion is defined as the amount of pixels falling in the state normalized by total amount of ocean pixels. Solid lines indicate TIR-channels based tests, while dashed lines correspond to optical- and MIR- channels based tests. MSG-2 SEVIRI 15-min FD data on June 03, 2008.*

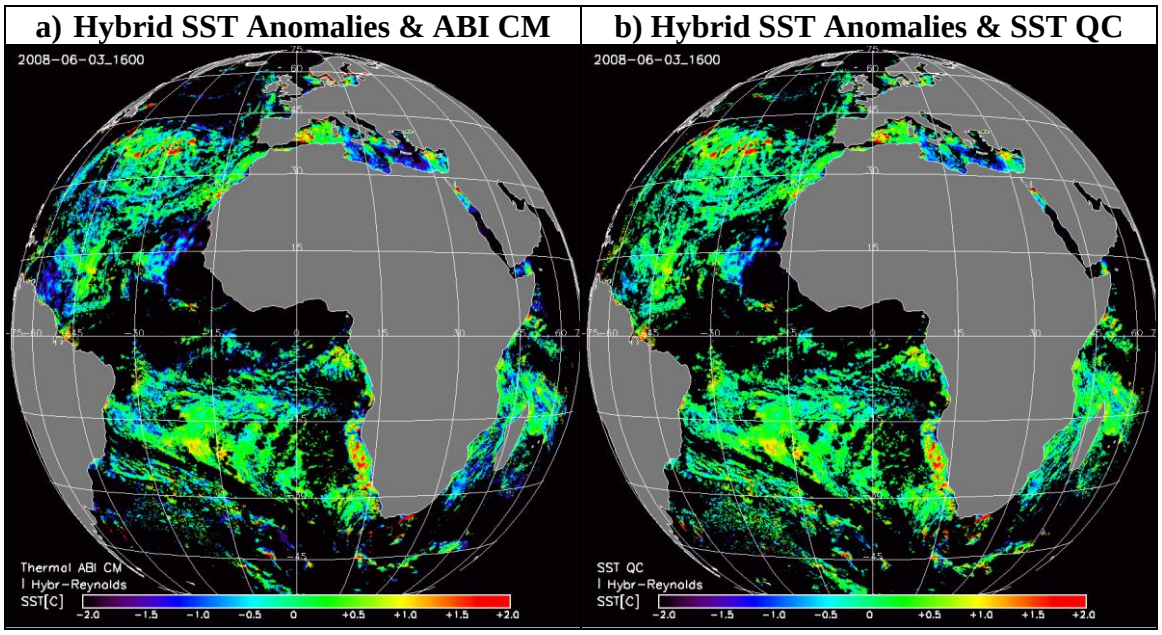


***Figure 4.16*** *Spatial distribution of SST anomalies ($\Delta T_S$ = Hybrid SST – Reynolds SST) screened with ABI CM (a) and SST QC (b) masks. MSG-2 SEVIRI 15-min Full Disk (FD) data on June 03, 2008 at 16:00 UTC.*

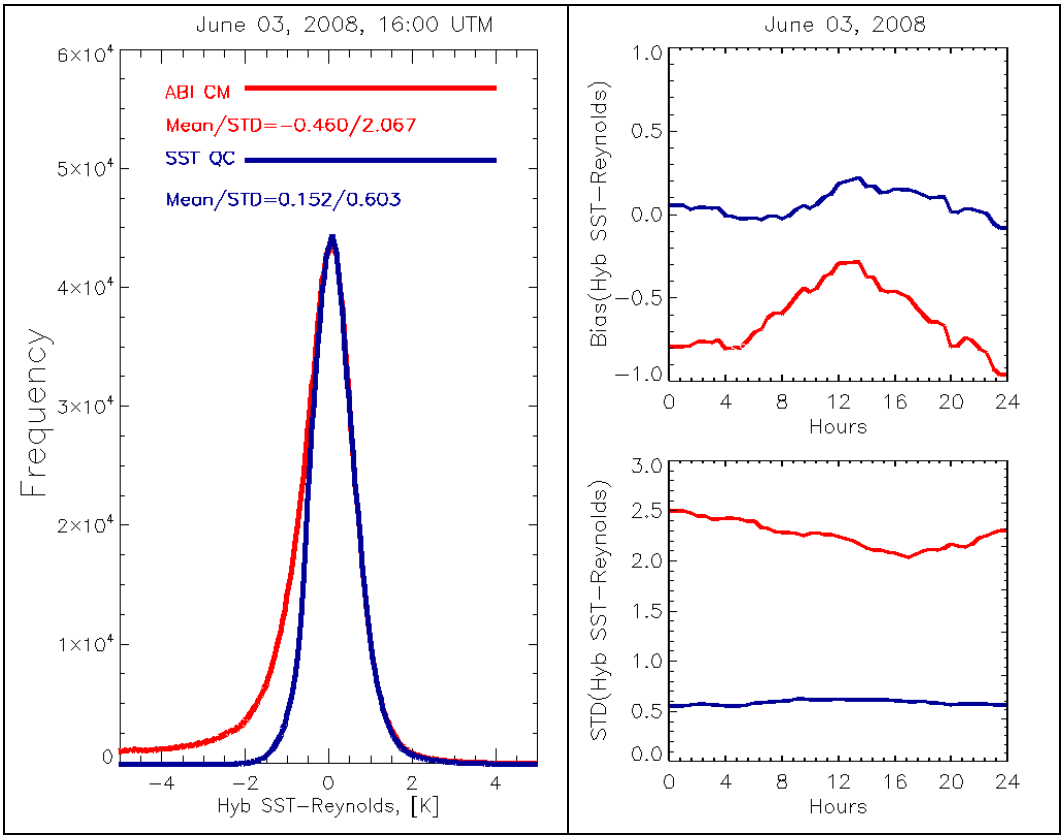


***Figure 4.17*** *Statistics for the SST anomalies ($\Delta T_S$) screened with ABI CM (in red) and SST QC (in blue) masks. MSG-2 SEVIRI 15-min FD data on June 03, 2008.*

| 12:00 UTC | SST QC | Optimal | Sub-Optimal | Poor |
|---|---|---|---|---|
| ABI CM | 100%= | 18.1% + | 5.3% + | 76.6% |
| Clear | 24.1% + | 14.4% | 2.6% | 7.1% |
| Probably | 15.4% + | 3.2% | 2.2% | 10.0% |
| Cloudy | 60.5% | 0.5% | 0.5% | 59.5% |

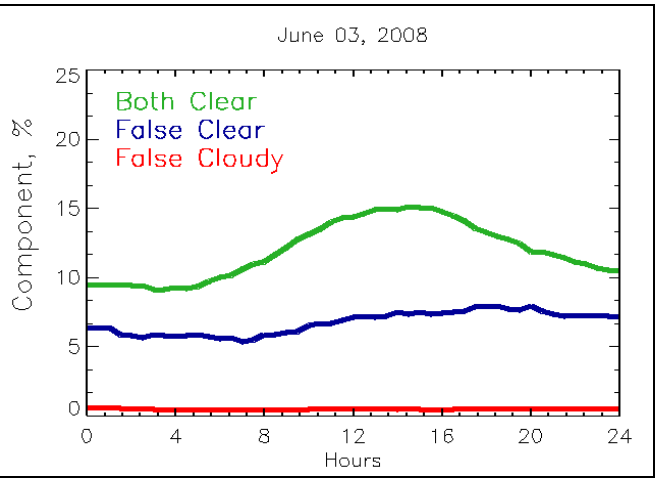


***Figure 4.18*** *Confusion matrix between ABI CM and SST QC. Components of the matrix are calculated as the amount of pixels falling in each category normalized by the total amount of ocean pixels. Color-coded are the three components of interest of the confusion matrix: 'False Clear' (red), 'False Cloudy' (blue), 'Both Clear' (green); complementary category 'Both Cloudy' (yellow) is also shown. MSG-2 SEVIRI data on June 03, 2008.*

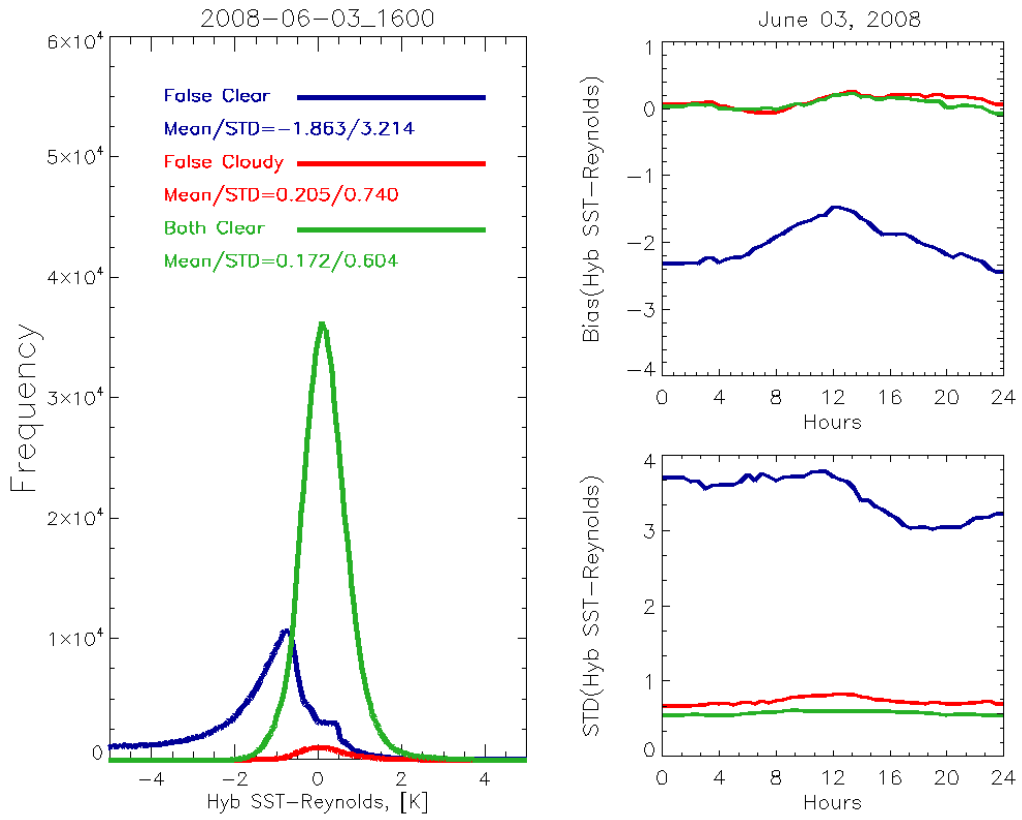


***Figure 4.19*** *Statistics of the SST anomalies ($\Delta T_S$) screened with 'False Clear' (in red), 'False Cloudy' (in blue) and 'Both Clear' (in green) components of the confusion matrix. MSG-2 SEVIRI 15-min FD data on June 03, 2008.*

## 4.8 Output Compositing

ABI will take FD images with the rate from 5 to 15 minutes while SST is required to be reported once an hour. This allows improving the coverage of the ocean surface and reduction of noise on SST images by compositing SST retrievals from several sequential SST images. One possible solution to this problem is to implement a Principal Component Analysis (PCA) technique on the time series of geostationary images (Richards and Xiuping, 2006).

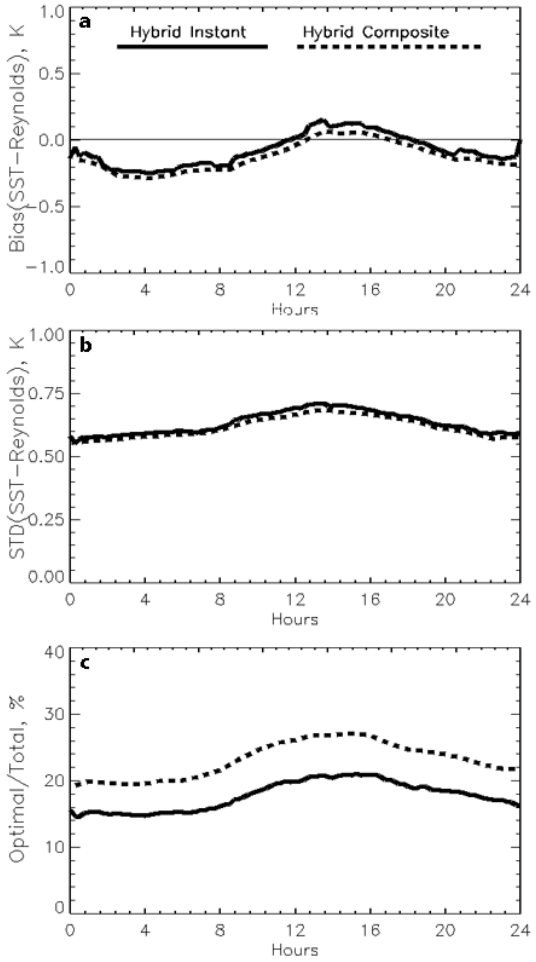


***Figure 4.20*** *Global bias (a), global STD (b) and percentage of "Optimal" pixels for instantaneous and composited SST images on June 18 2008.*

The implementation of this method is beyond the scope of this ATBD. To get the initial insight to the problem, we suggest for SEVIRI a simpler compositing algorithm: For each (x,y) pixel over the ocean and for 4 sequential 15 min FD SST images :

1. Select the pixels with "Optimal" quality flag value.
2. If at least one "Optimal" pixel found, average SST over "Optimal" pixels and set the quality flag for the (x,y) composite pixel to "Optimal."
3. Otherwise, select the pixels with "Suboptimal" quality flag value.

4. If at least one “Suboptimal” pixel found, average SST over “Suboptimal” pixels and set the quality flag for the (x,y) composite pixel to “Suboptimal.”
5. If neither “Optimal”, nor “Suboptimal pixels found, average SST over “Poor” pixels and set the quality flag for the (x,y) composite pixel to “Poor.”

The resulted composite image consists of ocean pixels with the same three categories of quality flags, which are used for the instantaneous images: “Optimal.” “Suboptimal.” and “Poor”. The effect of compositing shows itself in the increase of the amount of Optimal and in decrease of amount of Poor pixels. As an example, Fig. 4.20 shows statistics of SST anomalies over Optimal pixels for instant and composite SST images for June 18, 2008. The composite images were produced from 4 sequential SST images taken within one hour. The compositing only slightly changes global bias and STD of SST but spatial coverage with Optimal pixels increases from 15-20% to 20-27%.

## 4.9 Error Budget

Table 4.10 lists summary of SEVIRI and AVHRR validation statistics. Overall, all three SST algorithms meet the F&PS requirements. Regression SST includes the local bias component, which increases its STD over the hybrid SST. The adjusted inversion SST algorithm produces STD somewhat smaller than that for hybrid SST. The problem with the inversion algorithm is that it requires empirical adjustment because selection of the algorithm’s parameters according to theoretical recommendations causes over-smoothing of spatial and temporal SST variations within the inversion SST product. In particular, it strongly underestimates the diurnal cycle. A reasonable tradeoff between the regression and inversion SST algorithms is provided by the hybrid SST algorithm because unlike the regression, the hybrid algorithm does not include the local bias SST component and, unlike the inversion algorithm, it includes a mechanism to adjust the variance of the hybrid SST to the level of the bias-free component of regression SST. Based on the validation results for SEVIRI and AVHRR, the hybrid algorithm has been recommended as the primary algorithm for the ABI. The regression algorithm is a simple and robust approach, which can run in the absence of CRTM or its inputs (first-guess SST and atmospheric fields). It is therefore recommended as a fall-back (graceful degradation) algorithm.

The main components of the error budget for the ABI SST algorithm are: sensor BT calibration errors, CRTM BT modeling errors, ancillary GFS and reference SST field uncertainties, limitations of SST algorithms (regression, inversion, or hybrid), and CM/QC uncertainties.

**Table 4.10** *Summary of SEVIRI and AVHRR validation statistics. SST target accuracy (0.4K) and precision (0.8K) is met both for AVHRR & SEVIRI.*

| **AVHRR** | **Time Interval** | **Global Bias (K)** | **Global STD (K)** | **Diurnal Range (K)** |
|---|---|---|---|---|
| BT, Ch3B (3.7 μm) / Day | Jan 2001 - Present | CRTM inaccurate during daytime | | |
| BT, Ch3B (3.7 μm) / Night | | +0.3 | <0.5 | N/A |
| BT, Ch4 (11 μm) | | +0.5 | 0.55 | N/A |
| BT, Ch5 (12 μm) | | +0.5 | 0.65 | N/A |
| **SST (Regression)** | | **±0.1** | **0.55** | **~0.3±0.1** |
| **SST (Hybrid)** | | **±0.1** | **0.45** | **~0.3±0.1** |
| **SEVIRI** | **Time Interval** | **Global Bias (K)** | **Global STD (K)** | **Global Diurnal Range (K)** |
| BT, Ch04 (3.9 μm) / Day | Jun 2008 & Jan 2009 | CRTM is inaccurate during daytime | | |
| BT, Ch04 (3.9 μm) / Night | | -1.0 | N/A | N/A |
| BT, Ch09 (10.8 μm) | | +0.5 | 0.55 | N/A |
| BT, Ch10 (12.0 μm) | | +0.4 | 0.65 | N/A |
| **SST (Regression)** | | **±0.4** | **0.55** | **0.3** |
| **SST (Inversion)** | | **±0.2** | **0.46** | **0.23** |
| **SST (Hybrid)** | | **±0.2** | **0.50** | **0.25** |

Below we briefly discuss each component and propose mitigation strategies where applicable.

- Sensor BT calibration errors. Impact of the change in the sensor channel calibration on SST was investigated with SEVIRI data. On May 05, 2008 08:00AM EUMETSAT changed the calibration of SEVIRI MSG-1 (and 2) data to resolve an internal inconsistency in calibration methodology. This resulted in an average 0.5 [K] shift in channel BTs and translated to an increase in SST bias wrt reference fields of a similar magnitude. To mitigate these types of problems, the on-line bias correction algorithm has been implemented within ACSPO, as described in Section 4.4. This algorithm dynamically tracks Model minus Observation BT bias, retrieved minus NWP SST biases, and some other variables. The bias estimates are further taken into account in QC and OE SST algorithms. Nevertheless, according to contractual specifications, SST developers may assume that sensor data are properly calibrated (i.e., calibration risk is external).
- CRTM BT modeling errors is the second component of the problem of Model minus Observation BT biases for clear-sky conditions. Currently, the global "Model minus Observation" bias is +0.3 ~ +0.5 [K] for SEVIRI Channels 9-10 and AVHRR Channels 4-5. AVHRR Channel 3B has a mismatch of similar magnitude. However, the corresponding SEVIRI Channel 4 has an abnormal bias (cf. Fig. 3.9). This was investigated and attributed to the extended bandwidth of SEVIRI Channel 4 and associated large absorption, which CRTM fails to simulate with the currently provided number of vertical layers. Overall, CRTM will improve over time and global biases are expected to decrease by including AOD, surface emissivity, glint, etc. in the CRTM simulations. While biases exist, the mitigation strategy (implemented both for AVHRR and SEVIRI) is to perform bias corrections according to the

methods described above or perform retrievals based on bands where the biases are within a certain tolerance.

- Ancillary GFS and reference SST field uncertainties. Retrievals from temporally high-frequency geostationary data require timely and accurate CRTM input. SST retrievals (including OE and hybrid SST and QC) are highly sensitive to GFS corruption, as test cases with SEVIRI demonstrate. The mitigation strategy is to use multiple GFS forecast periods. We have enabled input of 6-, 9- and 12- hours GFS forecasts for SEVIRI retrievals.
- Limitations of SST models. The regression algorithm is sensitive to calibration trends and retrievals can be biased at some combinations of input variables, for example large local zenith angles and high water vapor content in the atmosphere. The optimal estimation algorithm is sensitive to the errors in CRTM and input NWP fields. In addition, uncertainties in OE SST depend on the difference between the retrieved and first guess SST. In order to provide the optimal retrieval stability in the wide range of observational conditions, the hybrid algorithm has been developed, as described in Section 4.2.3.
- CM/QC uncertainties. The quality of the SST product strongly depends on the quality of screening out SST pixels with atmospheric contamination. According to the ABI AIT strategy, this screening will be performed by the external cloud mask upstream to SST production. The additional and final screening will be done by the SST QC, as decribed in Section 4.3. Our analysis and intercomparison of current ABI external CM and internal QC (Section 5.6) indicates that while CM captures the majority of clouds, significant False Cloud and False Clear misclassification exist. The mitigation strategy is to combine the external CM and the internal QC in such a way as to provide optimal and efficient detection of cloudy pixels while maintaining a low false alarm rate.

Finally note that product uncertainties should match that of the validation data sets. Currently the most accurate data set available is GTS buoy measurements, which have measurements uncertainties of about 0.3 [K] (O'Carrol et al., 2008).

# 5 PRACTICAL CONSIDERATIONS

## 5.1 Numerical Computation Considerations

1. SST inversion/hybrid algorithm is computationally more expensive than the regression algorithm, but provides a more accurate SST product.
2. Both algorithms will meet the algorithm latency requirement (< 15 minutes, goal) on the current STAR computers.
3. Coarser resolution ancillary input files (Reynolds SST data and etc) will be interpolated to satellite pixel scale.
4. Retrieved SST's will be used to support additional quality control of the ABI cloud mask.

## 5.2 Programming and Procedural Considerations

1. Hybrid and regression SST will be the primary and the fall-back SST products, respectively.

2. If NCEP/GFS global fields are not available, the fall-back regression product may be used and the SST product will be degraded.
3. Both SST algorithms require initial training against *in-situ* SST, followed by periodic check-ups and potential adjustments. The corresponding procedures will be incorporated into the SST processing system.
4. Frequent temporal sampling (15 min for SEVIRI) will be used to mitigate data issues (noise, cloud), fill in data gaps, and extend product coverage and accuracy/precision.
5. The SST algorithms are purely pixel-by-pixel algorithms, implemented in a sequential mode. However, such QC tests as Adaptive SST and Spatial Uniformity will require analysis of the pixels in each pixel's immediate neighborhood.
6. Generating L3 and 4 SST products tailored to customers needs may require further processing of pixel-level retrievals (not discussed in this ATBD).

The primary adjustable parameters for the SST retrieval are the coefficients of the regression algorithm that may be stratified by day and night. The source of ancillary data sets should be configurable for the best available data set. Metadata used in this product may be modified, reduced and added later, at the stage of the product generation.

## 5.3 Quality Assessment and Diagnostics

The quality of SST retrieval will be assessed and monitored for diagnostics purposes. A set of quality control flags will be generated on a per pixel basis and stored as separate data layers including SST QC and Individual SST QC Tests (Tables 3.12-3.13). QC maps generated per pixel will be accompanied by image-wide QC statistics stored as part of the metadata (cf. Table 3.11).

## 5.4 Exception Handling

The SST processing takes into account the quality of input channel data as well as ancillary data (upper air GFS input to CRTM and Reynolds First Guess SST). To handle situations with missing/corrupted data we have implemented a graceful degradation approach. That is, an attempt is made to continue retrievals based on best available analogous inputs (climatology, adjacent in time data, etc). Table 5.1 summarizes different cases of exception handling. The results are reflected in the output SST QC.

***Table 5.1*** *Exception handling summary.*

| Algorithm | Type of missing data | | |
|---|---|---|---|
| | Measurements (11 or 12 μm channels) | NCEP GFS fields | Reynolds SST |
| Hybrid | Fails | Graceful degradation: Replaced with prior field or climatology | Graceful degradation: Replaced with prior field or static SST climatology. |
| Regression | Fails | Graceful degradation: CRTM based QC tests will be switched off | Graceful degradation: Replaced with prior field or static SST climatology. |

## 5.5 Algorithm Online Validation

### 5.5.1 Pre-launch Validation

Near-real time validation for the AVHRR and SEVIRI SST products is currently being established, and its results will be reported on the web.

Monitoring of AVHRR SST in near-real time for long-term stability and cross-platform consistency is currently performed against global reference fields using the web-based SST Quality Monitor (SQUAM), www.star.nesdis.noaa.gov/sod/sst/squam/. More information about the SQUAM tool, including monitoring results and relevant references are found online (Dash et al., 2009).

An automatic web-based Cal/Val system against *in situ* SSTs is currently being established for AVHRR, www.star.nesdis.noaa.gov/sod/sst/calval/. As of this writing, the tool continues to be under development and is password protected. More information about the tool, monitoring results, and relevant references are found online (Ignatov et al., 2009).

Monitoring of IR Clear-sky Radiances over Oceans for SST (MICROS) is another web-based near-real time tool, www.star.nesdis.noaa.gov/sod/sst/micros/, employed to monitor radiances associated with SSTs. It validates SST radiances against the CRTM radiances calculated using NCEP GFS and Reynolds SST as input. More information about the tool, monitoring results, and relevant references are found online and in (Liang and Ignatov, 2009).

### 5.5.2 Post-launch Validation

Work is underway to add SEVIRI retrievals to the SQUAM, CALVAL, and MICROS pages. One specific requirement of the SEVIRI analyses is that they will need to resolve diurnal cycle. Establishing a NRT monitoring system for SEVIRI will allow a quick evaluation of the ABI SSTs and associated clear-sky radiances, once GOES-R is in orbit.

During the initial intensive Cal/Val period (during the first several months in orbit), field measurements such as M-AERI would be instrumental in evaluating the SST product. This validation would be particularly helpful in light of the fact that the major SST product derived from ABI is the skin SST, also measured by the M-AERI (Minnett et al., 2001; Minnett, 2003).

# 6 ASSUMPTIONS AND LIMITATIONS

## 6.1 Performance

The following assumptions have been made in developing and estimating performance of ABI SST retrievals.

1) The ABI cloud mask is available.
2) Community Radiative Transfer Model (CRTM) is available.
3) NCEP/GFS and Reynolds SST are available.
4) ABI sensor performance is as specified in the MRD and GS F&PS.
5) SST regression and hybrid algorithms will be available pre-launch but their coefficients will be trained post-launch using match-up data with in-situ SSTs.

6) Static data sets (navigation, geometry, land/water mask) are available and within accuracy limits.

## 6.2 Assumed Sensor Performance

It's assumed that the ABI sensor will meet its current specifications. However, SST will be degraded under the following unfavorable observational conditions (degree of degradation is TBD)

a. Under degraded sensor performance (calibration, stability, NEdT, band-to-band co-registration, navigation)
b. Under heavy ambient or persistent cloud
c. Under unfavorable Illumination/Observation conditions (twilight zone, limb of disk, glint)
d. Under heavy aerosol conditions
e. In coastal waters

## 6.3 Pre-Planned Product Improvements

Experience accumulated during prototyping of the ABI SST algorithm with proxy data (AVHRR, SEVIRI, and others) will guide further optimization of the SST algorithm especially when applied to actual ABI data:

- Optimization of existing SST algorithm parameters. Testing different techniques, for multi-channel SST retrievals. Optimizing retrievals in proximity to special cases (twilight zone, glint, etc).
- Continue designing a robust hybrid algorithm to improve retrieval of spatial and temporal SST variations.
- Refining CRTM simulations (inclusion of aerosols, etc) to minimize "Model-Observation" bias in BT Channel data.
- Optimization of the QC tests.
- Enhancement of the ABI external cloud mask with screening provided by SST internal QC.
- Substitute hourly compositing algorithm with the robust PCA-based system which provides data compression and gap filling.

# 7 REFERENCES


Autret, E. & J.-F. Piollé, 2007: ODYSSEA Global SST Analysis – User's manual, MERSEA-WP02-IFR-STR-001-1A, CERSAT – IFREMER. http://cersat.ifremer.fr/data/discovery/by_parameter/sea_surface_temperature/odyssea_global_sst_analysis

Bard, Y., 1973: *Nonlinear parameter estimation.* Academic Press, 300 pp.

Barton, I., & R. Cechet, 1989: Comparison and Optimization of AVHRR SST Algorithms. *JTech*, 6, 1083–1089.

Barton, I, et al., 1989: Theoretical Algorithms for satellite-derived SSTs. *JGR*, 94, 3365-3375.

Barton, I., 1992: Satellite-derived SST-A Comparison between Operational, Theoretical, and Experimental Algorithms. *JAM*, 31, 433–442.

Barton, I., 1995: Satellite derived SSTs: Current status. *JGR*, 100, 8777-8790.

Berk, A., et al., 1998: MODTRAN cloud and multiple scattering upgrades with application to AVIRIS. *RSE*, 65, 367–375.

Berk, A., et al., 2000: MODTRAN4 Version 4.2 User's Manual, Space Vehicles Directorate, Hanscom AFB, MA 01731-3010.

Brisson, A, P. Le Borgne & A. Marsouin, 2002: Results of one year of preoperational production of SST from GOES-8. *JTech*, 19, 1638–1652.

Brown, O. & P. Minnett, 1999: MODIS Infrared SST Algorithm, ATBD, v2.0, University of Miami, Miami, FL (1999, Apr. 30) 33149–1098 (available at: *http://modis.gsfc.nasa.gov/data/atbd/ocean_atbd.php*)

Casey, K. & P. Cornillon, 1999: A comparison of satellite and *in situ* based SST climatologies. *JClim*, 12, 1848-1863.

Casey, K. & P. Cornillon, 2001: Global and regional SST trends. *JClim*, 14, 3801-3818.

Castro S.L., G.A. Wick & W.J. Emery, 2003: Further refinements to models for the bulk-skin SST difference. *JGR*, 108, 3377, doi:10.1029/2002JC001641.

Castro S.L., G.A. Wick, D.L. Jackson, & W.J. Emery, 2008: Error characterization of infrared and microwave satellite SST products for merging and analysis. *JGR*, 113, C03010, doi:10.1029/2006JC003829.

Castro S.L., G.A.Wick, P.J. Minett, A.T. Jessup, & W.J. Emery, 2010: The impact of measurement uncertainty and spatial variability on the accuracy of skin and subsurface regression-based sea surface temperature algorithms. *RSE*, 114, 2666-2678.

Chédin, A., N. Scott, C. Wahiche & P. Moulinier, 1985: The improved initialization inversion method: A high resolution physical temperature retrieval from TIROS N series, *J. Clim. Appl. Meteorol*, 24, 128–143.

Chin, M., R.B. Rood, S.-J. Lin, J.F. Muller & A.M. Thomspon, 2000: Atmospheric sulfur cycle in the global model GOCART: Model description and global properties, *JGR*, 105, 24,671-24,687.

Dash, P. and A. Ignatov, 2008: Validation of Clear-Sky Radiances over Oceans Simulated with MODTRAN4.2 and Global NCEP GDAS Fields against nighttime NOAA15-18 and MetOp-A AVHRR Data. *RSE*, 112, 3012-3029.

Dash, P., A. Ignatov, Y. Kihai, & J. Sapper, 2009: The near real-time web-based SST Quality Monitor (SQUAM): Application to NESDIS heritage AVHRR product. In prep.

Deschamps, P.Y. & T. Phulpin, 1980: Atmospheric correction of infrared measurements of SST using channels at 3.7, 11 and 12 μm, *Boundary-Layer Meteorology*, 18, 131–143.

Donlon, C.J., K.S. Casey, C. Gentemann, et al., 2009: Successes and challenges for the modern SST observing system, OceanObs09 Meeting.

Donlon, C.J., S.J. Keogh, D.J. Baldwin, et al, 1998: Solid-state radiometer measurements of skin SST. *JTech*, 15, 775-787.

Donlon, C.J., P.J. Minnett, C. Gentemann, et al., 2002: Toward improved validation of satellite sea surface skin temperature measurements for climate research, *JClim*, 15, 353–369.

Donlon, C.J. & I.S. Robinson, 1997: Observations of the oceanic thermal skin in the Atlantic Ocean. JGR, 102, 18585-18606.

Downing, H.D., & D. Williams, 1975: Optical constants of water in the infrared. *JGR*, 80, 1656–1661.

Emery, W.J., Y. Yu, G.A. Wick, P. Schluessel & R.W. Reynolds, 1994: Correcting infrared satellite estimates of SST for atmospheric water vapor attenuation, *JGR*, 99, 5219–5236.

Emery, W.J., D.J. Baldwin, P. Schluessel, and R.W. Reynolds, 2001: Accuracy of *in situ* SSTs used to calibrate infrared satellite measurements. *JGR*, 106, 2387-2405.

EUMETSAT-1, A Planned Change to the MSG Level 1.5 Image Product Radiance Definition. http://www.eumetsat.int/Home/Main/Access_to_Data/Meteosat_Image_Services/SP_1123237865326

EUMETSAT-2, Effective Radiance and Brightness Temperature Relation for Meteosat 8 and 9. http://www.eumetsat.int/Home/Main/Access_to_Data/Meteosat_Image_Services/SP_1123237865326

Fairall, C.W. et al, 1996: Cool-skin and warm-layer effects on SST. *JGR*, 101, 1295-1308.

François, D. & C. Ottlé, 1996: Atmospheric corrections in the thermal infrared: Global and water vapor dependent split-window algorithms, applications to ATSR and AVHRR data. *IEEE/TGRS*, 34, 457–470.

Friedman, D., 1969: Infrared characteristics of ocean water (1.5-15 μm). *Appl. Opt*., 8, 2073–2078.

Garand, L., 2003: Toward an integrated land–ocean surface skin temperature analysis from the variational assimilation of infrared radiances. *JAM*, 42, 570–583.

Gemmill, W., Katz, B. & X. Li, 2007: Daily real-time, global SST- high-resolution analysis: RTG_SST_HR, NOAA/NCEP. NOAA/NWS/NCEP/MMAB Office Note N260, 39 pp (http://polar.ncep.noaa.gov/sst/)

Gentemann, C.L, 2007: Diurnal warming at the ocean surface. Ph.D. Dissertation, U. Miami, 163pp.

Gentemann, C.L., C.J. Donlon, A. Stuart-Menteth & F. Wentz, 2003: Diurnal signals in satellite SST measurements. *GRL*, 30(3), 1140, doi: 10.1029/2002GL016291.

Gentemann, C.L. & P.J. Minnett (2008). Radiometric measurements of ocean surface thermal variability. *JGR*, 113, C08017, doi: 10.1029/2007JC004540.

GOES-R Program Office, GOES-R Series Mission Requirements Document (MRD), P417-R-MRD-0070, 2007.

GOES-R Program Office, GOES-R Series Ground Segment (GS) Functional & Performance Specifications (F&PS). Ver. 1.0. May 2008.

Gonzalez, R.C., and R. E. Woods, 2003: *Digital image processing*. Pearson Education (Singapore) Pte. Ltd., 793 pp.

Hale, G.M. & M.R. Querry, 1973: Optical constants of water in the 200-nm to 200-μm wavelength region. *Appl. Opt*., 12, 555–563.

Han, Y., P. van Delst, Q. Liu, F. Weng, B. Yan, R. Treadon, & J. Derber, 2006: JCSDA Community Radiative Transfer Model (CRTM) version 1. *NOAA Tech. Rep*., NESDIS 122.

Hanafin, J.A. & P.J. Minnett, 2005: Measurements of the infrared emissivity of a wind-roughened sea surface. *Appl. Opt*., 44 (3), 398-411.

Hayden, C.M., 1988: GOES-VAS simultaneous temperature-moisture retrieval algorithm. *JAM*, 27, 705-733.

Hayden, C.M., G.S. Wade & T.J. Schmit, 1996: Derived product imagery from GOES-8, *JAM*, 35, 153-162.

Heidinger, A., 2009: ABI Cloud Mask. 80% ATBD. NOAA/NESDIS/STAR.

Highwood, E.J., J.M. Haywood, M.D. Silverstone, S.M. Newman & J.P. Taylor, 2003: Radiative properties and direct effect of Saharan dust measured by the C-130 aircraft during Saharan Dust Experiment (SHADE): 2. Terrestrial spectrum. *JGR*, 108, DOI:10.1029/2002JD002552.

Hollweg, H.-D., S. Bakan & J.P. Taylor, 2006: Is the aerosol emission detectable in the thermal Infrared? *JGR*, DOI:10.1029/2005JD006432, D15202, 111, 1-13.

Horrocks, L., et al., 2003: Parameterizations of the ocean skin effect and implications for satellite-based measurement of SST. *JGR*, 108(C3), 3096, doi:10.1029/2002JC001503.

Ignatov, A., P. Dash, J. Sapper, and Y. Kihai, 2010: Heritage NESDIS AVHRR SST Calibration and Validation system. In preparation.

Ignatov, A., J. Sapper, I. Laszlo, et al., 2004: Global operational SST and aerosol products from AVHRR: Current status, diagnostics, and potential enhancements, 13th AMS Conf. on Satellite Oceanogr. Meteorol., Norfolk, Virginia, 12pp.

Kearns, E.J., J.A. Hanafin, R.H. Evans, P.J. Minnett & O. B. Brown, 2000: An Independent Assessment of Pathfinder AVHRR SST Accuracy Using the Marine Atmosphere Emitted Radiance Interferometer (MAERI). *BAMS*, 81, 1525–1536.

Kent, E.C., and P.G. Challenor, 2006: Toward estimating climatic trends in SST. Part II: Random errors. *JTech*, 23, 476-486.

Kent, E.C., and P.G. Challenor, 2006: Toward estimating climatic trends in SST. Part III: Systematic Biases. *JTech*, 23, 487-500.

Khattak, S., RA. Vaughan, & AP. Cracknell, 1991: Sunglint and its observation in AVHRR data. *RSE*, 37, 101-116.

Kilpatrick, K.A., G.P. Podesta & R. Evans, 2001: Overview of the NOAA/NASA AVHRR Pathfinder algorithm for SST and associated match-up database, *JGR* 106 (C5), 9179–9197.

Kumar, A., P.J. Minnett, G. Podestá & R.H. Evans, 2003: Error Characteristics of the Atmospheric Correction Algorithms Used in Retrieval of SST from Infrared Satellite Measurements: Global and Regional Aspects. *JAS*, 60, 575–585.

Legeckis, R. & T. Zhu, 1997: SST from GOES-8 geostationary satellite. *BAMS*, 78, 1971-1983.

Liang, X., A. Ignatov, & Y. Kihai, 2009: Implementation of the Community Radiative Transfer Model (CRTM) in Advanced Clear-Sky Processor for Oceans (ACSPO) and validation against nighttime AVHRR radiances. *JGR*, 114, D06112, doi:10.1029/2008JD010960.

Liang, X., and A. Ignatov, 2010: Monitoring of IR Clear-sky Radiances over Oceans for SST (MICROS): Near-Real Time Web-based Tool for Monitoring CRTM - AVHRR Biases. *JGR*, submitted.

Liu, Q., X. Liang, Y. Han, P. van Delst, Y. Chen, A. Ignatov, and F Weng, 2009: Effect of out-of-band response in NOAA-16 AVHRR Channel 3B on top-of-atmosphere radiances calculated with the Community Radiative Transfer Model. *JTech*, 26, 1968-1972.

Llewellyn-Jones, D.T., P.J. Minnett, R.W. Saunders & A.M. Zavody, 1984: Satellite multi-channel infrared measurements of SST of the N.E. Atlantic Ocean using AVHRR/2. *QJRMS*, 110, 613-631.

Martins, J. V., D. Tanre, L. Remer, Y. Kaufman, S. Mattoo, and R. Levy 2002: MODIS cloud screening for remote sensing of aerosols over oceans using spatial variability, *GRL*, 29(12), 8009, doi:10.1029/2001GL013252.

Masuda, K., 2006: Infrared sea surface emissivity including multiple reflection effect for isotropic Gaussian slope distribution model. *RSE*, 103, 488–496.

Maturi, E.M., A.R. Harris, C. Merchant, J. Mittaz, B. Potash, W. Meng, and J. Sapper, 2008: NOAA's Geostationary Operational Environmental Satellites (GOES) SST products. *BAMS*, 89, 1877-1888.

McClain, E.P., W.G. Pichel & C.C. Walton, 1985: Comparative performance of AVHRR-based multi-channel SSTs. *JGR*, 90, 11,587–11,601.

McMillin, L.M., 1975: Estimation of SSTs from two infrared window measurements with different absorption. *JGR*, 80, 5113–5117.

McMillin, L.M. & D.S. Crosby, 1984: Theory and validation of multiple window SST technique. *JGR*, 89, 3655-3661.

Menzel, W. P., and J. F. W. Purdom, 1994: Introducing GOES-I: The first of a new generation of Geostationary Operational Environmental Satellites. *BAMS*, **75,** 757–781.

Merchant, C.J. & A.R. Harris, 1999: Towards the elimination of bias in satellite retrievals of SSTs. 2: Comparison with *in situ* measurements. *JGR*, 104, 23,579-23,590.

Merchant, C.J. & P. Le Borgne, 2004: Retrieval of SST from space based on modeling of infrared radiative transfer: Capabilities and limitations. *JTech*, 22, 1734–1746.

Merchant, C.J., A.R. Harris, E. Maturi, O. Embury, S.N. MacCallum, J. Mittaz, & C.P. Old, 2009: Sea Surface Temperature Estimation from the Geostationary Operational Environmental Satellite-12 (GOES-12). *JTech*, 26, 570-581.

Merchant C.J., A.R. Harris, E. Maturi & S. Maccallum, 2005: Probabilistic physically based cloud screening of satellite infrared imagery for operational SST retrieval. *QJRMS*, 131, 2735-2755.

Merchant, C.J., L.A. Horrocks, J. Eyre & A.G. O'Carroll, 2006a: Retrievals of SST from infrared imagery: Origin and form of systematic errors. *QJRMS*, 132, 1205–1223.

Merchant, C.J., O. Embury, P. Le Borgne & B. Bellec, 2006b: Saharan dust in nighttime thermal imagery: Detection and reduction of related biases in retrieved SST. *RSE*, 104 (1), 15-30.

Merchant, C. J., P. Le Borgne, A. Marsouin & H. Roquet, 2008: Optimal estimation of SST from split-window observations. *RSE*, 112, 2469-2484.

Merchant, C.J., P. Le Borgne, H. Roquet, and A. Marsouin, 2009: Sea surface temperature from a geostationary satellite by optimal estimation. *RSE*, 113, 445–457.

Minnett, P.J., 1990: The Regional Optimization of Infrared Measurements of SST From Space. *JGR*, 95, 13,497–13,510.

Minnett, P.J., 1991: Consequences of SST variability on the validation and applications of satellite measurements. *JGR*, 96, 18,475-18,489.

Minnett, P.J., 2003: Radiometric measurements of skin SST: the competing roles of the diurnal thermocline and the cool skin. *IJRS*, 24, 5033-5047.

Minnett, P.J., R.O. Knuteson, F.A. Best, B.J. Osborne, J.A. Hanafin & O.B. Brown, 2001: The Marine-Atmospheric Emitted Radiance Interferometer: A high-accuracy, seagoing infrared spectroradiometer. *JTech*, 18, 994-1013.

Minnett, P., and R. Evans, 2008: Personal Communication.

Murray, J.M., M.R. Allen, C.J. Merchant, A.R. Harris & C.J. Donlon, 2000: Direct observations of skin-bulk SST variability. *GRL*, 27, 1171–1174.

Nalli, N.R., P.J. Minnett, and P. Van Delst, 2008: Emissivity and reflection model for calculating unpolarized isotropic water surface-leaving radiance in the IR: 1: Theoretical development and calculations. *Appl. Opt.*, 47, 3701-3721.

Nalli, N.R., P.J. Minnett, and E. Maddy, W.W. McMillan, &. M.D. Goldberg, 2008: Emissivity and reflection model for calculating unpolarized isotropic water surface-leaving radiance in the IR: 1: Validation using Fourier transform spectrometers. *Appl. Opt.*, 47, 4649-4671.

Nalli, N.R. & L.L. Stowe, 2002: Aerosol correction for remotely sensed SSTs from the NOAA AVHRR. *JGR*, 107, 3172.

Nalli, N.R. & R.W. Reynolds, 2006: SST Daytime Climate Analyses Derived from Aerosol Bias-Corrected Satellite Data. *JClim*, 19, 410–428.

Nardielli, B.B., S. Marullo, R. Santoleri, 2005: Diurnal variations in AVHRR SST fields: A strategy for removing warm layer effects from daily images. *RSE*, 95, 47-56.

Nath, AN., MV. Rao, & KH. Rao, 1993: Observed high temperatures in the sunglint area over the North Indian Ocean. *IJRS*, 14, 849-853.

Newman, S.M., J.A. Smith, M.D. Glew, S.M. Rogers & J.P. Taylor, 2005: Temperature and salinity dependence of sea surface emissivity in the thermal infrared. *QJRMS*, 131, 2539-2557.

Niclòs, R., E. Valor, V. Caselles, C. Coll & J.M. Sanchez, 2005: *In situ* angular measurements of thermal infrared sea surface emissivity--Validation of models. *RSE*, 94, 83-93.

Niclòs, R., V. Caselles, C. Coll & E. Valor, 2007: Determination of SST at large observation angles using an angular and emissivity-dependent split-window equation. *RSE*, 111, 107-121.

O'Carroll, A. G., J.G. Watts, L. A. Horrocks, R.W. Saunders & N.A. Rayner, 2006: Validation of the AATSR Meteo product SST. *JTech*, 23, 711-726.

O'Carroll, A.G., J.R. Eyre and R.W. Saunders, 2008: Three-way error analysis between AATSR, AMSR-E, and *in situ* sea surface temperature observations, *J. Atmos. Oceanic Technol.*, 25(7), 1197–1207.

Pellegrini, P., M. Bucci, M. Tommasini, M. Innocenti, 2006: Monthly average SSTs. *IJRS*, 27, 2519-2539.

Petrenko, B., et al, 2009: Clear-sky mask for the Advanced Clear Sky Processor for Oceans. *Jtech*, submitted.

Pinkley, L.W., P.P. Sethna & D. Williams, 1977: Optical constants of water in the infrared: Influence of temperature. *JOSA*, 678, 494-499.

Prabhakara, C., G. Dalu & V.G. Kunde, 1974: Estimation of SST from remote sensing in the 11-13 μm window region. JGR, 79, 5039-5044.

Reynolds, R.W. & T.M. Smith, 1994: Improved Global SST Analyses Using Optimum Interpolation. *J.Clim.*, 7, 929–948.

Reynolds, R.W., N.A. Rayner, T.M. Smith, D.C. Stokes & W. Wang, 2002: An improved *in situ* and satellite SST analysis for climate. *JClim*, 15, 609–1625.

Reynolds, R.W., H.M. Zhang, T.M. Smith, C.L. Gentemann & F. Wentz, 2005: Impacts of *in situ* and additional satellite data on the accuracy of a SST analysis for climate. *Int. J. Clim.*, 25, 857-864.

Reynolds, R.W., T.M. Smith, C. Liu, D.B. Chelton, K.S. Casey & M.G. Schlax, 2007: Daily High-Resolution-Blended Analyses for SST. *JClim*, 20, 5473–5496.

Richards, J.A. and Xiuping, J. (2006) Remote Sensing Digital Image Analysis, Chapter 6: Multispectral Transformations of Image Data, pp. 137-162, Springer, 4-th Ed, 2006

Robel, J. et al., 2009: NOAA KLM user's guide, *NOAA/NESDIS*, http://www.ncdc.noaa.gov/oa/pod-guide/ncdc/docs/klm/cover.htm

Robinson, I.S., N.C. Wells & H. Charnock, 1984: The sea surface boundary layer and its relevance to the measurement of SST by airborne and spaceborne radiometers. *IJRS*, 5, 19-45.

Rogers, C. D., 1976: Retrieval of atmospheric temperature and composition from remote measurements of thermal radiation. *Rev. Geophys. Space Phys.*, **14,** 609–624.

Romaguera, M., J.A. Sobrino & F.-S. Olesen, 2006: Estimation of SST from SEVIRI data: algorithm testing and comparison with AVHRR products. *IJRS*, 27, 5081-5086.

Saunders, P.M., 1967a: Aerial measurement of SST in the infrared. *JGR*, 72, 4109-4117.

Saunders, P.M., 1967b: The temperature at the ocean-air interface. *JAS*, 24, 269-273.

Segelstein, D.J., 1981: The complex refractive index of water. M.S. thesis. U. Missouri, Kansas City, MO.

Schmetz, J, P. Pili, S. Tjemkes, D. Just, K. Kerkmann, S. Rota, & A. Ratier, 2002: An introduction to Meteosat Second Generation (MSG). *BAMS*, 83, 977-992.

Schmit, T. J., M. M. Gunshor, W. P. Menzel, J. Li, S. Bachmeier, and J. J. Gurka, 2005: Introducing the Next-generation Advanced Baseline Imager (ABI) on GOES-R, *BAMS*, **86**, 1079-1096.

Shabanov N., A. Ignatov, B. Petrenko, Y. Kihai and A. Heidinger, 2010: Towards integrated cloud mask and quality control for ABI SST product: prototyping with MSG/SEVIRI. 6th Annual Symp. NPOESS&GOES-R, 90-th AMS Annual Meeting, 17-21 January, Atlanta, GA.

Sikorski, R.J., S.W. Miller & P.S. Kealy, 2002: SST from the Visible and Infrared Imager/ Radiometer Suite, Algorithm Theoretical Basis Document, v5.1, Raytheon Systems Company, 68pp.

Smith, W.L., R.O. Knuteson, H.E. Revercomb, W. Feltz, H.B. Howell, W.P. Menzel, N.R. Nalli, O. Brown, J. Brown, P. Minnett & W. McKeown, 1996: Observations of the infrared radiative properties of the ocean – implications for the measurement of SST via satellite remote sensing. *BAMS*, 77, 41–51.

Sobrino, J. A., Z.L. Li & M.P. Stoll, 1993: Impact of the atmospheric transmittance and total water vapor content in the algorithms for estimating SSTs. *IEEE/TGRS*, 31, 946-952.

SSA-MTM toolkit for spectral analysis http://www.atmos.ucla.edu/tcd/ssa/

Stark, J.D., C.J. Donlon, M.J. Martin & M.E. McCulloch, 2007: OSTIA. Oceans'07 IEEE Aberdeen, Marine challenges: coastline to deep sea. 18-22 June, 2007, Aberdeen, Scotland.

Steyn-Ross, M.L., D.A. Steyn-Ross & A. Jelenak, 1999: Comparison of atmospheric correction algorithms for deriving SST from AVHRR. *IJRS*, 20, 3515–3531.

Steyn-Ross, M.L., D.A. Steyn-Ross & W. Emery, 1997: A dynamic water vapor correction method for the retrieval of land surface temperature from AVHRR. *JGR*, 102, 19629–19643.

Stuart-Menteth, A.C., I.S. Robinson & P.G. Challenor, 2003: A global study of diurnal warming using satellite-derived SST. *JGR*, 108, 3155, doi:10.1029/2002JC001534.

Tanashi, S., H. Kawamura, T. Takahashi & H. Yusa, 2003: Diurnal variations of SST over the wide-ranging ocean using VISSR onboard GMS. *JGR*, 108, 3216, doi:10.1029/2002JC001313.

Thiébaux, J., E. Rogers, W. Wang, and B. Katz, 2003: A New High-Resolution Blended Real-Time Global (RTG) SST Analysis. *BAMS*, 84, 645–656.

Uddstrom M.J., W.R. Gray, R. Murphy. N.A. Olen & T. Murray, 1999: A Bayesian cloud mask for SST retrieval. *JTech*, 16, 117-132

Vazquez-Cuervo, J., E.M. Armstrong & A. Harris, 2004: The effect of aerosols and clouds on the retrieval of infrared SST, *J.Clim.*, 17 (20), 3921–3933.

Walton, CC., 1988: Nonlinear multichannel algorithms for estimating SST with AVHRR satellite data. *JAM*, 27, 115-124.

Walton, CC., 1985: Satellite measurement of SST in presence of volcanic aerosols. *J.Clim Appl. Meteor.*, 24, 501-507.

Walton, C.C., W.G. Pichel, J.F. Sapper & D. A. May, 1998: The development and operational application of nonlinear algorithms for the measurement of sea SSTs with the NOAA polar-orbiting environmental satellites. *JGR*, 103, 27,999–28,012.

Watts, P.D., M.R. Allen & T.J. Nightingale, 1996: Wind speed effects on sea surface emission and reflection for the Along Track Scanning Radiometer. *JTech*, 13, 126-141.

Wick, G., J. Bates & D. Scott, 2002: Satellite and skin-layer effects on the accuracy of SST measurements from the GOES satellites. *JTech*, 19, 1834-1847.

Wu, X, P. Menzel & G. Wade, 1999: Estimation of SST Using GOES-8/9 Radiance measurements. *BAMS*, 80, 1127-1138.

Wu, X. & W.L. Smith, 1997: Emissivity of rough sea surface for 8-13 μm: modeling and verification. *Appl.Opt.*, 36, 2609–2619.

Xu, F., & A. Ignatov, 2009: Evaluation of *in situ* SSTs for use in the calibration and validation of satellite retrievals. *JGR*, submitted.

Xu, F., A. Ignatov, and X. Liang, 2009: Towards continuous error characterization of SST in ACSPO, *2009 AMS Conference on GOES-R and NPOEES*, Phoenix AZ, 12-17 January 2009, http://ams.confex.com/ams/pdfpapers/143882.pdf.

Xue, Y., Cai, Guoyin, Guan, Y N, Cracknell, A P, J. Tang, 2005: Iterative self-consistent approach for Earth surface temperature determination. *IJRS*, 26(1), 185-192.

Yu, Y. and I.J. Barton, 1994: A non-regression-coefficients method of SST retrieval from space. *IJRS*, 15, 1189-1206.

Závody, A.M., C.T. Mutlow & D.T. Llewellyn-Jones, 1995: A radiative transfer model for SST retrieval for the along-track scanning radiometer. *JGR*, 100, 937–952.

Zhang C., F. Qiu, 2008: Empirical relationship between SST and water vapor: Improvement of the physical model with remote sensing derived data. *J. Oceanogr*., 64, 163 – 170.

# ACKNOWLEDGMENTS

This ATBD was prepared for the SST Application Team under the GOES-R Algorithm Working Group. Members of the GOES-R AT include: Drs Peter Minnett (U. Miami), William Smith, Sr (U. Hampton and U. of Wisconsin), John Sapper (NESDIS/OSDPD), and William Pichel (NESDIS/STAR). Contributions to this ATBD have been also provided by the GOES-R SST Development Team including Drs. XingMing Liang (STAR/CIRA), Boris Petrenko (STAR/IMSG), Nikolay Shabanov (STAR/IMSG), Prasanjit Dash (STAR/CIRA), Yury Kihai (STAR and DPS, and Feng Xu (STAR/CIRA). Help provided by the GOES-R Algorithm Integration Team (Walter Wolf, the Lead) is acknowledged.

# APPENDIX 1: COMMON ANCILLARY DATA SETS

## 1. LAND_MASK_NASA_1KM

### *a. Data description*

**Description**: Global 1km land/water used for MODIS collection 5
**Filename**: lw_geo_2001001_v03m.nc
**Origin**: Created by SSEC/CIMSS based on NASA MODIS collection 5
**Size**: 890 MB.
**Static/Dynamic**: Static

### *b. Interpolation description*

The closest point is used for each satellite pixel:

1) Given ancillary grid of large size than satellite grid
2) In Latitude / Longitude space, use the ancillary data closest to the satellite pixel.

## 2. SNOW_MASK_IMS_SSMI

### a. *Data description*

**Description**: Snow/Ice mask, IMS – Northern Hemisphere, SSM/I – Southern Hemisphere
4km resolution – the 25 km SSM/I has been oversampled to 4km
**Filename**: snow_map_4km_YYMMDD.nc
**Origin**: CIMSS/SSEC
**Size**: 39 MB.
**Static/Dynamic**: Dynamic

### b. *Interpolation description*

The closest point is used for each satellite pixel:

1) Given ancillary grid of large size than satellite grid
2) In Latitude / Longitude space, use the ancillary data closest to the satellite pixel.

## 3. OISST_WEEKLY_1DEGREE

### a. *Data description*

**Description:** NCEP EMC Reynolds OISST weekly analysis, 1 degree resolution.
**Filename**: oisst.YYYYMMDD.nc
Where,
YYYYMMDD – 4 digit year plus 2 digit month plus 2 digit day
**Origin**: NCEP/EMC
**Size**: 0.761 MB
**Static/Dynamic**: Dynamic

### b. *Interpolation description*

A double linear interpolation is applied using four nearest neighbor OISST grid points and the weight of the four points are defined by the Latitude / Longitude difference between the satellite observation point and the four nearest neighbor OISST grid points. The interpolation is realized in routine BLINT, which is called by routine GET_PIXEL_SST_ANALYSIS. There is no curvature effect.

Input OISST data is in a regular grid.

Suppose:

Latitude and Longitude of the four points are:
(Lat1, Lon1), (Lat1, Lon2), (Lat2, Lon1), (Lat2, Lon2)
Satllite observation point is
(Lat, Lon)

Define
aLat = (Lat – Lat1) / (Lat2 – Lat1)
alon = (Lon – Lon1) / (Lon2 – Lon1)

Then the weights at four points are:
w11 = aLat * aLon
w12 = aLat * (1 – aLon)
w21 = (1 – aLat) * aLon
w22 = (1-aLat) * (1 – aLon)

Also define any variable at the four points have values:
a11, a12, a21, a22

Then the corresponding interpolated value at satellite observation point (Lat, Lon) should be:

a(Lat, Lon) = ( a11*w11 + a12*w12 + a21*w21 + a22*w22 ) / u

Where,

u = w11 + w12 + w21 + w22

## *4. CRTM*

### a. Data *description*

**Description:** Community radiative transfer model
**Filename**: N/A
**Origin**: NOAA / NESDIS
**Size**: N/A
**Static/Dynamic**: N/A

### *b.* Interpolation *description*

A double linear interpolation is applied in the interpolation of the transmissitance and radiance profile, as well as in the surface emissivity, from four nearest neighbor NWP grid points to the satellite observation point. There is no curvature effect. The weights of the four points are defined by the Latitude / Longitude difference between neighbor NWP grid points and the satellite observation point. The weight is defined with subroutine ValueToGrid_Coord:

NWP forecast data is in a regular grid.

Suppose:
Latitude and Longitude of the four points are:
(Lat1, Lon1), (Lat1, Lon2), (Lat2, Lon1), (Lat2, Lon2)
Satellite observation point is:
(Lat, Lon)

Define
aLat = (Lat – Lat1) / (Lat2 – Lat1)
alon = (Lon – Lon1) / (Lon2 – Lon1)

Then the weights at four points are:
w11 = aLat * aLon

w12 = aLat * (1 – aLon)
w21 = (1 – aLat) * aLon
w22 = (1-aLat) * (1 – aLon)

Also define variable at the four points are:
a11, a12, a21, a22

Then the corresponding interpolated result at satellite observation point (Lat, Lon) should be:

a(Lat, Lon) = ( a11*w11 + a12*w12 + a21*w21 + a22*w22 ) / u

Where,

u = w11 + w12 + w21 + w22

**c. CRTM calling procedure in the AIT framework**

The NWP GFS pressure, temperature, moisture and ozone profiles start on 101 pressure levels.
They are converted to 100 layers in subroutine Compute_Layer_Properties. The layer temperature between two levels is simply the average of the temperature on the two levels.
layer_temperature(i) = (level_temperature(i) + level_temperature(i+1))/2
While pressure, moisture and ozone are assume to be exponential with height.
hp = (log(p1)-log(p2))/(z1-z2)
p = p1* exp(z*hp)
Where p is layer pressure, moisture or ozone. p1,p2 represent level pressure, moisture or ozone. z is the height of the layer.

CRTM needs to be initialized before calling. This is done in subroutine Initialize_OPTRAN. In this call, you tell CRTM which satellite you will run the model. The sensor name is passed through function call CRTM_Init. The sensor name is used to construct the sensor specific SpcCoeff and TauCoeff filenames containing the necessary coefficient data, i.e. seviri_m08.SpcCoeff.bin and seviri_m08.TauCoeff.bin. The sensor names have to match the coefficient file names. You will allocate the output array, which is RTSolution, for the number of channels of the satellite and the number of profiles. You also allocate memory for the CRTM Options, Atmosphere and RTSoluiton structure. Here we allocate the second RTSolution array for the second CRTM call to calculate derivatives for SST algorithm.

Before you call CRTM forward model, load the 100-layer pressure, temperature, Moisture and ozone profiles and the 101 level pressure profile into the Atmosphere Structure. Set the units for the two absorbers (H2O and O3) to be

MASS_MIXING_RATIO_UNITS and VOLUME_MIXING_RATIO_UNITS respectively. Set the Water_Coverage in Surface structure to be 100% in order to get surface emissivity over water. Land surface emissivity will be using SEEBOR. Also set other variables in Surface data structure, such as wind speed/direction and surface temperature. Use NWP surface temperature for land and coastline, and OISST sea surface temperature for water. Set Sensor_Zenith_Angle and Source_Zenith_Angle in Geometry structure. Call CRTM_Forward with normal NWP profiles to fill RTSolution, then call CRTM_Forward again with moisture profile multiplied by 1.05 to fill RTSolution_SST. The subroutine for this step is Call_OPTRAN.

After calling CRTM forward model, loop through each channel to calculate transmittance from each level to Top of Atmosphere (TOA). What you get from RTSolution is layer optical depth, to get transmittance

```
Trans_Atm_Clr(1) = 1.0

Do Level =  2 , TotalLevels
  Layer_OD = RTSolution(ChnCounter, 1)%Layer_Optical_Depth(Level -1)
  Layer_OD = Layer_OD / COS(CRTM%Grid%RTM(LonIndex,LatIndex) &
               %d(Virtual_ZenAngle_Index)%SatZenAng * DTOR)
  Trans_Atm_Clr(Level) = EXP(-1 * Layer_OD) &
              * Trans_Atm_Clr(Level - 1)
ENDDO
```

DTOR is degree to radius PI/180.

Radiance and cloud profiles are calculated in Clear_Radiance_Prof

```
SUBROUTINE Clear_Radiance_Prof(ChnIndex, TempProf, TauProf, RadProf,
&
                        CloudProf)
B1 = Planck_Rad_Fast(ChnIndex, TempProf(1))
RadProf(1) = 0.0_SINGLE
CloudProf(1) = B1*TauProf(1)

DO LevelIndex=2, NumLevels
  B2 = Planck_Rad_Fast(ChnIndex, TempProf(LevelIndex))
  dtrn = -(TauProf(LevelIndex) - TauProf(LevelIndex-1))
  RadProf(LevelIndex) = RadProf(LevelIndex-1) + (B1+B2)/2.0_SINGLE * dtrn


  CloudProf(LevelIndex) = RadProf(LevelIndex) + B2*TauProf(LevelIndex)
  B1 = B2
END DO
```

Transmittance, radiance and cloud profiles are calculated for both normal CRTM structure and the 2nd CRTM structure for SST.

Call Clear_Radiance_TOA to get TOA clear-sky radiance and brightness temperature.

```
SUBROUTINE Clear_Radiance_TOA(Option, ChnIndex, RadAtm, TauAtm, SfcTemp, &
                              SfcEmiss, RadClr, BrTemp_Clr, Rad_Down)
IF(Option == 1) THEN
  IF(PRESENT(Rad_Down))THEN
    RadClr = RadAtm + (SfcEmiss * Planck_Rad_Fast(ChnIndex, SfcTemp) &
         + (1. - SfcEmiss) * Rad_Down) * TauAtm
  ELSE
    RadClr = RadAtm + SfcEmiss * Planck_Rad_Fast(ChnIndex, SfcTemp) &
             * TauAtm
  ENDIF

  CALL Planck_Temp(ChnIndex, RadClr, BrTemp_Clr)

 ELSE
   RadClr = 0.0
   BrTemp_Clr = 0.0
ENDIF
```

In this subroutine, Rad_Down is optional, depending on if you want to have a reflection part from downward radiance when you calculate the clear-sky radiance. Notice that clear-sky radiance and brightness temperature on NWP grid only calculated for normal CRTM structure not the SST CRTM structure.

Also save the downward radiances from RTSolution and RTSolution_SST to CRTM_RadDown and CRTM_RadDown_SST. Save CRTM calculated surface emissivity to CRTM_SfcEmiss. The above steps are done in subroutine CRTM_OPTRAN